



気象庁

Japan Meteorological Agency

**CLIMATE CHANGE MONITORING REPORT  
2019**

**December 2020**

Published by the  
**Japan Meteorological Agency**

3-6-9 Toranomom, Minato City, Tokyo 105-8431, Japan

Telephone +81 3 3584 8603  
Facsimile +81 3 3434 9009  
E-mail [iao-jma@met.kishou.go.jp](mailto:iao-jma@met.kishou.go.jp)

**CLIMATE CHANGE MONITORING REPORT  
2019**

**December 2020**

**JAPAN METEOROLOGICAL AGENCY**



# Preface

The Japan Meteorological Agency (JMA) has published annual assessments under the title of *Climate Change Monitoring Report* since 1996 to highlight the outcomes of its activities (including monitoring and analysis of atmospheric, oceanic and global environmental conditions) and provide up-to-date information on climate change in Japan and around the world.

In 2019, extreme meteorological phenomena such as heavy rainfall and heat waves occurred worldwide. Japan experienced particularly significant rainfall from western parts to the Tokai region during the Heavy Rain Event of July 2018, when overall precipitation nationwide was the highest since 1982, and extremely high temperatures subsequently persisted across the country except in the Okinawa/Amami region. The monthly mean temperature for July and the seasonal mean temperature for summer in eastern Japan were the highest since 1946.

The increasing frequency and scale of such extreme weather events are considered to stem from global warming. JMA, in consultation with the Advisory Panel on Extreme Climatic Events, has concluded that Japan's unprecedentedly warm winter (December 2019 – February 2020) was due in part to an ongoing global warming-related rise in temperatures worldwide.

As global warming continues, the frequency and scale of extreme events are expected to increase. The Paris Agreement will be implemented in 2020, forming a new international framework with which to combat climate change and support adaptation to its effects. With Japan's introduction of the Climate Change Adaptation Act in December 2018, national and local governments are currently stepping up their efforts in this regard.

This report is intended to provide a scientific basis for better implementation of measures relating to climate change and to raise awareness of global environmental issues.



**Yasuo Sekita**  
**Director-General**  
**Japan Meteorological Agency**



# Index

<b>Topics</b> .....	<b>1</b>
<b>I 2019 as the warmest year on record for Japan</b> .....	<b>1</b>
I.1 Surface temperature over Japan .....	1
I.2 Characteristics of atmospheric circulation for high temperature conditions over Japan in 2019 .....	2
<b>II Smallest Antarctic ozone hole since 1990</b> .....	<b>5</b>
<b>III Deep-ocean circulation monitoring by JMA research vessels</b> .....	<b>7</b>
<b>Chapter 1 Climate in 2019</b> .....	<b>9</b>
<b>1.1 Global climate summary</b> .....	<b>9</b>
<b>1.2 Climate in Japan</b> .....	<b>13</b>
1.2.1 Annual characteristics .....	13
1.2.2 Seasonal characteristics .....	14
<b>1.3 Atmospheric circulation and oceanographic conditions</b> .....	<b>19</b>
1.3.1 Characteristics of individual seasons .....	19
1.3.2 Global average temperature in the troposphere .....	26
1.3.3 Asian summer monsoon .....	26
1.3.4 Tropical cyclones over the western North Pacific and the South China Sea .....	26
<b>Chapter 2 Climate Change</b> .....	<b>29</b>
<b>2.1 Changes in temperature</b> .....	<b>29</b>
2.1.1 Global surface temperature .....	29
2.1.2 Surface temperature over Japan .....	30
2.1.3 Long-term trends of extreme temperature events in Japan .....	31
2.1.4 Urban heat island effect at urban stations in Japan .....	33
<b>2.2 Changes in precipitation</b> .....	<b>35</b>
2.2.1 Global precipitation over land .....	35
2.2.2 Precipitation over Japan .....	35
2.2.3 Long-term trends of extreme precipitation events in Japan .....	36
2.2.4 Long-term trends of heavy rainfall analyzed using AMeDAS data .....	37
2.2.5 Snow depth in Japan .....	39
<b>2.3 Changes in the phenology of cherry blossoms and acer leaves in Japan</b> .....	<b>40</b>
<b>2.4 Tropical cyclones over the western North Pacific and the South China Sea</b> .....	<b>41</b>
<b>2.5 Sea surface temperature</b> .....	<b>42</b>
2.5.1 Global sea surface temperature .....	42

2.5.2	Sea surface temperature (around Japan)	43
<b>2.6</b>	<b>El Niño/La Niña and PDO (Pacific Decadal Oscillation)</b>	<b>44</b>
2.6.1	El Niño/La Niña	44
2.6.2	Pacific Decadal Oscillation	45
<b>2.7</b>	<b>Global ocean heat content</b>	<b>46</b>
<b>2.8</b>	<b>Sea levels around Japan</b>	<b>47</b>
<b>2.9</b>	<b>Sea ice</b>	<b>49</b>
2.9.1	Sea ice in Arctic and Antarctic areas	49
2.9.2	Sea ice in the Sea of Okhotsk	51
<b>2.10</b>	<b>Snow cover in the Northern Hemisphere</b>	<b>52</b>
<b>Chapter 3 Atmospheric and Marine Environment Monitoring</b>		<b>54</b>
<b>3.1</b>	<b>Monitoring of greenhouse gases</b>	<b>54</b>
3.1.1	Concentration of carbon dioxide	55
3.1.2	Concentration of methane	67
3.1.3	Concentration of nitrous oxide	69
<b>3.2</b>	<b>Monitoring of the ozone layer and ultraviolet radiation</b>	<b>70</b>
3.2.1	Ozone layer	70
3.2.2	Solar UV radiation in Japan	73
3.2.3	Concentration of ozone-depleting substances	73
<b>3.3</b>	<b>Monitoring of aerosols and surface radiation</b>	<b>76</b>
3.3.1	Aerosols	76
3.3.2	Kosa (Aeolian dust)	77
3.3.3	Solar radiation and downward infrared radiation	78

## Topics

### I 2019 as the warmest year on record for Japan

- The annual anomaly of the average temperature over Japan was  $+0.92^{\circ}\text{C}$ , the highest on record since 1898. On a longer time scale, it is virtually certain that the annual average temperature over Japan has risen and the warmest years on record have all been observed since the 1990s.
- These long-term trends and recent warm years can be largely attributed to global warming caused by increased concentrations of greenhouse gases such as  $\text{CO}_2$  and the influence of natural climate variabilities over different time scales ranging from years to decades.

#### I.1 Surface temperature over Japan

JMA has monitored long-term changes in the surface temperature over Japan based on 15 observation stations<sup>1</sup> that have continued observation for a long period of time and are thought to be with relatively small influence of urbanization. The annual anomaly of the average surface temperature over Japan (deviation from the 1981 – 2010 average) has risen at a rate of  $1.24^{\circ}\text{C}$  per century (statistically significant at a confidence level of 99%) together with fluctuates on different time scales ranging from years to decades. The annual anomaly of mean surface temperature in Japan for 2019 is estimated to have been  $0.92^{\circ}\text{C}$ , which is the highest since 1898 (Figure I.1-1 and Table I.1-1). Most of the months in 2019 were warmer than normal for each month (Table I.1-2).

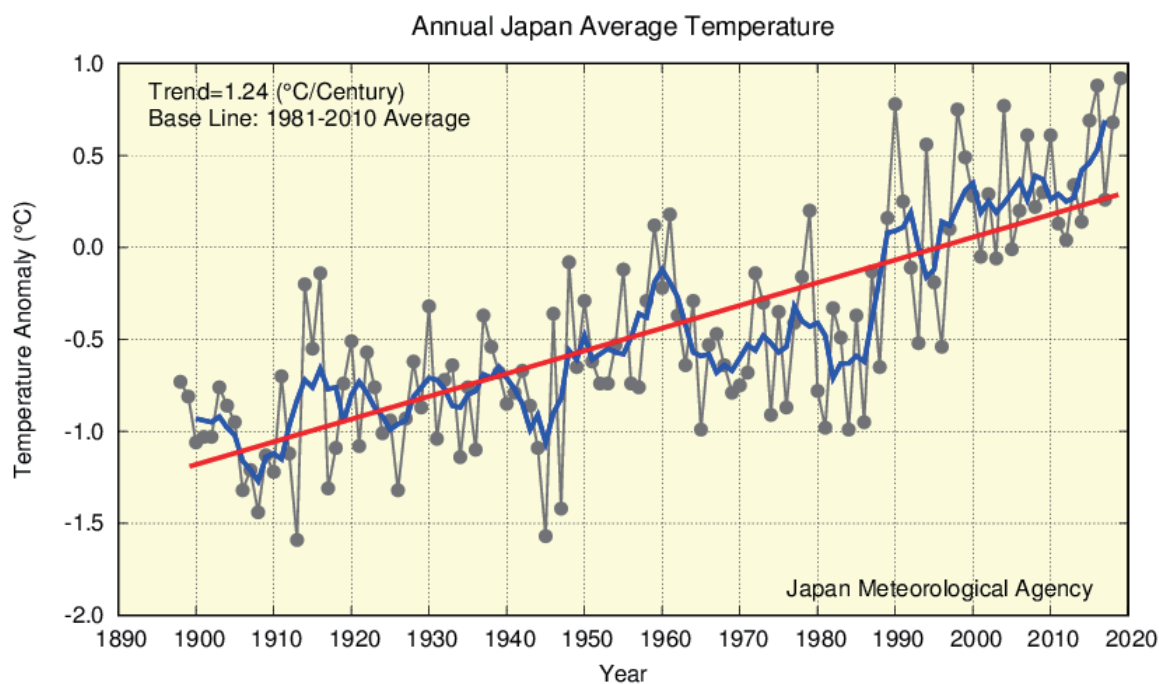


Figure I.1-1 Annual surface temperature anomalies from 1898 to 2019 in Japan. Anomalies are deviations from the baseline (i.e., the 1981 – 2010 average). The thin black line

<sup>1</sup> Please refer to Table 2.1-1 regarding observation stations whose data are used to calculate surface temperature anomalies over Japan

indicates the surface temperature anomaly for each year. The blue line indicates the five-year running mean, and the red line indicates the long-term linear trend.

Table I.1-1 The warmest 10 years over Japan

Rank	1	2	3	4	5	6	7	8	9	10
Year	2019	2016	1990	2004	1998	2015	2018	2010	2007	1994
Anomaly (°C)	+0.92	+0.88	+0.78	+0.77	+0.75	+0.69	+0.68	+0.61	+0.61	+0.56

Table I.1-2 Monthly surface temperature anomalies in 2019 and their ranks on record since 1898 for each month

	Jan.	Feb.	Mar.	Apr.	May	Jun.	Jul.	Aug.	Sep.	Oct.	Nov.	Dec.
Anomaly (°C)	+0.80	+1.49	+1.32	+0.05	+1.62	+0.42	+0.20	+0.73	+1.43	+1.61	+0.43	+0.99
Rank	15	6	3	32	4	21	43	12	6	2	20	9

### *1.2 Characteristics of atmospheric circulation for high temperature conditions over Japan in 2019*

The year's highest annual average temperature anomaly over Japan since 1898 is attributed to global warming caused by increased concentrations of greenhouse gases such as CO<sub>2</sub>, and to the influence of natural climate variabilities over time scales ranging from years to decades. These influences include convective activity in the tropics and westerly jet stream meandering associated with the El Niño event that emerged in autumn 2018 and persisted until spring 2019, and sea surface temperature (SST) conditions in the Indian Ocean.

#### (1) Winter (December 2018 – February)

Warm air covered large parts of Japan in association with anti-cyclonic circulation anomalies around the East China Sea (Figure I.2-1) due to meandering of the upper-level Subtropical Jetstream (STJ). The eastward extension of the Siberian High was weaker than normal, and the Aleutian Low was shifted northwestward of its normal position. As a result, typical winter pressure patterns around Japan did not persist, contributing to weaker-than-normal southward cold air outbreaks in southern and other parts of the country. In February, warm air flowed into Okinawa/Amami due to anti-cyclonic circulation anomalies seen from the Philippines to the south of Japan in the lower troposphere (Figure I.2-2 (a)) in association with suppressed tropical convective activity around the Maritime Continent, which was consistent with common patterns observed in past El Niño events.

#### (2) Spring (March – May)

High-pressure systems frequently covered Japan, bringing predominantly sunny conditions. In March, cold-air outbreaks were weaker than normal. In May, southwesterly warm-air inflows were brought by frequent passages of low-pressure systems around northeastern China.

#### (3) Summer (June – August)

From the end of July to the first half of August, eastern and other parts of Japan experienced hot sunny conditions in association with expansion of the upper-level

Tibetan High and the lower-level North Pacific Subtropical High. This may be attributable to meandering of the westerly jet stream over Japan and enhanced convective activity from the Philippines to the area east of the Philippines.

#### (4) Autumn (September – November)

Warm air covered large parts of Japan in association with anti-cyclonic circulation anomalies around the country (Figure I.2-3) due to meandering of the upper-level westerly jet stream. A stronger-than-normal high-pressure system east of Japan in the lower troposphere also brought warm air inflows to the country. The meandering of the upper-level westerly jet stream over Japan was associated with suppressed convective activity from the central part of the southern equatorial Indian Ocean to the Maritime Continent, which may be attributable to the contrast between above-normal SSTs in the western Indian Ocean and below-normal SSTs in the eastern Indian Ocean as a typical characteristic of a positive Indian Ocean Dipole. In September, Japan tended to be covered by high-pressure systems (Figure I.2-4 (a)) bringing predominantly sunny conditions in association with enhanced convective activity east of the Philippines (Figure I.2-4 (b)).

Global average surface temperatures typically rise after El Niño events, as seen prior to 2016 (the highest-ever global average surface temperature) and 2015 (the third highest). However, the average temperature over Japan is subject to other climate variabilities, meaning that El Niño events do not necessarily bring warmer conditions. For example, in 1990 and 2004 (Table I.1-1), the country experienced warmer conditions with no El Niño event. However, the higher temperatures observed in 1998, 2015 and 2016 are attributable to El Niño conditions. While the El Niño event that terminated in the spring of 2019 may have contributed to the warmer conditions observed in certain regions and periods, the higher temperatures seen from summer onward are attributed to other climate variabilities.

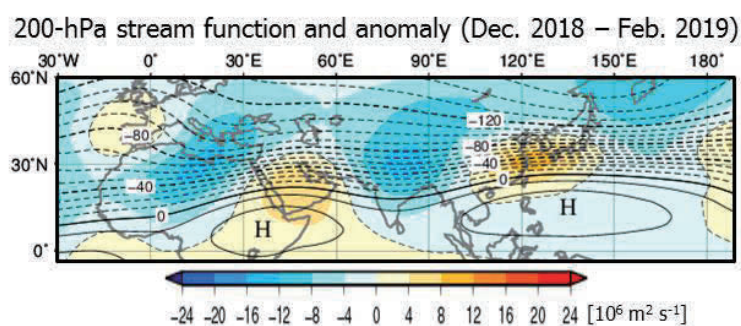


Figure I.2-1 200-hPa stream function (contours) and anomaly (shade) for December 2018 – February 2019

The contours are drawn at intervals of  $10 \times 10^6 \text{ m}^2 \text{ per s}$ . The base period for the normal is 1981 – 2010.

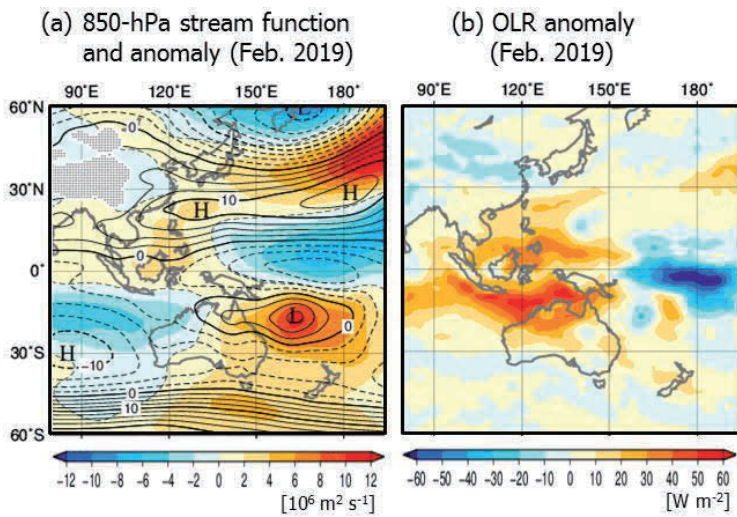


Figure I.2-2 (a) 850-hPa stream function (contours) and anomaly (shade), (b) outgoing longwave radiation (OLR) anomaly for February 2019

The contours are drawn at intervals of (a)  $10 \times 10^6 \text{ m}^2 \text{ s}^{-1}$ . The base period for the normal is 1981 – 2010.

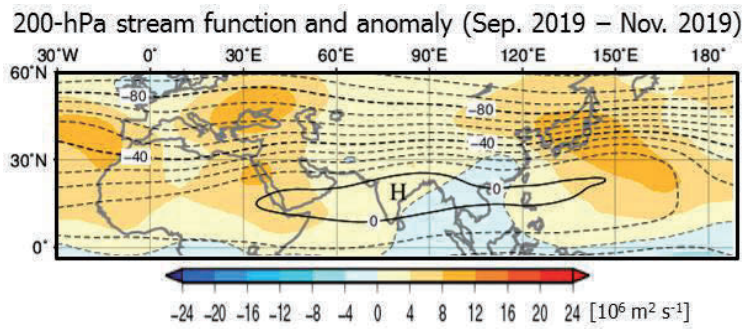


Figure I.2-3 As per Figure I.2-1, but for September – November 2019.

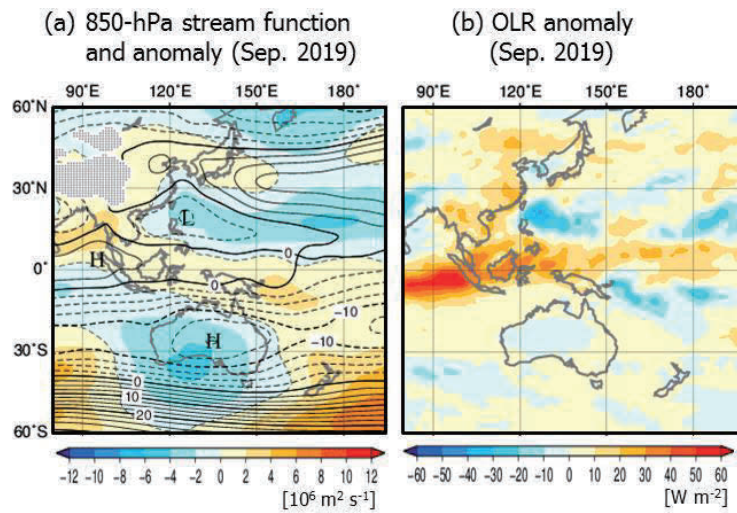


Figure I.2-4 As per Figure I.2-2, but for September 2019.

## II Smallest Antarctic ozone hole since 1990

- The annual maximum size of the ozone hole in 2019 was the smallest since 1990, when large-scale ozone hole continuously began to be observed.
- The expansion of the ozone hole was mainly attributed to particular meteorological conditions such as the occurrence of sudden stratospheric warming over the Antarctic at the end of August.

The formation and development of the ozone hole are closely related to the atmospheric concentration of ozone-depleting substances such as chlorofluorocarbons and meteorological conditions above Antarctica. Concentrations of ozone-depleting substances (ODSs) have shown a gradual decline worldwide since the mid-1990s due to the effects of production regulations based on the Montreal Protocol on Substances that Deplete the Ozone Layer (adopted in September 1987 and enforced in January 1989). However, concentrations are still higher than in the 1980s (Figure 3.2-7), suggesting that the Antarctic ozone hole in 2019 would have been as large as in the previous few years.

Figure II.1 shows a time-series representation of the daily ozone hole area for 2019. The ozone hole formed as usual in August and expanded until early September, then shrank rapidly from late October and disappeared on 10 November – the earliest since 1990. Its maximum size of 11.0 million square kilometers (about 0.8 times the size of Antarctica) was observed on 7 September, approximately matching scales observed in the mid-1980s. This was the smallest since 1990, when large-scale ozone hole continuously began to be observed (Figure 3.2-3). Its maximum size was similar to that of 1982, but the latter peaked in the second half of September while the 2019 ozone hole expanded rapidly from August (as seen with other ozone holes in recent years) before unexpectedly peaking in early September.

The significant reduction in the scale of the 2019 ozone hole can mainly be attributed to peculiar meteorological conditions. The stratospheric temperature at about 20 km in the polar vortex was much higher than the most recent decadal average from the end of August onward (Figure II.2). This hindered the formation of polar stratospheric clouds (PSCs), which play an important role in ozone destruction. The weaker polar vortex also induced flows of high-concentration ozone from low latitudes.

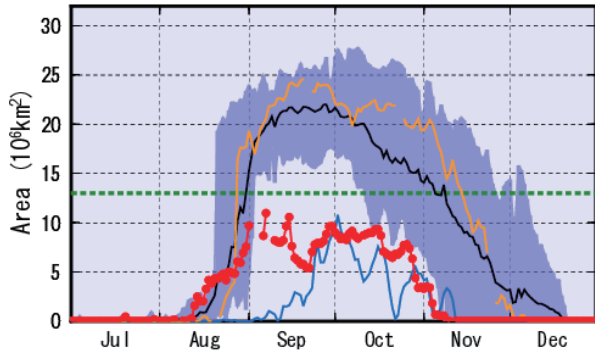


**Figure II.1 Time-series representation of the daily ozone hole area for 2019**

Red: 2019; orange: 2018; blue: 1982; black: 2009 – 2018 average

Blue shading: Range of daily minima and maxima for the previous decade

Green dotted line: Antarctic area (13.9 million square kilometers)

Based on data from NASA’s Ozone Monitoring Instrument (OMI) satellite sensors

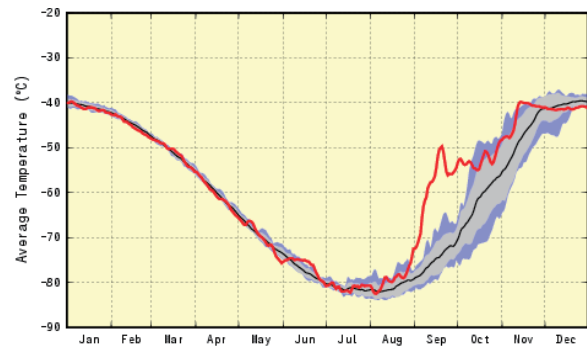


**Figure II.2 Time-series representation of daily temperatures averaged over 60°S latitude (50 hPa)**

Red: 2019; black: 2009 – 2018 average

Grey shading: Standard deviation range for the previous decade

Blue shading: Range of daily minima and maxima for the previous decade

Based on the Japanese 55-year Reanalysis (JRA-55)

*Scientific Assessment of Ozone Depletion: 2018 (WMO, 2018a)* reported that the ozone hole has shown a statistically significant decrease in scale and is expected to gradually shrink, with springtime total column ozone in the 2060s returning to 1980 values. As ODS concentrations in the atmosphere are decreasing but remain high, ongoing monitoring of stratospheric ozone is required.

### III. Deep-ocean circulation monitoring by JMA research vessels

- The Japan Meteorological Agency (JMA) observed chlorofluorocarbons (CFCs) in the lower layer of the western North Pacific from its research vessels in summer 2018 and winter 2019. The results indicated that water in this layer, which was originally at the surface of the Antarctic Ocean and absorbed CFCs from the atmosphere, flows from the South Pacific to the North Pacific on the western boundary current of general circulation in the Pacific.

JMA's ship-based western North Pacific hydrographic observation supports climate monitoring, with precise evaluation of chemical and physical parameters to clarify air-sea interaction/oceanic CO<sub>2</sub> accumulation and abyssal circulation flow paths.

CFCs are artificial chemicals that were not originally present in oceans. Since CFCs released into the atmosphere as a result of human activity now dissolve into surface water and are subducted into deeper layers, tracking of seawater containing these chemicals helps to determine its flow speed and path. Based on monitoring of temperature, salinity and dissolved oxygen and currents, surface water is considered to subduct into the bottom layer of the Antarctic Ocean and flow northward to the western Pacific on the western-boundary current in general Pacific circulation. CFCs were first identified in the southwestern South Pacific in 1996 by NOAA (USA) and in the northwestern South Pacific in 2007 by JAMSTEC (Japan), indicating that subducted lower-layer water flows northward in the western South Pacific. CFCs were first identified in the bottom layer of the southwestern North Pacific by JMA in August – September 2018 then in January – February 2019 (Figure III-1), indicating that lower-layer water flows from the South Pacific to the North Pacific on the western boundary current of general circulation in the Pacific.

In consideration of locational and temporal differences among these observations, lower-layer water is considered to flow northward at about 1 cm/sec (approx. 315 km/year). Figure III-2 shows the distribution of CFC concentrations simulated using the Meteorological Research Institute's ocean circulation model. The results indicate that CFCs stayed in the South Pacific in 1996, crossed the equator around 2007 and reached the southwestern North Pacific in 2017. These results are consistent with those of actual CFC observation.

JMA remains committed to its ship-based hydrographic observation and its contribution to climate model validation, and to improving global warming prediction via the online provision of observation data.

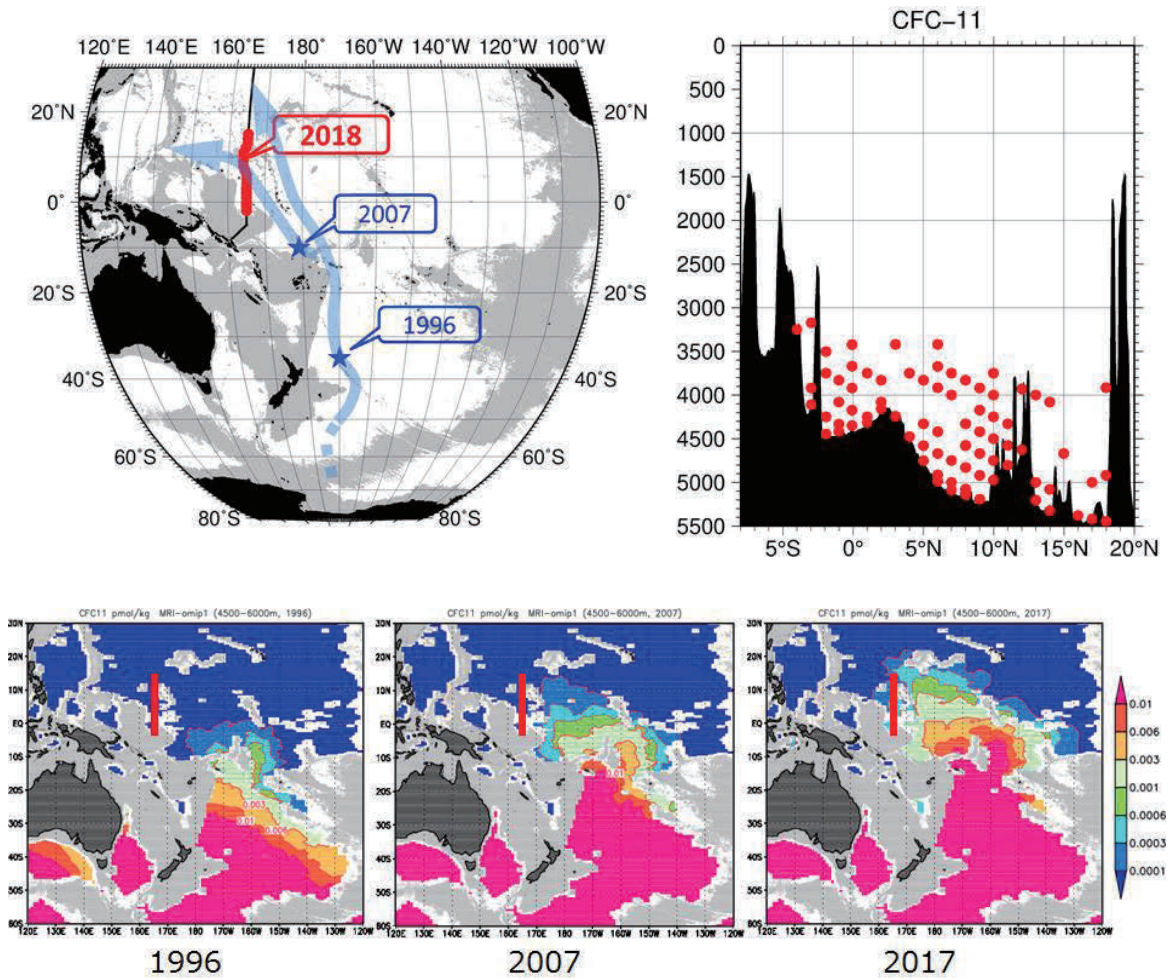


**Figure III-1 Pacific CFC observation (upper left)**

Bold red line: JMA observation; blue stars: previous observations; light-blue arrows: sea-floor flow paths estimated from various observations; shading: water depths of 4,000 m or less

**Vertical cross section along 165°E (upper right)**

Red circles: locations of CFC-11 observation near the sea floor

**Figure III-2 Ocean circulation model distribution of CFC-11 concentration (pmol/kg) averaged over depths of 4,500 – 6,000 m (bottom)**

Bold red line: JMA observation of CFC-11

## Chapter 1 Climate in 2019

### 1.1 Global climate summary

- Extremely high temperatures were observed in various parts of the world. Heat waves occurred from northern to central Europe in June and July, with new national high-temperature records being set in several countries.
- Numerous fatalities and considerable economic damage were caused by heavy rain in and around South Asia (July – October) and from the northern to western part of Eastern Africa (October – December), cyclones in the southern part of Eastern Africa (March and April), and hurricane conditions in the Bahamas (September). Large bushfires caused severe damage in Australia (September – December).

Major extreme climate events<sup>1</sup> and weather-related disasters that occurred in 2019 are shown in Figure 1.1-1 and Table 1.1-1.

Extremely high temperatures were observed in various parts of the world ((2), (3), (5), (9), (11), (12), (16), (18), (20), (24), (25), (27) in Figure 1.1-1). In and around Europe, extremely high temperatures were observed from June to December ((12) in Figure 1.1-1), and annual mean temperatures in Germany and France were the second and third highest since 1881 and 1900, respectively (Deutscher Wetterdienst and Meteo France). Heat waves occurred in June and July from northern to central Europe ((14) in Figure 1.1-1), and it was estimated that two heatwaves in France from 24 June to 7 July and from 21 to 27 July caused a total of more than 1,400 excess deaths (source: French Government). New national-high temperature records were set in France, Germany, the Netherlands, Belgium, Luxembourg and the United Kingdom. In Alaska, extremely high temperatures were observed from February to March, from June to July and in September ((20) in Figure 1.1-1), and the annual mean temperature in Alaska was the highest on record since 1925 (National Oceanic and Atmospheric Administration, the USA). In Australia, extremely high temperatures were observed in January, March, July and from September to December ((27) in Figure 1.1-1), and the annual mean temperature was the highest on record since 1910 (source: Bureau of Meteorology, Australia).

In midwestern and southeastern parts of the USA, extremely high precipitation was observed in February, from April to May, and from September to October ((22) in Figure 1.1-1). In the contiguous USA, seasonal precipitation from December 2018 to February 2019 was the highest on record since 1896, and annual precipitation for 2019 was the second highest on record since 1895 (National Oceanic and Atmospheric Administration, USA). Conversely, from the central Malay Peninsula to Java Island, extremely low precipitation amounts were observed from June to July and from September to November ((6) in Figure 1.1-1). In Australia, annual precipitation for 2019 was the lowest since 1900 (Bureau of Meteorology, Australia).

Heavy rain from July to October caused more than 2,300 fatalities in and around South Asia (sources: governments of India/Pakistan and the European Commission) ((8) in Figure 1.1-1). Cyclone Idai in March and Cyclone Kenneth in April caused more than 1,000 fatalities in the southern part of Eastern Africa (European Commission) ((19) in Figure 1.1-1). Hurricane Dorian caused more than 70 fatalities from the eastern USA to the Bahamas (sources: governments of

<sup>1</sup> Extreme climate events are defined by anomalies or ratios to climatological normals. Normals represent mean climate conditions at given sites, and are currently based on a 30-year mean covering the period from 1981-2010.

the USA and the Bahamas), and economic losses in the Bahamas were estimated at more than 34 billion US dollars (Inter-American Development Bank) ((23) in Figure 1.1-1). In Australia, large bushfires destroyed more than six million hectares (approximately 16% of Japan's land area) from September to December (International Federation of Red Cross and Red Crescent Societies; not shown in Figure 1.1-1 due to a lack of official information on economic damage).

Annual mean temperatures were above normal in most parts of the world, and were very high in Siberia, from northeastern to southern parts of East Asia, Southeast Asia, the southern part of South Asia, Central Asia, the Middle East, from central to southern Europe, from the eastern part of Eastern Africa to Southern Africa, Alaska, from the southern part of North America to Central America, from the northern to eastern part of South America, and Australia. Annual mean temperatures were below normal in central North America (Figure 1.1-2).

Annual precipitation was above normal in South Asia, from the northern Middle East to the northern part of Northern Africa, Alaska, the USA, and the northwestern part of South America, and were below normal in the southeastern part of Southeast Asia, the western part of Northern Africa, the southwestern part of South America, and from eastern to central Australia (Figure 1.1-3).

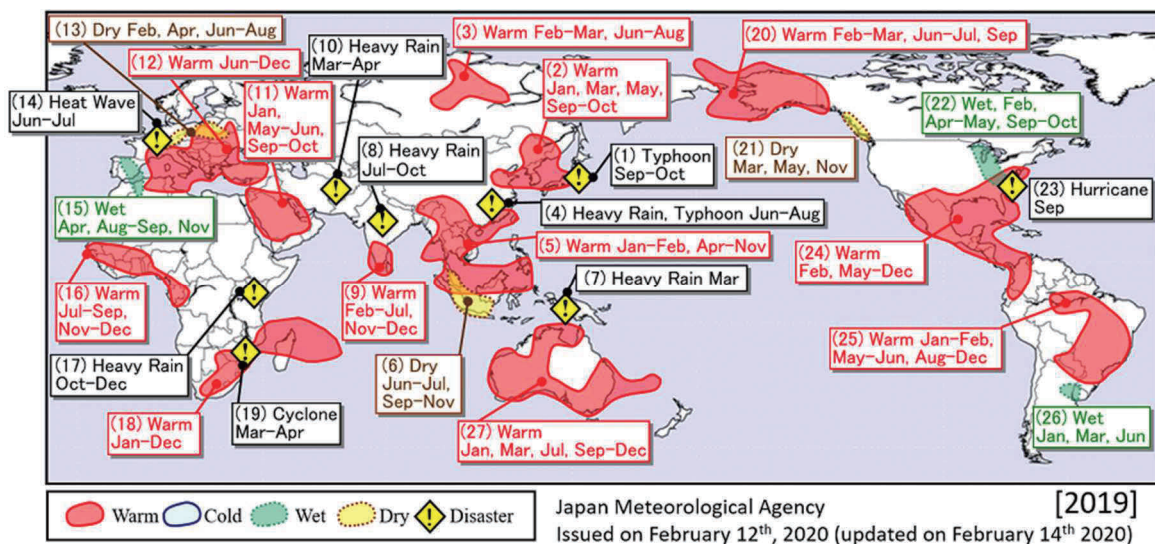


Figure 1.1-1 Major extreme events and weather-related disasters observed in 2019<sup>2</sup>

Schematic representation of major extreme climatic events and weather-related disasters occurring during the year.

“Warm”, “Cold”, “Wet” and “Dry” indicate that monthly extreme events occurred three times or more during the year in these regions. JMA defines an extreme climate event as a phenomenon likely to happen only once every 30 years.

Data and information on disasters are based on official reports of the United Nations and national governments and databases of research institutes (EM-DAT).

EM-DAT: The Emergency Events Database - Université Catholique de Louvain (UCL) - CRED, D. Guha-Sapir - www.emdat.be, Brussels, Belgium.

<sup>2</sup> Annual distribution maps for major extreme climatic events and weather-related disasters after 2008 are provided at JMA’s website.

<https://ds.data.jma.go.jp/tcc/tcc/products/climate/annual/index.html>

Table 1.1-1 Major extreme events and weather-related disasters occurring in 2019

No.	Event
(1)	Typhoon: from the Pacific side of northern Japan to the Pacific side of eastern Japan (September – October)
(2)	Warm: in and around the northeastern part of East Asia (January, March, May, September – October)
(3)	Warm: from the northern to central part of Central Siberia (February – March, June – August)
(4)	Heavy Rain and Typhoon: from eastern China to northern Thailand (June – August)
(5)	Warm: from the southern part of East Asia to the central part of Southeast Asia (January – February, April – November)
(6)	Dry: from the central part of the Malay Peninsula to Java Island (June – July, September – November)
(7)	Heavy Rain: eastern Indonesia (March)
(8)	Heavy Rain: in and around South Asia (July – October)
(9)	Warm: from southern India to Sri Lanka (February – July, November – December)
(10)	Heavy Rain: from the northern Middle East to India (March – April)
(11)	Warm: the Arabian Peninsula (January, May – June, September – October)
(12)	Warm: in and around southern Europe (June – December)
(13)	Dry: from eastern to central Europe (February, April, June – August)
(14)	Heat Wave: from northern to central Europe (June – July)
(15)	Wet: in and around Spain (April, August – September, November)
(16)	Warm: from the western part of Western Africa to the western part of Middle Africa (July – September, November – December)
(17)	Heavy Rain: from the northern to western part of Eastern Africa (October – December)
(18)	Warm: from Mauritius to South Africa (January – December)
(19)	Cyclone: the southern part of Eastern Africa (March – April)
(20)	Warm: in and around Alaska (February – March, June – July, September)
(21)	Dry: southwestern Canada (March, May, November)
(22)	Wet: from the Midwestern to southeastern USA (February, April – May, September – October)
(23)	Hurricane: from the eastern USA to the Bahamas (September)
(24)	Warm: from the eastern USA to the northwestern part of South America (February, May – December)
(25)	Warm: in and around Brazil (January – February, May – June, August – December)
(26)	Wet: in and around northeastern Argentina (January, March, June)
(27)	Warm: Australia (January, March, July, September – December)

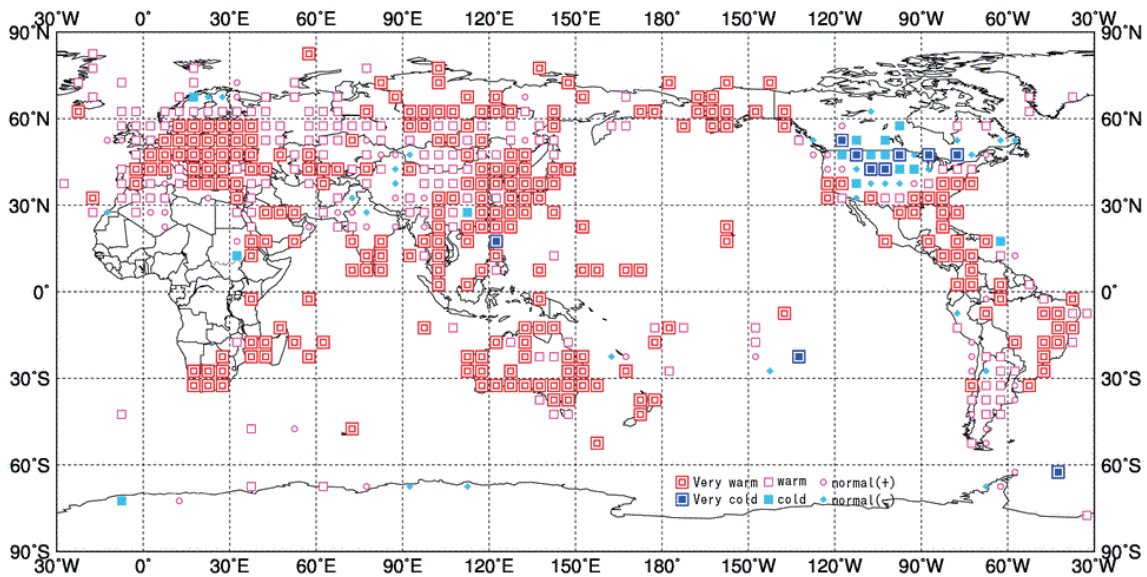


Figure 1.1-2 Annual mean temperature anomalies in 2019<sup>3</sup>

Categories are defined by the annual mean temperature anomaly against the normal divided by its standard deviation and averaged in  $5^\circ \times 5^\circ$  grid boxes. Red/blue marks indicate values above/below the normal calculated for the period from 1981 to 2010. The thresholds of each category are  $-1.28$ ,  $-0.44$ ,  $0$ ,  $+0.44$  and  $+1.28$ <sup>4</sup>. Areas over land without graphical marks are those where observation data are insufficient or normal data are unavailable.

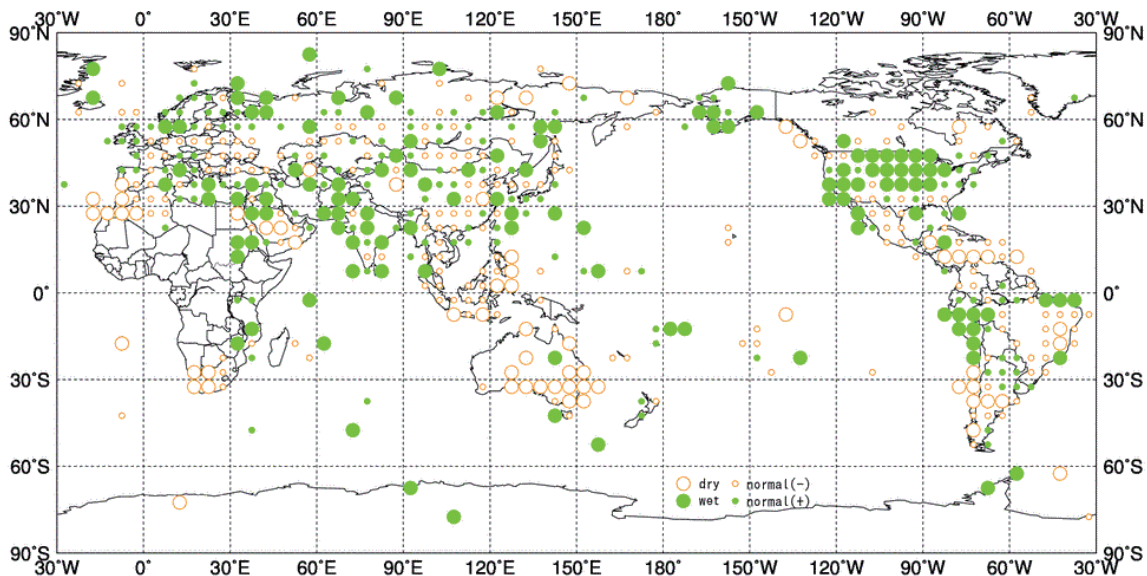


Figure 1.1-3 Annual total precipitation amount ratios in 2019

Categories are defined by the annual precipitation ratio to the normal averaged in  $5^\circ \times 5^\circ$  grid boxes. Green/yellow marks indicate values above/below the thresholds. The thresholds of each category are 70, 100 and 120% of the normal calculated for the period from 1981 to 2010. Areas over land without graphical marks are those where observation data are insufficient or normal data are unavailable.

<sup>3</sup> Distribution maps for normalized annual mean temperature anomaly and precipitation amount ratio to normal after 2008 are provided at JMA's website.

<https://ds.data.jma.go.jp/tcc/tcc/products/climate/annual/index.html>

<sup>4</sup> In normal distribution, values of 1.28 and 0.44 correspond to occurrence probabilities of less than 10 and 33.3%, respectively.

## 1.2 Climate in Japan<sup>5</sup>

- Annual mean temperatures were significantly above normal nationwide as a result of ongoing above-normal values throughout the period.
- Record rainfall and record storm conditions were observed in northern and eastern Japan due to the approach and passage of typhoons Faxai and Hagibis.
- From summer to autumn, record rainfall was observed in several regions.

### 1.2.1 Annual characteristics

The annual climate anomaly/ratio for Japan in 2019 is shown in Figure 1.2-1.

- Annual mean temperatures were significantly above normal nationwide.
- Annual precipitation was significantly below normal on the Sea of Japan side of northern Japan, below normal on the Sea of Japan side of eastern Japan, significantly above normal in Okinawa/Amami, above normal on the Pacific side of eastern and western Japan, and near normal on the Pacific side of northern Japan and the Sea of Japan side of western Japan.
- Annual sunshine durations were significantly above normal in northern Japan and on the Sea of Japan side of eastern Japan, above normal on the Sea of Japan side of western Japan, below normal in Okinawa/Amami, and near normal on the Pacific side of eastern and western Japan.

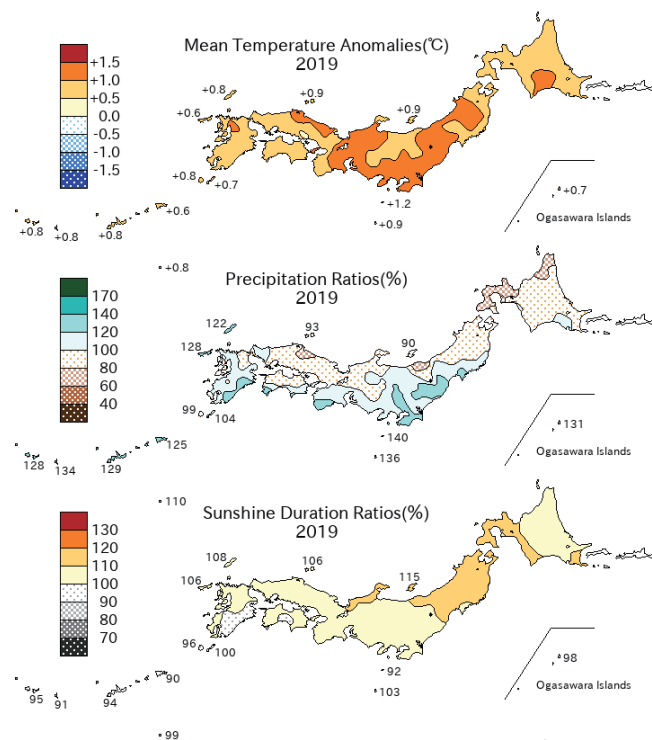


Figure 1.2-1 Annual climate anomaly/ratio for Japan in 2019

The base period for the normal is 1981 – 2010.

<sup>5</sup> The term *significantly above normal* is used for cases in which observed mean temperatures or precipitation amounts exceed the 90th percentile for the base period (1981 – 2010), and *significantly below normal* is used when the corresponding figures fall below the 10th percentile.

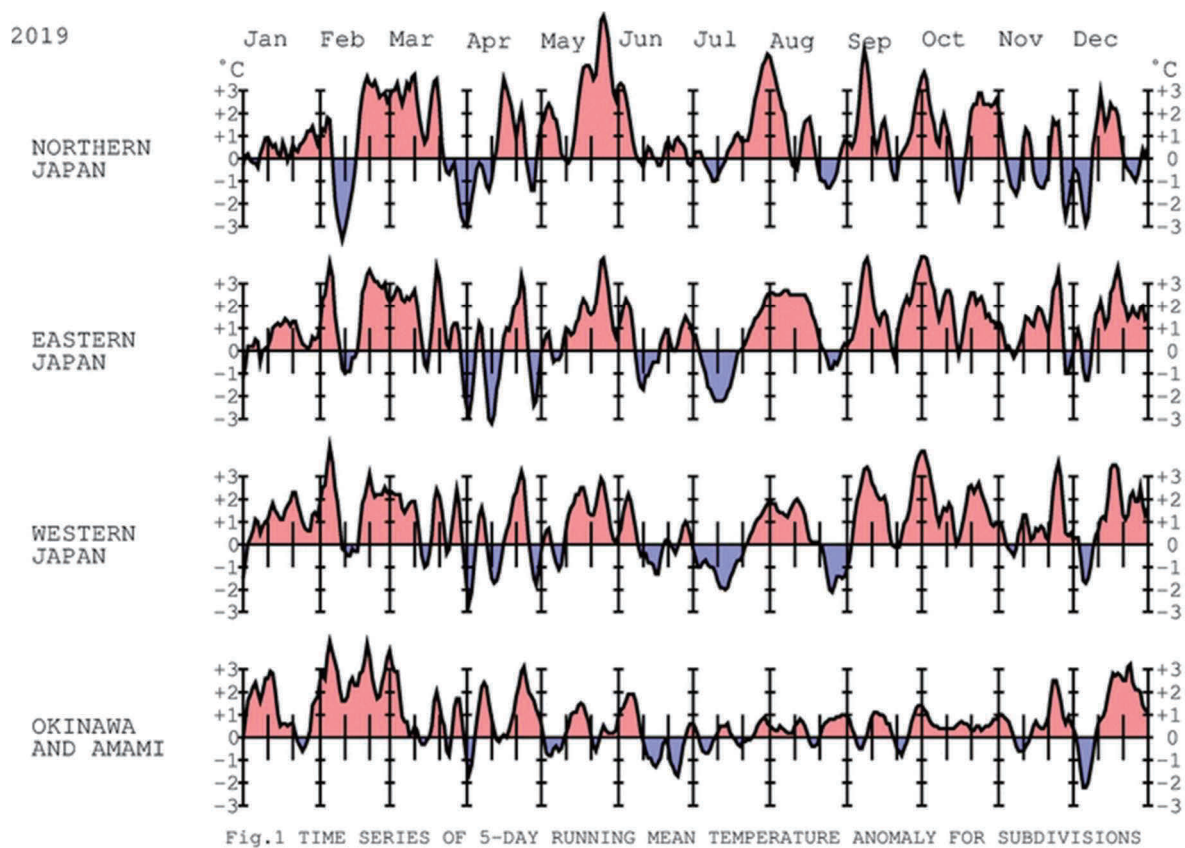


Fig.1 TIME SERIES OF 5-DAY RUNNING MEAN TEMPERATURE ANOMALY FOR SUBDIVISIONS

Last Data:2020/ 1/ 2

Figure 1.2-2 Five-day running mean temperature anomaly for divisions (January – December 2019)

The base period for the normal is 1981 – 2010.

### 1.2.2 Seasonal characteristics

Five-day running mean temperature anomalies for different divisions (January – December 2019) are shown in Figure 1.2-2, and seasonal anomalies/ratios for Japan in 2019 are shown in Figure 1.2-3. Numbers of observatories reporting record monthly and annual mean temperatures, precipitation amounts and sunshine durations (2019) are shown in Table 1.2-1.

#### (1) Winter (December 2018 – February 2019)

- Mean temperatures were above normal nationwide except in northern Japan, where values were near normal.
- Precipitation was significantly below normal on the Pacific side of northern Japan and on the Sea of Japan side of eastern Japan, below normal on the Sea of Japan side of northern Japan and on the Pacific side of eastern Japan, above normal in Okinawa/Amami and near normal in western Japan.
- Sunshine durations were above normal on the Pacific side of northern Japan, significantly below normal on the Pacific side of western Japan, below normal on the Pacific side of eastern Japan and on the Sea of Japan side of western Japan, and near normal on the Sea of Japan side of northern and eastern Japan and in Okinawa/Amami.

In association with a weak winter monsoon, seasonal mean temperatures were significantly above normal nationwide except in northern Japan. In particular, the value for

Okinawa/Amami was the highest since records began in winter 1946/47, at 1.8°C over the normal. Seasonal snowfall amounts were significantly below normal on the Sea of Japan side. In particular, the value for the Sea of Japan side of western Japan was the lowest since records began in winter 1961/62, at 7% of the normal.

### (2) Spring (March – May 2019)

- Mean temperatures were significantly above normal in northern and western Japan and in Okinawa/Amami, and above normal in eastern Japan.
- Precipitation was significantly below normal on the Sea of Japan side of northern Japan, below normal on the Pacific side of northern Japan and in western Japan, above normal in Okinawa/Amami, and near normal in eastern Japan.
- Sunshine durations were significantly above normal in northern, eastern and western Japan, and near normal in Okinawa/Amami.

Seasonal sunshine durations were significantly above normal from northern to western Japan as a result of high-pressure systems over the country throughout the period. Values for the Sea of Japan side of northern, eastern and western Japan and the Pacific side of northern Japan were all the highest since records began in 1946. Seasonal precipitation was significantly below normal on the Sea of Japan side of northern Japan. Seasonal mean temperatures were significantly above normal in northern and western Japan and in Okinawa/Amami and above normal in eastern Japan due to the influence of many days with strong sunshine and inflows of warm air masses.

### (3) Summer (June – August 2019)

- Mean temperatures were above normal in northern and eastern Japan and in Okinawa/Amami, and near normal in western Japan.
- Precipitation was significantly above normal on the Pacific side of western Japan and in Okinawa/Amami, above normal on the Pacific side of eastern Japan and on the Sea of Japan side of western Japan, and near normal in northern Japan and on the Sea of Japan side of eastern Japan.
- Sunshine durations were significantly below normal in Okinawa/Amami, below normal on the Pacific side of eastern Japan and in western Japan, and near normal in northern Japan and on the Sea of Japan side of eastern Japan.

In July, the rainy season ended later than usual in many regions because the Baiu front was south of its normal location, and cool wet conditions continued in eastern Japan and elsewhere. Extremely high temperatures continued from late July to the first half of August, particularly in eastern Japan, due to the Subtropical High over the country. Seasonal temperatures were above normal in northern and eastern Japan and in Okinawa/Amami. Western Japan experienced occasional heavy rain due to the influence of stationary fronts and typhoons. Record rainfall in southern Kyushu in July and in northern Kyushu in July and August caused serious damage, including landslides and floods. Seasonal precipitation was significantly above normal on the Pacific side of western Japan. In Okinawa/Amami, seasonal precipitation was significantly above normal and seasonal sunshine durations were significantly below normal due to the influence of the Baiu front, typhoons and moist air flows.

### (4) Autumn (September – November 2019)

- Mean temperatures were significantly above normal in eastern and western Japan, and above normal in northern Japan and Okinawa/Amami.
- Precipitation was below normal on the Sea of Japan side of northern and eastern Japan, and above normal in the Pacific side of northern and eastern Japan and in Okinawa /Amami, and near normal in western Japan.
- Sunshine durations were significantly above normal on the Pacific side of northern and western Japan, above normal on the Sea of Japan side of northern and western Japan and in eastern Japan, and near normal in Okinawa /Amami.

Seasonal mean temperatures were above normal nationwide as a result of high-pressure systems with warm air masses over Japan throughout the period. In particular, values for eastern and western Japan were the highest since records began in 1946 due to the inflow of southern warm-air masses. Seasonal sunshine durations were above normal from northern to western Japan. In early September, heavy rainfall and record storm conditions were observed on the Pacific side of eastern Japan, with serious damage in Chiba Prefecture, due to the influence of Typhoon Faxai. In mid-October, record heavy rainfall was observed over a wide area from eastern Japan to the Tohoku region, causing severe damage including flooding of multiple rivers due to the influence of Typhoon Hagibis. In late-October, heavy rainfall was observed again in the Kanto Koshin and Tohoku districts, causing serious damage including flooding and landslides, due to the influence of cyclones. Typhoons Lingling, Tapah, Mitag, Neoguri and Fung-Wong approached or passed over Okinawa/Amami during the season, bringing heavy rain and storm conditions.

#### (5) Early Winter (December 2019)

Monthly temperatures in December 2019 were near normal in northern Japan, significantly above normal in eastern and western Japan and above normal in Okinawa/Amami due to a weaker-than-normal winter monsoon. Monthly snowfall amounts were significantly below normal on the Sea of Japan side of mainland Japan.

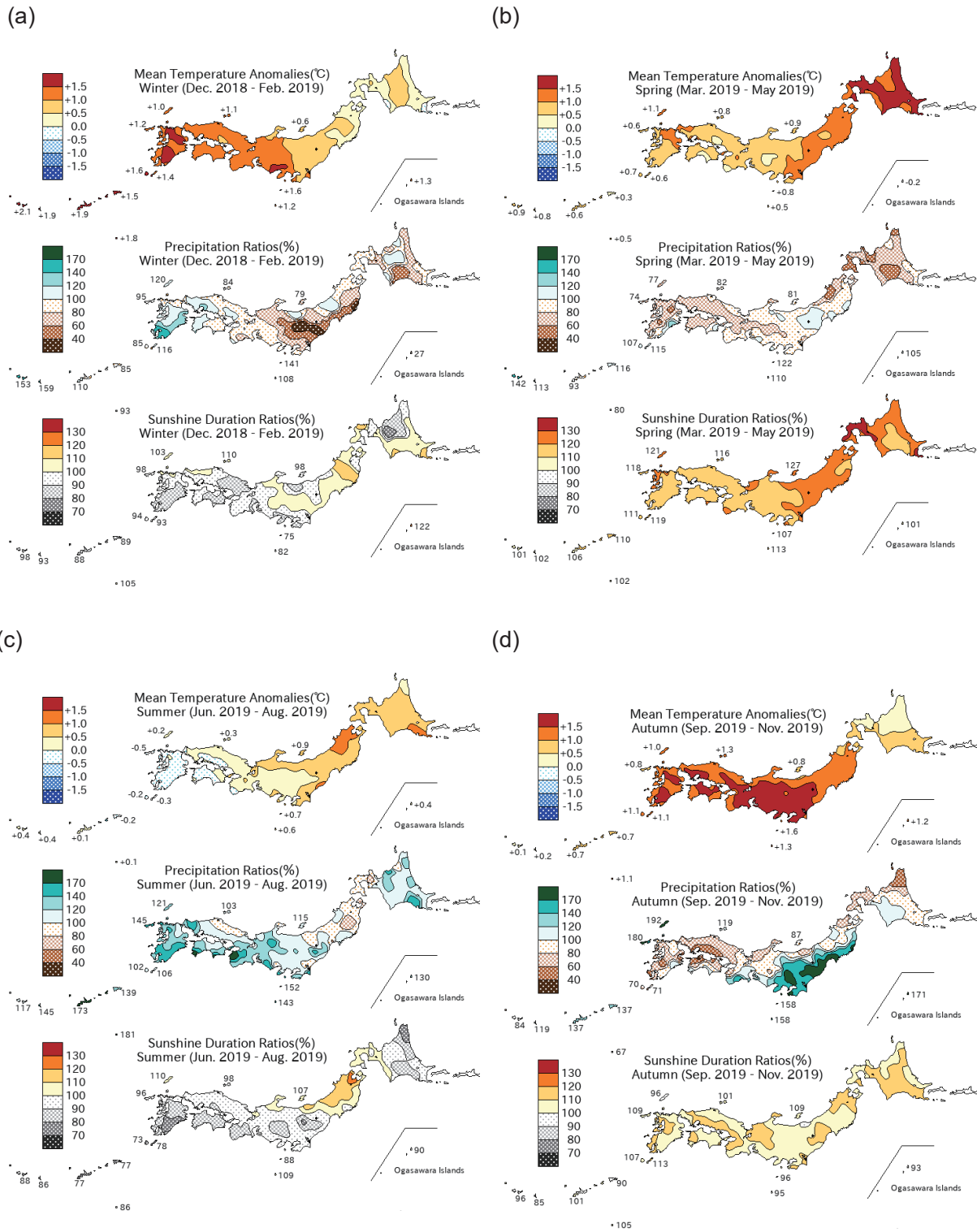


Figure 1.2-3 Seasonal anomalies/ratios for Japan in 2019

(a) Winter (December 2018 to February 2019), (b) spring (March to May 2019), (c) summer (June to August 2019), (d) autumn (September to November 2019). The base period for the normal is 1981 – 2010.

Table 1.2-1 Number of observatories reporting record(include tie record) monthly and annual mean temperatures, precipitation amounts and sunshine durations (2019)

From 153 surface meteorological stations across Japan.

	Temperature		Precipitation amount		Sunshine duration	
	Highest	Lowest	Heaviest	Lightest	Longest	Shortest
January				6	1	
February	9			1		9
March	1					
April				1	5	
May	28		1	4	51	
June	1		2			1
July			2			2
August	4		1			
September	19		1	3	2	1
October	50		16	1	1	
November				9	10	
December	5			2		
year	22		2	2	3	

### 1.3 Atmospheric circulation and oceanographic conditions<sup>6</sup>

- The El Niño event that emerged in autumn 2018 persisted until spring 2019, which may have contributed to the rising tendency of the global average temperature in the troposphere during the first half of 2019.
- In the Indian Ocean, remarkably positive SST anomalies were widely observed in the western part and remarkably negative SST anomalies were observed in the southeastern part, indicating typical characteristics of a positive Indian Ocean Dipole from summer to autumn 2019. In association with these anomaly patterns, tropical convection was enhanced over the western tropical Indian Ocean, and was suppressed from the eastern Indian Ocean to the Maritime Continent.

Monitoring of atmospheric and oceanographic conditions (e.g., upper air flow, tropical convective activity, sea surface temperatures (SSTs) and the Asian monsoon) is key to understanding the causes of extreme weather events<sup>7</sup>. This section briefly outlines the characteristics of atmospheric circulation and oceanographic conditions seen in 2019.

#### 1.3.1 Characteristics of individual seasons<sup>8</sup>

##### (1) Winter (December 2018 – February 2019)

The El Niño event that emerged in autumn 2018 peaked in winter 2018/2019 (see Section 2.6.1). SSTs were higher than normal along most of the equator, and remarkably positive anomalies were observed west of the date line (Figure 1.3-1 (a)).

Tropical convection was enhanced west of the date line and suppressed from the southeastern Indian Ocean to the Maritime Continent and around the Philippines (Figure 1.3-1 (b)). In the lower troposphere of the tropical region, cyclonic circulation anomalies straddling the equator were seen from west of the date line to the central Pacific, and anti-cyclonic circulation anomalies were seen around the Philippines and over the southern Indian Ocean (Figure 1.3-1 (c)).

In the 500-hPa height field, the polar vortices were centered near the North Pole and over the Kamchatka Peninsula. Positive height anomalies were seen over the seas south of Alaska and western Europe and from eastern China to the seas east of Japan, and negative height anomalies were seen over the western USA (Figure 1.3-1 (d)). The subtropical jet stream from North Africa to Eurasia meandered, and the westerly jet stream was shifted northward of its normal position from eastern China to Japan. The sea level pressure (SLP) field indicates that the Siberian High

<sup>6</sup> See the Glossary for terms relating to sea surface temperature variations and monsoon.

<sup>7</sup> The main charts used for monitoring of atmospheric circulation and oceanographic conditions are: sea surface temperature (SST) maps representing SST distribution for monitoring of oceanographic variability elements such as El Niño/La Niña phenomena; outgoing longwave radiation (OLR) maps representing the strength of longwave radiation from the earth's surface under clear sky conditions into space or from the top of clouds under cloudy conditions into space for monitoring of convective activity; 850-hPa stream function maps representing air flow in the lower troposphere for monitoring of atmospheric circulation variability elements such as the Pacific High and the monsoon trough associated with the Asian summer monsoon; 500-hPa height maps representing air flow at a height of approximately 5,500 meters for monitoring of atmospheric circulation variability elements such as westerly jet streams and the Arctic Oscillation; sea level pressure maps representing air flow and pressure systems on the earth's surface for monitoring of the Pacific High, the Siberian High, the Arctic Oscillation and other phenomena; 850-hPa temperature maps representing air temperature at a height of approximately 1,500 meters; and temperature calculated from thickness in the troposphere for monitoring of mean temperature of the troposphere.

<sup>8</sup> JMA publishes Monthly Highlights on the Climate System including information on the characteristics of climatic anomalies and extreme events around the world, atmospheric circulation and oceanographic conditions. It can be found at <https://ds.data.jma.go.jp/tcc/tcc/products/clisys/highlights/index.html>.

was stronger than usual over its normal position, and that the Aleutian Low was shifted northwestward. As a result, typical winter pressure patterns around Japan did not persist during the season, especially in the southern part (Figure 1.3-1 (e)). Temperatures at 850 hPa were above normal over Alaska, the southeastern USA and from southern China to the seas south of Japan, and were below normal over the western USA (Figure 1.3-1 (f)).

### (2) Spring (March – May 2019)

The El Niño event persisted until spring 2019. In the equatorial Pacific, remarkably positive SST anomalies were observed over most of the region except the area near Indonesia and east of 90°W. In the Indian Ocean, remarkably positive SST anomalies were observed over most of the region except for the southwestern coast of Australia (Figure 1.3-2 (a)).

Tropical convection was enhanced from west of the date line to the central equatorial Pacific and over the southwestern and central southern equatorial Indian Ocean, and was suppressed from the northern tropical Indian Ocean to the Philippines, over the southeastern tropical Indian Ocean and over the western and central tropical South Pacific (Figure 1.3-2 (b)). In the lower troposphere of the tropical region, cyclonic circulation anomalies straddling the equator were seen around the western tropical Pacific, and anti-cyclonic circulation anomalies were seen over the northern Indian Ocean (Figure 1.3-2 (c)).

In the 500-hPa height field, positive anomalies were seen over Alaska and east of Greenland, and negative anomalies were seen south of Greenland. The westerly jet stream was shifted southward of its normal position from Japan to the eastern part of the North Pacific (Figure 1.3-2 (d)). Positive SLP anomalies were seen over the northwestern USA and eastern Greenland, and negative SLP anomalies were seen from south of Greenland to northern Canada, and from the Kara Sea to the Bering Sea (Figure 1.3-2 (e)). Temperatures at 850 hPa were above normal over Central and Eastern Siberia, over Alaska and around Greenland, and below normal from eastern Canada to southern Greenland (Figure 1.3-2 (f)).

### (3) Summer (June – August 2019)

SST anomalies were remarkably positive near the date line in the equatorial Pacific. In the Indian Ocean, remarkably positive SST anomalies were observed over most of the region west of 100°E, and remarkably negative SST anomalies were observed south of Java and on the southwestern coast of Australia, indicating typical characteristics of a positive Indian Ocean Dipole (Figure 1.3-3 (a)).

Tropical convection was enhanced over Northern Africa and the southwestern tropical Indian Ocean, and was suppressed over the southeastern tropical Indian Ocean and Central America (Figure 1.3-3 (b)). In the lower troposphere over the tropical region, cyclonic circulation anomalies were seen over the northwestern part of Africa, and anti-cyclonic circulation anomalies were seen over Australia and the eastern Pacific. The monsoon trough over Southeast Asia was stronger than normal in August 2019 (Figure 1.3-3 (c)).

In the 500-hPa height field, positive anomalies were seen from west of Greenland via the northern polar region to Central Siberia and over southern Alaska and eastern Europe, and negative anomalies were seen over the seas west of Europe and over Western Russia. The westerly jet stream was stronger than normal over the seas east of Japan (Figure 1.3-3 (d)). Positive SLP anomalies were seen from Greenland to the northern polar region and from Eastern Siberia to southwestern Alaska, and negative values were seen near the UK, from Western Russia to Western

Siberia and over the latitude band of 40°N in the eastern North Pacific. The extension of the North Pacific Subtropical High (NPSH) toward mainland Japan was generally weaker than normal, moving toward mainland Japan in early August and southern Japan in late August (Figure 1.3-3 (e)). Temperatures at 850 hPa were above normal over Central Siberia, southern Alaska, west of Greenland and in Europe, and below normal over the Sea of Okhotsk, northwestern Canada, the seas west of Europe, and Western Russia (Figure 1.3-3 (f)).

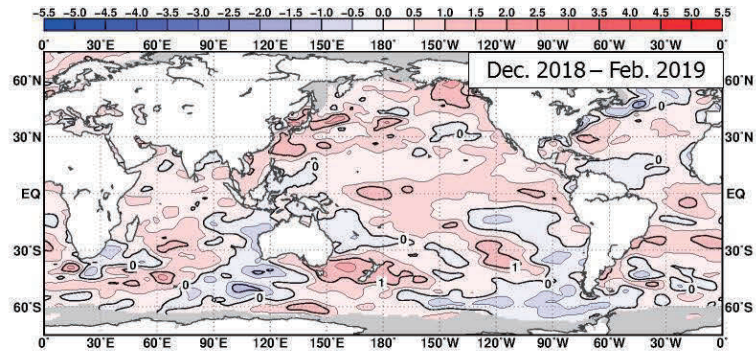
#### (4) Autumn (September – November 2019)

Remarkably positive SST anomalies were observed in the western part of the equatorial Pacific and over western and other parts of the Indian Ocean. However, remarkably negative anomalies were observed off the southwestern coast of Sumatra, representing clear characteristics of a positive Indian Ocean Dipole (Figures 1.3-4 (a)).

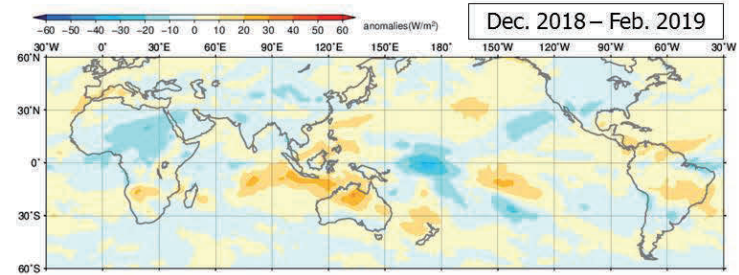
Tropical convection was enhanced from Western Africa to the western tropical Indian Ocean and over the latitude band of 10°N in the Pacific, and was suppressed from the central part of the southern equatorial Indian Ocean to the Maritime Continent (Figure 1.3-4 (b)). In the lower troposphere of the tropical region, anti-cyclonic circulation anomalies straddling the equator were seen over the central and eastern Indian Ocean (Figure 1.3-4 (c)).

Positive anomalies in the 500-hPa height field were seen over the seas south of Alaska, northern Greenland and eastern Europe, and negative values were seen over northwestern Europe. The westerly jet stream was shifted northward from its normal position over Japan (Figure 1.3-4 (d)). Positive SLP anomalies were seen over the western part of Central Asia, Japan, the area off the western coast of North America, and the seas east of Greenland, and negative values were seen from the Sea of Okhotsk to the Chukchi Sea and over Europe (Figure 1.3-4 (e)). Temperatures at 850-hPa were above normal from the Chukchi Sea to the seas south of Alaska, around Greenland and over eastern Europe, and below normal over the western USA and northern Europe (Figure 1.3-4 (f)).

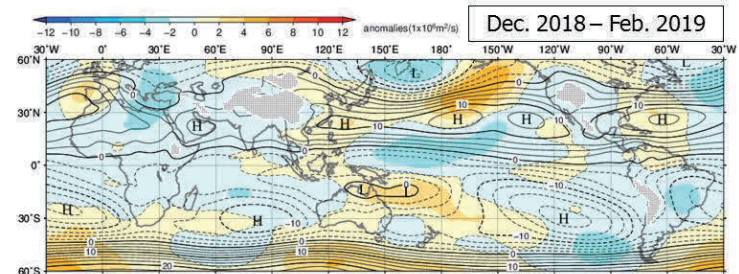
(a) SST anomaly



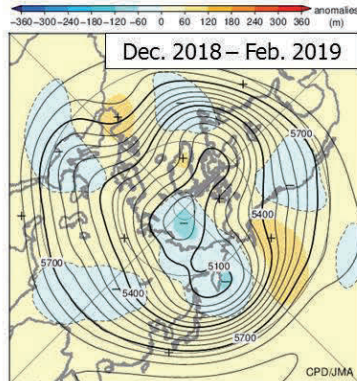
(b) OLR anomaly



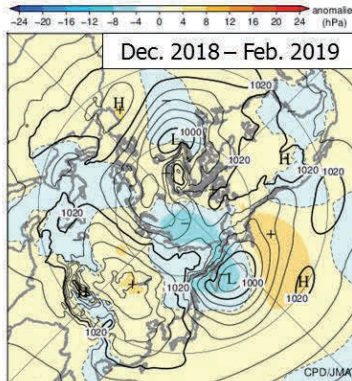
(c) 850-hPa stream function and anomaly



(d) 500-hPa height and anomaly



(e) SLP and anomaly



(f) 850-hPa temp. and anomaly

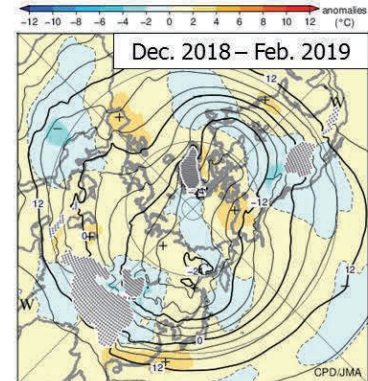
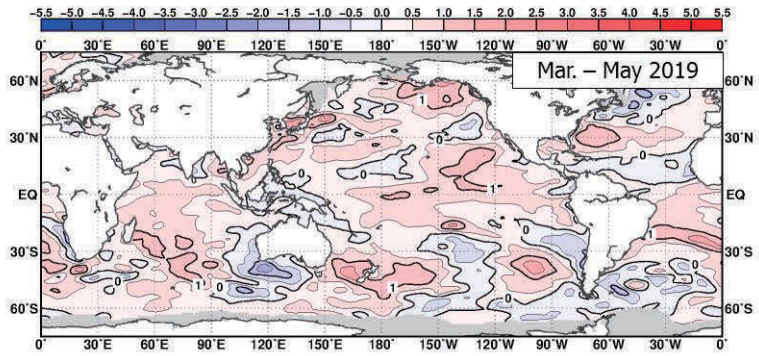


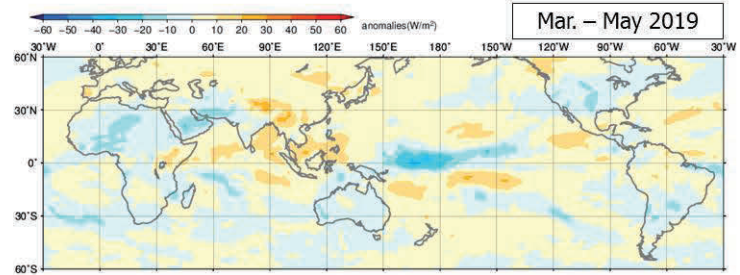
Figure 1.3-1 Three-month mean (a) sea surface temperature (SST) anomaly, (b) outgoing longwave radiation (OLR) anomaly, (c) 850-hPa stream function and anomaly, (d) 500-hPa height and anomaly in the Northern Hemisphere (NH), (e) sea level pressure (SLP) and anomaly in NH, and (f) 850-hPa temperature and anomaly in NH (December 2018 – February 2019)

The base period for the normal is 1981 – 2010. (a) The contour interval is  $0.5^{\circ}\text{C}$ . Sea ice coverage areas are shaded in gray. (b) Negative (cold color) and positive (warm color) OLR anomalies show enhanced and suppressed convection, respectively, compared to the normal. (c) The contour interval is  $2.5 \times 10^6 \text{ m}^2 \text{ per s}$ . “H” and “L” denote high- and low-pressure systems, respectively. Original data provided by NOAA. (d) Contours show 500-hPa height at intervals of 60 m, and shading indicates height anomalies. “H” and “L” denote high- and low-pressure systems, respectively. (e) Contours show sea level pressure at intervals of 4 hPa, and shading indicates sea level pressure anomalies. “H” and “L” denote high- and low-pressure systems, respectively. (f) Contours show temperature at intervals of 4 degree C, and shading indicates temperature anomalies. “W” and “C” denote warm and cold conditions, respectively.

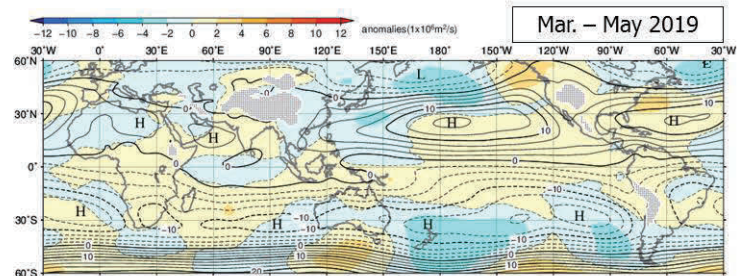
(a) SST anomaly



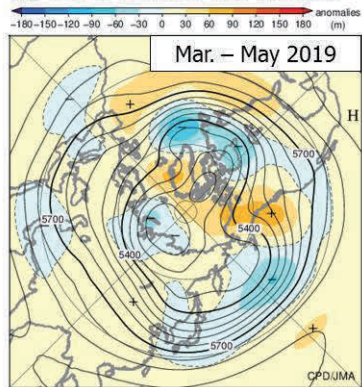
(b) OLR anomaly



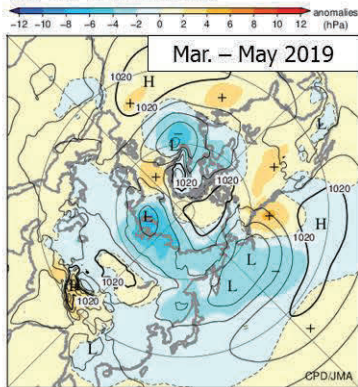
(c) 850-hPa stream function and anomaly



(d) 500-hPa height and anomaly



(e) SLP and anomaly



(f) 850-hPa temp. and anomaly

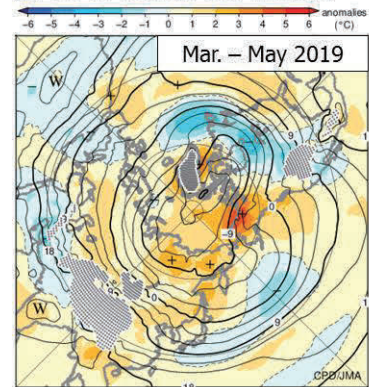
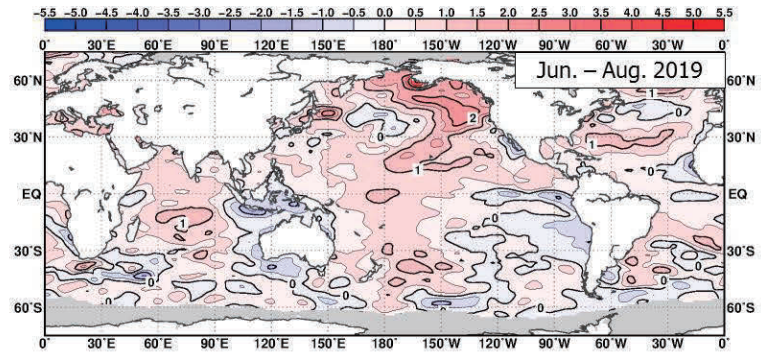
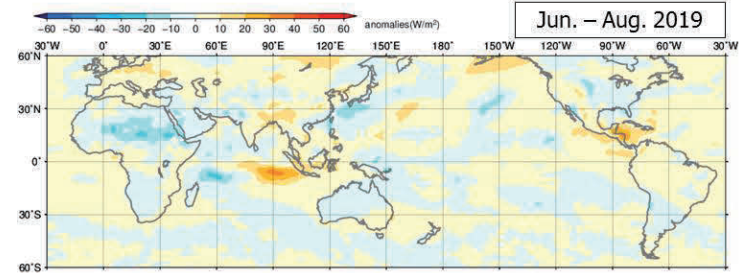


Figure 1.3-2 As per Figure 1.3-1, but for March – May 2019  
In (f), contour interval is 3 degree C.

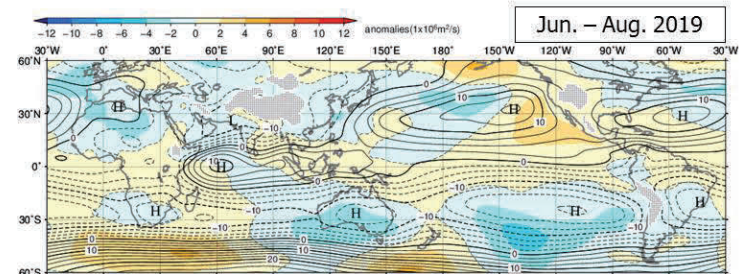
(a) SST anomaly



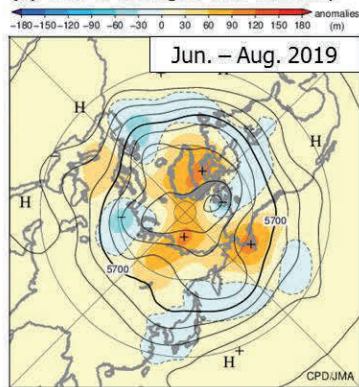
(b) OLR anomaly



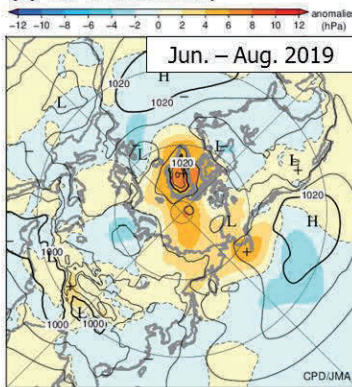
(c) 850-hPa stream function and anomaly



(d) 500-hPa height and anomaly



(e) SLP and anomaly



(f) 850-hPa temp. and anomaly

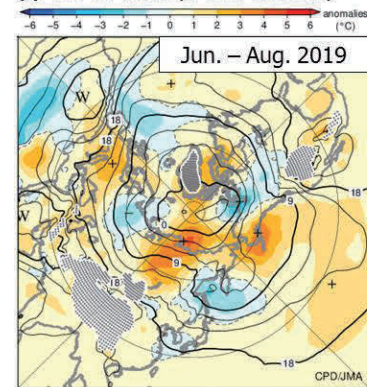
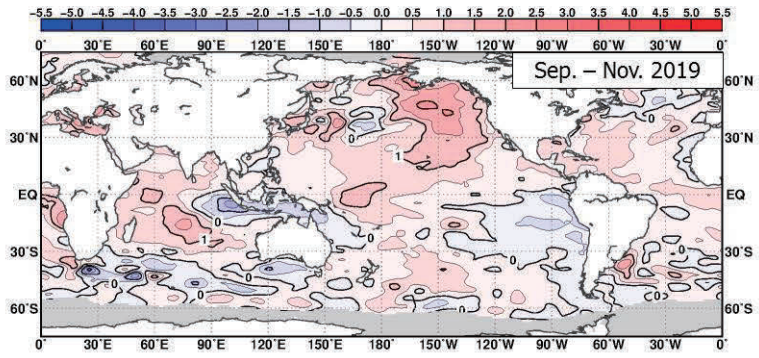
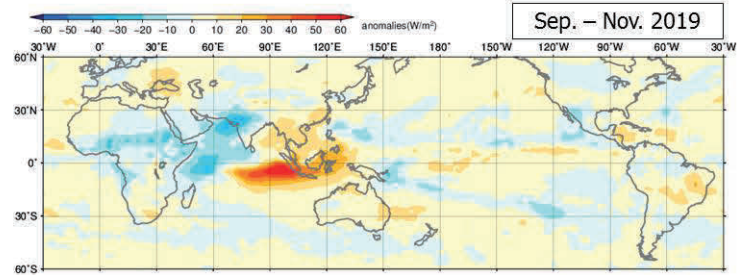


Figure 1.3-3 As per Figure 1.3-1, but for June – August 2019  
In (f), contour interval is 3 degree C.

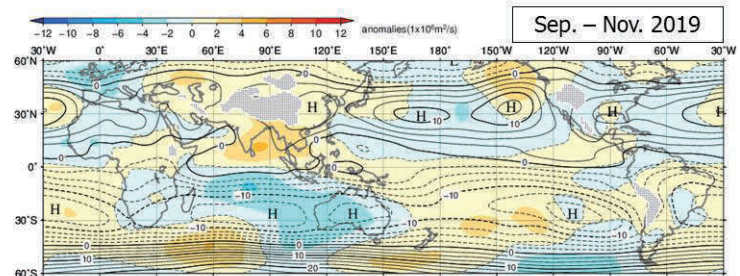
(a) SST anomaly



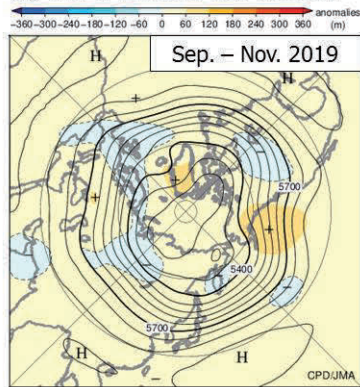
(b) OLR anomaly



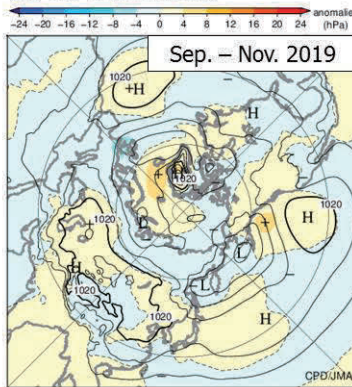
(c) 850-hPa stream function and anomaly



(d) 500-hPa height and anomaly



(e) SLP and anomaly



(f) 850-hPa temp. and anomaly

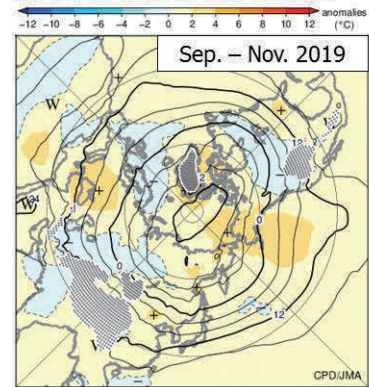


Figure 1.3-4 As per Figure 1.3-1, but for September – November 2019

### 1.3.2 Global average temperature in the troposphere

The global average temperature in the troposphere (Figure 1.3-5) peaked in spring 2016 before decreasing until spring 2018 and then following a rising tendency. Values in June and November 2019 were the highest on record for those months since 1958 (Figure 1.3-6). The rising tendency seen during the first half of 2019 may be attributable to the El Niño event that occurred from autumn 2018 to spring 2019, which may have contributed to 2019’s second-highest annual anomaly of the global average surface temperature since 1891.

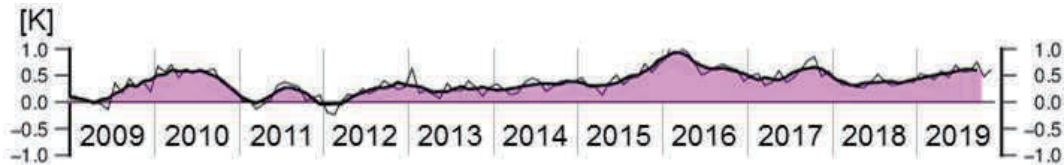


Figure 1.3-5 Time-series representation of global average temperature anomalies calculated from thickness in the troposphere (2009 to 2019)

The thin and thick lines show monthly mean and five-month running mean values, respectively. The base period for the normal is 1981 – 2010.

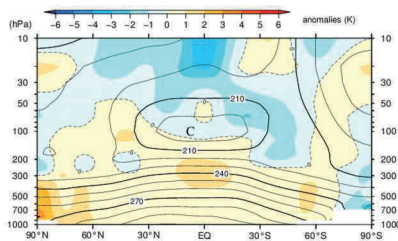


Figure 1.3-6 Latitude-height cross section of zonal mean temperature and anomaly (June 2019)

Contours show zonal mean temperature at intervals of 10 K, and shading indicates temperature anomalies. The base period for the normal is 1981 – 2010. “W” and “C” denote warm and cold conditions, respectively.

### 1.3.3 Asian summer monsoon

Convection during the 2019 Asian summer monsoon season (June – September) was generally suppressed, while enhancement was seen in early and late August as indicated by OLR index values (SAMOI (A))<sup>9</sup>, JMA, 1997; Figure 1.3-7). Convection around the Philippines was suppressed from June to mid-July (in line with slower-than-normal northward movement of the Baiu front) and was enhanced from late July to early August, which may have been a factor in the extension of the North Pacific Subtropical High (NPSH) toward mainland Japan.

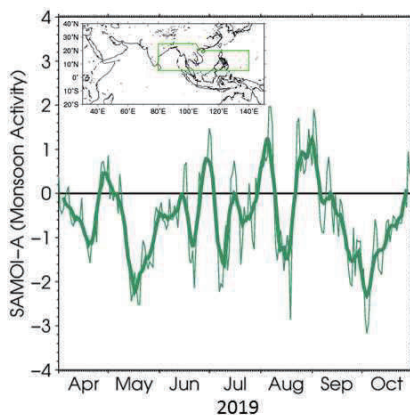


Figure 1.3-7 Time-series representation of the Asian summer monsoon OLR index (SAMOI (A)) (April – October 2019)

The thin and thick green lines indicate daily and seven-day running mean values, respectively. SAMOI (A) indicates the overall activity of the Asian summer monsoon, and positive and negative values indicate enhanced and suppressed convective activity, respectively, compared to the normal. The base period for the normal is 1981 – 2010. Original OLR data provided by NOAA.

<sup>9</sup> SAMOI (A) is defined as reversed-sign area-averaged OLR anomalies normalized by its standard deviation. The area for average is enclosed by green line in the map of Figure 1.3-7.

### 1.3.4 Tropical cyclones over the western North Pacific and the South China Sea

In 2019, 29 tropical cyclones (TCs) with maximum wind speeds of  $\geq 34$  kt<sup>10</sup> formed over the western North Pacific and the South China Sea (Figure 1.3-8, Table 1.3-1), which was above the normal of 25.6 (1981 – 2010 average). The first named TC of 2019, Pabuk, formed at 15 JST<sup>11</sup> on 1 January, which was the earliest formation of the first named TC of the year since records began in 1951 and the first-ever formation on 1 January. After the formation of the second named TC of the year (Wutip), no TCs formed from March to mid-June, which may be attributable to the suppression of convective activity over the tropics in the western North Pacific and the South China Sea during the term. A total of 26 TCs formed from July to December 2019, which was above the normal of 21 (1981 – 2010 average). A total of 6 TCs formed in November 2019, which tied with 1964 and 1991 as the highest on record for the month since 1951.

A total of 15 TCs came within 300 km of the Japanese archipelago, which was above the normal of 11.4. A total of 5 TCs (Nari, Francisco, Krosa, Faxai and Hagibis) made landfall on Japan, exceeding the normal of 2.7.

TC Faxai made landfall around the city of Chiba in Chiba Prefecture on 9 September (JST) and brought unusually strong winds, causing particular damage to the area around the Boso Peninsula. It made landfall with a maximum wind speed of 80 kt, which was the strongest for a TC over the Kanto region since records began in 1991. TC Hagibis made landfall on the Izu Peninsula on 12 October (JST) with a maximum wind speed of 80 kt, which was the strongest for a TC over eastern Japan since 1991.

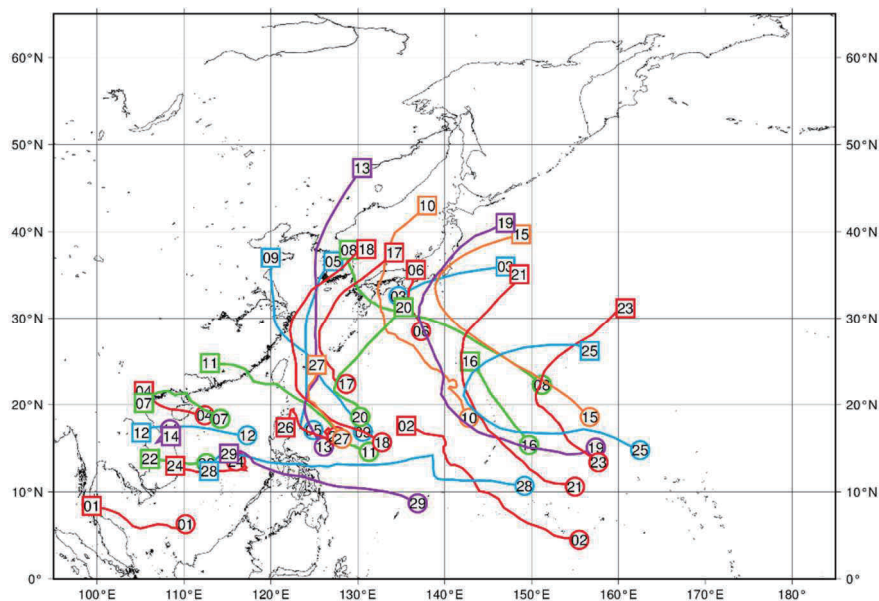


Figure 1.3-8 Tracks of TCs with maximum wind speeds of  $\geq 34$  kt in 2019

Numbered circles indicate positions of the TC formed (maximum wind speeds of  $\geq 34$  kt), and numbered squares indicate positions of the TC dissipated (maximum wind speeds lower than 34 kt). Source: RSMC Tokyo-Typhoon Center data

10 One knot (kt) is about 0.51 m/s.

11 Japan Standard Time (JST) is defined to set nine hours forward of UTC.

Table 1.3-1 TCs with maximum wind speeds of  $\geq 34$  kt in 2019 (Source: RSMC Tokyo-Typhoon Center data)

Number ID	Tropical Cyclone	Duration (UTC)	Maximum Wind <sup>1)</sup> (kt)	Number ID	Tropical Cyclone	Duration (UTC)	Maximum Wind <sup>1)</sup> (kt)
1901	PABUK	0600, 01 Jan - 1800, 04 Jan	45	1916	PEIPAH	0000, 15 Sep - 1200, 16 Sep	35
1902	WUTIP	1800, 19 Feb - 0600, 28 Feb	105	1917	TAPAH	0000, 19 Sep - 0000, 23 Sep	65
1903	SEPAT	1200, 27 Jun - 0600, 28 Jun	40	1918	MITAG	0000, 28 Sep - 0600, 03 Oct	75
1904	MUN	0600, 02 Jul - 0600, 04 Jul	35	1919	HAGIBIS	1800, 05 Oct - 0300, 13 Oct	105
1905	DANAS	0600, 16 Jul - 1800, 20 Jul	45	1920	NEOGURI	0000, 17 Oct - 1200, 21 Oct	75
1906	NARI	1800, 25 Jul - 0600, 27 Jul	35	1921	BUALOI	0600, 19 Oct - 1200, 25 Oct	100
1907	WIPHA	1800, 30 Jul - 1200, 03 Aug	45	1922	MATMO	1800, 29 Oct - 0600, 31 Oct	50
1908	FRANCISCO	1200, 02 Aug - 0000, 07 Aug	70	1923	HALONG	1200, 02 Nov - 0000, 09 Nov	115
1909	LEKIMA	0600, 04 Aug - 1800, 12 Aug	105	1924	NAKRI	1800, 05 Nov - 0000, 11 Nov	65
1910	KROSA	0600, 06 Aug - 1200, 16 Aug	75	1925	FENGSHEN	0000, 12 Nov - 1200, 17 Nov	85
1911	BAILU	0600, 21 Aug - 1800, 25 Aug	50	1926	KALMAEGI	1200, 14 Nov - 0000, 20 Nov	70
1912	PODUL	0000, 28 Aug - 0000, 30 Aug	40	1927	FUNG-WONG	0000, 20 Nov - 1200, 22 Nov	55
1913	LINGLING	0000, 02 Sep - 0000, 08 Sep	95	1928	KAMMURI	0000, 26 Nov - 1800, 05 Dec	90
1914	KAJIKI	1200, 02 Sep - 1200, 03 Sep	35	1929	PHANFONE	1200, 22 Dec - 0000, 28 Dec	80
1915	FAXAI	1800, 04 Sep - 0000, 10 Sep	85				

1) Estimated maximum 10-minute mean wind speed

## Chapter 2 Climate Change

### 2.1 Changes in temperature<sup>12</sup>

- The annual anomaly of the global average surface temperature in 2019 was +0.43°C, the 2nd highest since 1891. On a longer time scale, it is virtually certain that the annual global average surface temperature has risen at rates of 0.74°C per century.
- The annual anomaly of the average temperature over Japan was +0.92°C, the highest since 1898. On a longer time scale, it is virtually certain that the annual average temperature over Japan has risen at rates of 1.24°C per century.
- It is virtually certain that the annual number of days with maximum temperatures of 35 °C or higher ( $T_{\max} \geq 35^{\circ}\text{C}$ ) and that with minimum temperatures of 25°C or higher ( $T_{\min} \geq 25^{\circ}\text{C}$ ) have increased, while the annual number of days with minimum temperatures below 0°C ( $T_{\min} < 0^{\circ}\text{C}$ ) has decreased.

#### 2.1.1 Global surface temperature

The annual anomaly of the global average surface temperature in 2019 (i.e., the combined average of the near-surface air temperature over land and the SST) was +0.43°C above the 1981 – 2010 average. This was the 2nd highest since 1891. The years from 2014 to 2019 were the top-six warmest on record in terms of global temperature. The global average temperature fluctuates on different time scales ranging from years to decades. On a longer time scale, it is virtually certain that the global average surface temperature has risen at a rate of 0.74°C per century<sup>13</sup> (statistically significant at a confidence level of 99%<sup>14</sup>).

The surface temperature anomalies over the Northern Hemisphere and the Southern Hemisphere were +0.57°C (the 3rd highest) and +0.30°C (the 2nd highest) above the 1981 – 2010 average, respectively (Figure 2.1-1). It is virtually certain that average surface temperatures over the Northern Hemisphere and the Southern Hemisphere have risen at rates of 0.80°C and 0.70°C per century, respectively (both statistically significant at a confidence level of 99%).

Linear temperature trends for 5° × 5° latitude/longitude grid boxes indicate that most areas of the world, especially in the high latitudes of the Northern Hemisphere, have experienced long-term warming (Figure 2.1-2). These long-term trends in annual average temperatures can be largely attributed to global warming caused by increased concentrations of greenhouse gases such as CO<sub>2</sub>. On a shorter time scale, temperatures fluctuate due to the influence of natural climate dynamics over different time scales ranging from years to decades.

<sup>12</sup> Monthly, seasonal and annual estimates of mean temperatures averaged over the globe and Japan are published on JMA's website.

<https://www.data.jma.go.jp/cpdinfo/temp/index.html> (Japanese)

<https://ds.data.jma.go.jp/tcc/tcc/products/gwp/gwp.html> (English)

<sup>13</sup> According to IPCC AR5, the global average surface temperature has risen about 0.85°C (The 90% uncertainty interval is 0.65 to 1.06°C) over the period 1880 to 2012. The values given in IPCC AR5 and those in this report are considered to show no remarkable difference that have risen on a longer time scale and are higher since the mid-1990s, although they do not correspond exactly because of differences in dataset calculation methods and the statistical period examined.

<sup>14</sup> For evaluation and clarification of the significance statistics used here, see “Explanatory note on detection of statistical significance in long-term trends” at the end of the report.

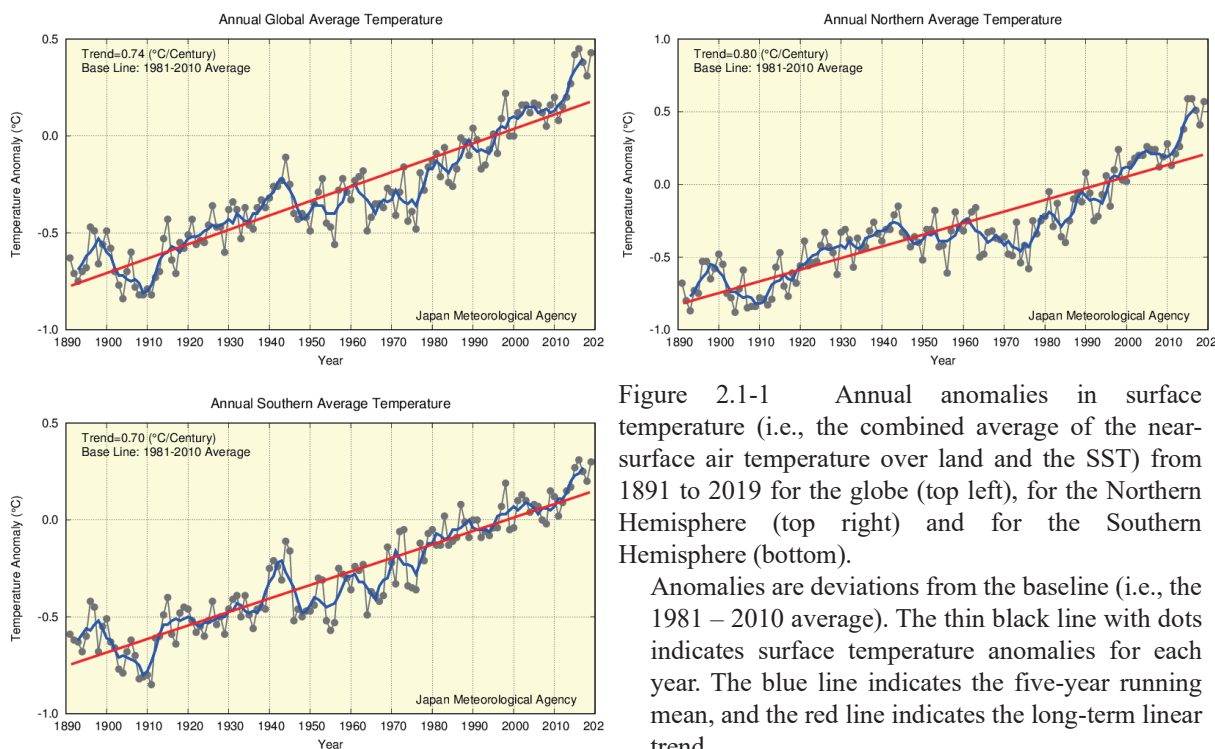


Figure 2.1-1 Annual anomalies in surface temperature (i.e., the combined average of the near-surface air temperature over land and the SST) from 1891 to 2019 for the globe (top left), for the Northern Hemisphere (top right) and for the Southern Hemisphere (bottom).

Anomalies are deviations from the baseline (i.e., the 1981 – 2010 average). The thin black line with dots indicates surface temperature anomalies for each year. The blue line indicates the five-year running mean, and the red line indicates the long-term linear trend.

Trends of surface temperature (1891-2019)

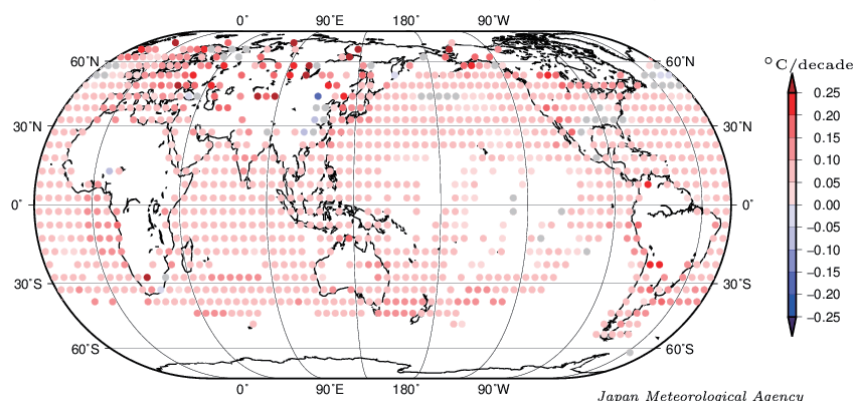


Figure 2.1-2 Linear temperature trends for  $5^{\circ} \times 5^{\circ}$  latitude/longitude grid boxes for the period of 1891 to 2019

The grid boxes with gray circles have no statistically significant trend (not statistically significant at a confidence level of 90%). Blank areas indicate those with insufficient data to analyze long-term trends.

### 2.1.2 Surface temperature over Japan

Long-term changes in the surface temperature over Japan are analyzed using observational records dating back to 1898. Table 2.1-1 lists the meteorological stations whose data are used to derive annual mean surface temperatures.

Table 2.1-1 Observation stations whose data are used to calculate surface temperature anomalies over Japan  
Miyazaki and Iida were relocated in May 2000 and May 2002, respectively, and their temperatures have been adjusted to eliminate the influence of the relocation.

Element	Observation stations
Temperature (15 stations)	Abashiri, Nemuro, Suttsu, Yamagata, Ishinomaki, Fushiki, Iida, Choshi, Sakai, Hamada, Hikone, Tadotsu, Miyazaki, Naze, Ishigakijima

The mean surface temperature in Japan for 2019 is estimated to have been 0.92°C above the 1981 – 2010 average, which is the highest since 1898 (Figure 2.1-3). The surface temperature fluctuates on different time scales ranging from years to decades. On a longer time scale, it is virtually certain that the annual mean surface temperature over Japan has risen at a rate of 1.24°C per century (statistically significant at a confidence level of 99%). Similarly, it is virtually certain that the seasonal mean temperatures for winter, spring, summer and autumn have risen at rates of about 1.13, 1.47, 1.11 and 1.23°C per century, respectively (all statistically significant at a confidence level of 99%).

It is noticeable from Figure 2.1-3 that the annual mean temperature remained relatively low before the 1940s, started to rise and reached a local peak around 1960, entered a cooler era through to the mid-1980s and then began to show a rapid warming trend in the late 1980s. The warmest years on record have all been observed since the 1990s.

The high temperatures seen in recent years have been influenced by fluctuations over different time scales ranging from years to decades, as well as by global warming resulting from increased concentrations of greenhouse gases such as CO<sub>2</sub>.

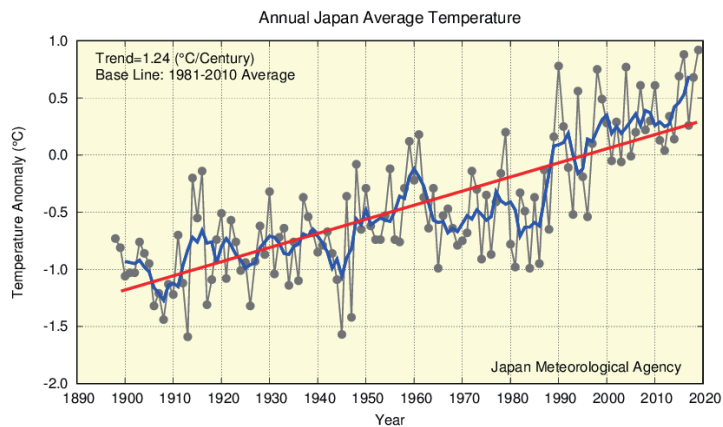


Figure 2.1-3 Annual surface temperature anomalies from 1898 to 2019 in Japan.

Anomalies are deviations from the baseline (i.e., the 1981 – 2010 average). The thin black line indicates the surface temperature anomaly for each year. The blue line indicates the five-year running mean, and the red line indicates the long-term linear trend.

### 2.1.3 Long-term trends of extreme temperature events<sup>15</sup> in Japan

This section describes long-term trends of extremely high/low-temperature events in Japan, as derived from analysis of temperature records from the 15 observation stations. Though monthly mean temperatures of the stations in Miyazaki and Iida have been adjusted to eliminate the influence of their relocation, records from these two stations are not used for analysis of daily temperatures due to the difficulty of adjustment in regard to the relocation.

#### (1) Long-term trends of monthly extreme temperatures

It is virtually certain that the frequency of extremely high monthly temperatures has increased, while that of extremely low monthly temperatures has decreased (both statistically significant at the confidence level of 99%) (Figure 2.1-4). The frequency of extremely high monthly temperatures has largely increased since about 1990.

<sup>15</sup> Here, judgment of extremely high/low temperatures is based on the fourth-highest/lowest monthly values on records over the 119-year period from 1901 to 2019. The frequency of occurrence of the highest/lowest to the fourth-highest/lowest values over this period is once approximately every 30 years, which is close to JMA's definition of extreme climate events as those occurring once every 30 years or longer (See the Glossary for terms relating to Extreme climate event).

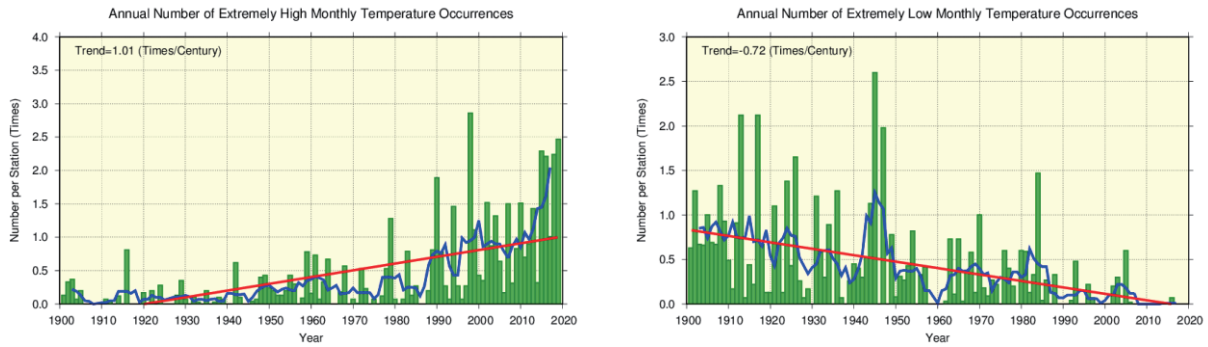


Figure 2.1-4 Annual number of extremely high/low monthly mean temperature occurrences from 1901 to 2019  
 The graphs show the annual number of occurrences of the highest/lowest first-to-forth values for each month during the period from 1901 to 2019. The green bars indicate annual occurrences of extremely high/low monthly mean temperatures divided by the total number of monthly observation data sets available for the year (i.e., the average occurrence per station). The blue line indicates the five-year running mean, and the straight red line indicates the long-term linear trend.

(2) Annual number of days with maximum temperatures of  $\geq 30^{\circ}\text{C}$  and  $\geq 35^{\circ}\text{C}$

The annual number of days with maximum temperatures ( $T_{\max}$ ) of  $\geq 30^{\circ}\text{C}$  and  $T_{\max} \geq 35^{\circ}\text{C}$  is virtually certain to have increased (both statistically significant at a confidence level of 99%) (Figure 2.1-5). Especially, the annual number of days with  $T_{\max} \geq 35^{\circ}\text{C}$  has largely increased since about mid-1990s.

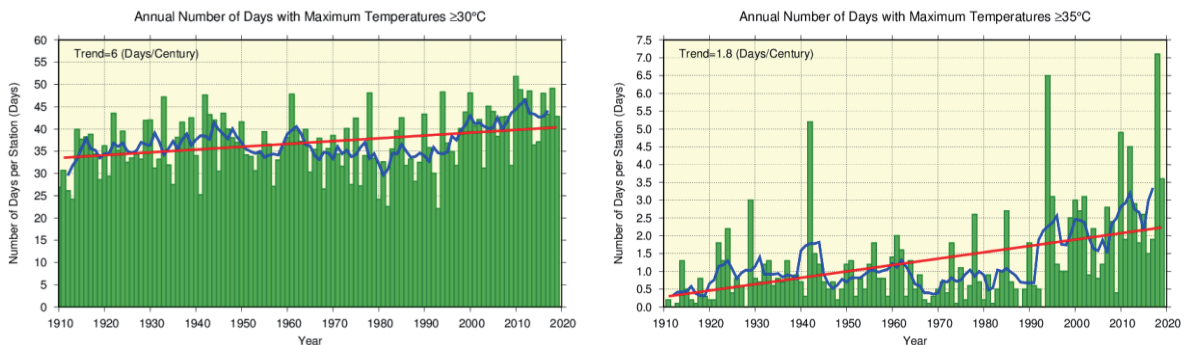


Figure 2.1-5 Annual number of days with maximum temperatures of  $\geq 30^{\circ}\text{C}$  and  $\geq 35^{\circ}\text{C}$  from 1910 to 2019  
 The green bars indicate the annual number of days per station for each year. The blue line indicates the five-year running mean, and the straight red line indicates the long-term linear trend.

(3) Annual number of days with minimum temperatures of  $< 0^{\circ}\text{C}$  and  $\geq 25^{\circ}\text{C}$

It is virtually certain that the annual number of days with minimum temperatures ( $T_{\min}$ ) of  $< 0^{\circ}\text{C}$  has decreased, while the annual number of days with  $T_{\min} \geq 25^{\circ}\text{C}$  has increased (both statistically significant at a confidence level of 99%) (Figure 2.1-6).

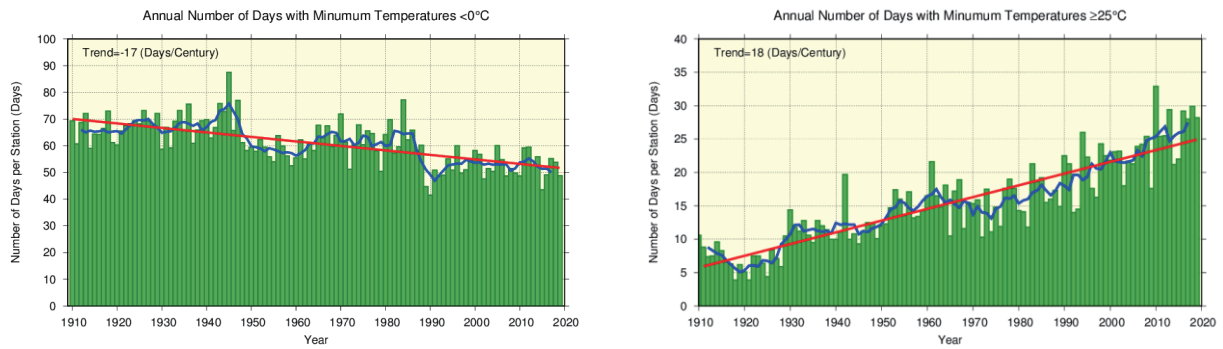


Figure 2.1-6 Annual number of days with minimum temperatures of  $<0^{\circ}\text{C}$  and  $\geq 25^{\circ}\text{C}$  from 1910 to 2019  
As per Figure 2.1-5.

#### 2.1.4 Urban heat island effect at urban stations in Japan

The long-term trends of annual average temperatures are more pronounced for urban observation stations whose data are homogeneous over a long period (Sapporo, Sendai, Niigata, Tokyo, Yokohama, Nagoya, Kyoto, Osaka, Hiroshima, Fukuoka, Kagoshima) than for the average of the 15 rural observation stations (Table 2.1-2 and Figure 2.1-7).

Table 2.1-2 Long-term trends of annual and seasonal average temperatures at urban stations in Japan

These figures are based on data from 1927 to 2019. The trend of the 15 rural station averages (Table 2.1-1) is also listed. Values shown in italics are not statistically significant at a confidence level of 90%. For stations with asterisks (5 urban stations, and Iida and Miyazaki among the 15 rural stations), trends are calculated after adjustment to eliminate the influence of relocation.

Station	Long-term temperature trend ( $^{\circ}\text{C}/\text{century}$ )														
	Average					Daily maximum					Daily minimum				
	Ann	Win	Spr	Sum	Aut	Ann	Win	Spr	Sum	Aut	Ann	Win	Spr	Sum	Aut
Sapporo	2.6	3.3	2.9	1.8	2.4	1.0	1.4	1.7	0.5	0.4	4.4	5.6	4.7	3.3	4.1
Sendai	2.4	2.9	2.8	1.4	2.5	1.3	1.6	1.7	0.9	1.0	3.1	3.6	3.8	2.0	3.2
Niigata*	2.0	2.2	2.6	1.4	1.8	2.0	2.6	2.8	0.9	1.6	2.2	2.3	2.7	1.9	1.8
Tokyo*	3.2	4.2	3.3	2.1	3.4	1.8	2.1	2.2	1.3	1.8	4.4	5.8	4.6	2.9	4.4
Yokohama	2.8	3.5	3.1	1.8	2.8	2.5	2.8	3.0	1.8	2.4	3.5	4.5	3.7	2.2	3.5
Nagoya	2.9	2.9	3.1	2.2	3.1	1.4	1.5	1.8	1.0	1.4	3.9	3.7	4.4	3.2	4.3
Kyoto	2.7	2.6	3.0	2.2	2.8	1.1	0.9	1.7	1.1	0.9	3.7	3.7	4.1	3.2	4.0
Osaka*	2.6	2.6	2.7	2.0	2.9	2.1	2.1	2.4	1.9	2.1	3.5	3.1	3.5	3.2	4.0
Hiroshima*	2.0	1.6	2.3	1.5	2.4	1.0	0.6	1.7	1.1	0.5	3.1	2.7	3.3	2.6	3.9
Fukuoka	3.0	2.9	3.4	2.2	3.7	1.7	1.7	2.2	1.4	1.7	4.9	4.3	5.8	3.6	6.0
Kagoshima*	2.5	2.5	2.8	2.0	2.9	1.3	1.1	1.7	1.0	1.4	3.9	3.5	4.4	3.3	4.6
15 stations*	1.5	1.6	1.9	1.1	1.5	1.1	1.2	1.7	0.8	0.9	1.9	1.8	2.1	1.6	1.9

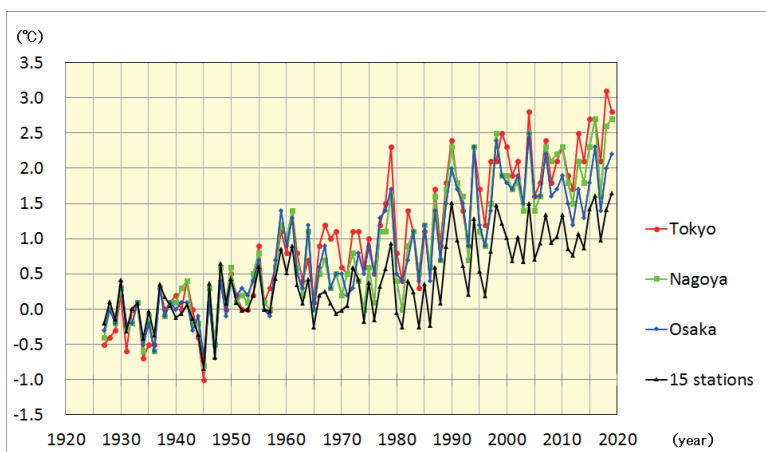


Figure 2.1-7 Annual temperature anomalies at Tokyo, Nagoya and Osaka and values averaged over 15 rural stations in Japan from 1927 to 2019

Anomalies are deviations from the baseline (i.e., the 1927 – 1956 average). Values averaged between 1927 and 1956 for respective stations all equal zero.

As it can be assumed that the long-term trends averaged over the 15 rural stations reflect large-scale climate change, the differences in the long-term trends of urban stations from the average of the 15 stations largely represent the influence of urbanization.

Detailed observation reveals that the long-term trends are more significant in winter, spring and autumn than in summer and more pronounced for minimum temperatures than for maximum temperatures at every urban observation station.

Records from urban stations whose data are not affected by relocation are used to determine long-term trends for the annual number of days with minimum temperatures of  $< 0^{\circ}\text{C}$  and  $\geq 25^{\circ}\text{C}$  and maximum temperatures of  $\geq 30^{\circ}\text{C}$  and  $\geq 35^{\circ}\text{C}$ . The number of days with  $T_{\min} < 0^{\circ}\text{C}$  is very likely to have decreased with statistical significance at all urban stations, and the number with  $T_{\min} \geq 25^{\circ}\text{C}$ ,  $T_{\max} \geq 30^{\circ}\text{C}$  and  $T_{\max} \geq 35^{\circ}\text{C}$  is very likely to have increased with statistical significance at most stations except Sapporo (Table 2.1-3).

Table 2.1-3 Long-term trends for the annual number of days with minimum temperatures of  $< 0^{\circ}\text{C}$  and  $\geq 25^{\circ}\text{C}$  and maximum temperatures of  $\geq 30^{\circ}\text{C}$  and  $\geq 35^{\circ}\text{C}$ .

These figures are based on data from 1927 to 2019. The trend of the 13 rural station averages (Table 2.1-1, excluding Iida and Miyazaki) is also listed. Values shown in italics are not statistically significant at a confidence level of 90%.

Station	Annual number of days			
	Trend (days/decade)			
	$T_{\min} < 0^{\circ}\text{C}$	$T_{\min} \geq 25^{\circ}\text{C}$	$T_{\max} \geq 30^{\circ}\text{C}$	$T_{\max} \geq 35^{\circ}\text{C}$
Sapporo	-4.3	<i>0.0</i>	<i>0.1</i>	<i>0.0</i>
Sendai	-5.7	0.4	1.0	0.1
Yokohama	-6.0	3.1	2.2	0.2
Nagoya	-6.8	3.7	1.2	1.0
Kyoto	-7.2	3.6	1.4	1.4
Fukuoka	-4.9	4.7	1.1	1.1
13 Stations	-2.0	1.8	0.6	0.2

## 2.2 Changes in precipitation<sup>16</sup>

- The annual anomaly of global precipitation (for land areas only) in 2019 was -15 mm.
- The annual anomaly of precipitation in 2019 was +35.5 mm in Japan. Annual precipitation over Japan shows no discernible long-term trend.
- The annual number of days with daily and hourly extreme precipitation has increased in Japan, while that with wet days has decreased.
- Snow depth on the Sea of Japan side has decreased.

### 2.2.1 Global precipitation over land

Annual precipitation (for land areas only) in 2019 was -15 mm above the 1981 – 2010 average (Figure 2.2-1), and the figure has fluctuated periodically since 1901. In the Northern Hemisphere, records show large amounts of rainfall around 1930, in the 1950s and after the mid-2000s. Long-term trends are not analyzed because the necessary precipitation data for sea areas are not available.

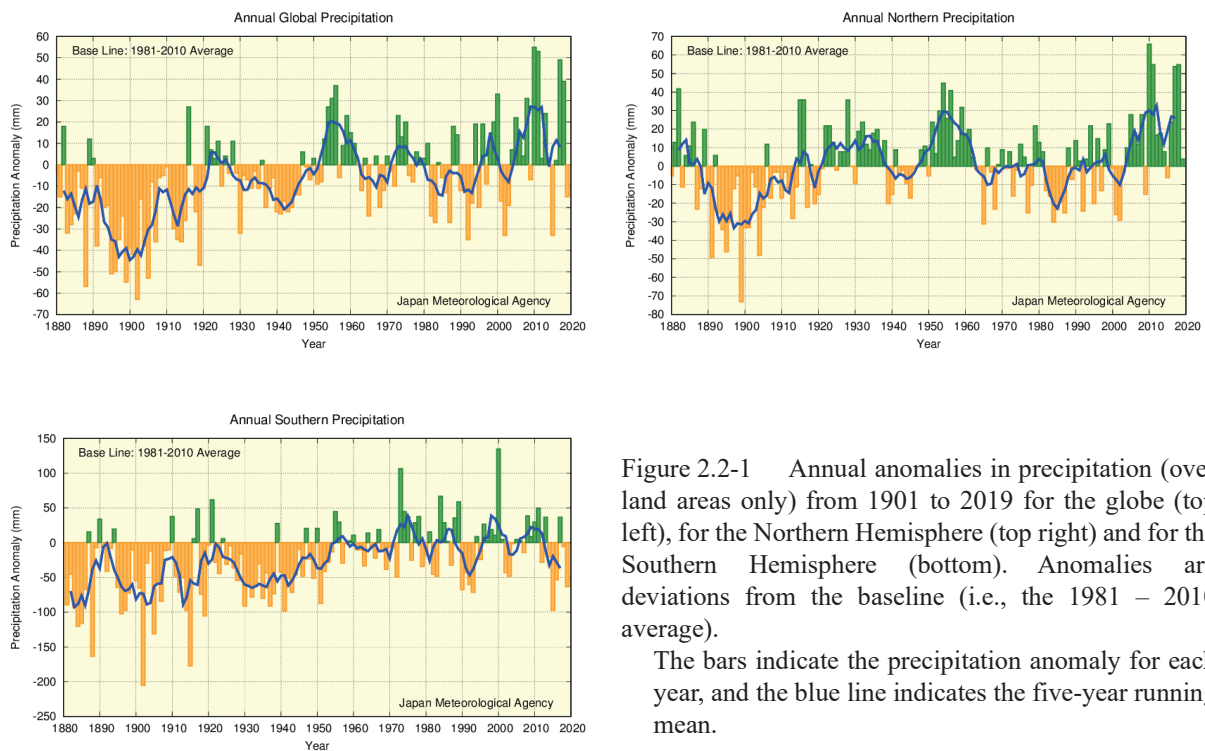


Figure 2.2-1 Annual anomalies in precipitation (over land areas only) from 1901 to 2019 for the globe (top left), for the Northern Hemisphere (top right) and for the Southern Hemisphere (bottom). Anomalies are deviations from the baseline (i.e., the 1981 – 2010 average).

The bars indicate the precipitation anomaly for each year, and the blue line indicates the five-year running mean.

### 2.2.2 Precipitation over Japan

This section describes long-term trends in precipitation over Japan as derived from analysis of precipitation records from 51 observation stations (Table 2.2-1).

Annual precipitation in 2019 was +35.5 mm above the 1981 – 2010 average. Japan experienced relatively large amounts of rainfall until the mid-1920s and around the 1950s. The annual figure exhibits greater variability for the period from the 1970s to the 2000s (Figure 2.2-2).

<sup>16</sup> Data on annual precipitation around the world and in Japan are published on JMA's website. <https://www.data.jma.go.jp/cpdinfo/temp/index.html> (Japanese)

Table 2.2-1 List of 51 observation stations whose data are used to calculate precipitation anomalies and long-term trends in Japan

Element	Observation stations
Precipitation (51 stations)	Asahikawa, Abashiri, Sapporo, Obihiro, Nemuro, Suttsu, Akita, Miyako, Yamagata, Ishinomaki, Fukushima, Fushiki, Nagano, Utsunomiya, Fukui, Takayama, Matsumoto, Maebashi, Kumagaya, Mito, Tsuruga, Gifu, Nagoya, Iida, Kofu, Tsu, Hamamatsu, Tokyo, Yokohama, Sakai, Hamada, Kyoto, Hikone, Shimonoseki, Kure, Kobe, Osaka, Wakayama, Fukuoka, Oita, Nagasaki, Kumamoto, Kagoshima, Miyazaki, Matsuyama, Tadotsu, Kochi, Tokushima, Naze, Ishigakijima, Naha

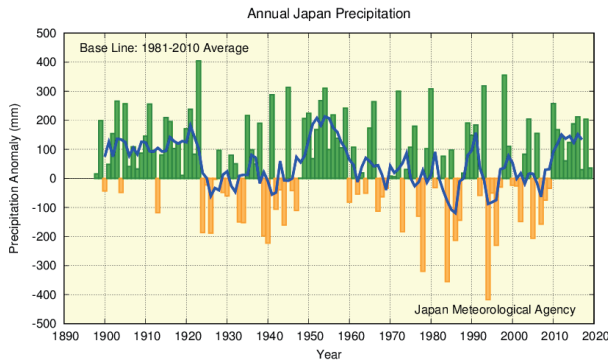


Figure 2.2-2 Annual anomalies in precipitation from 1898 to 2019 in Japan. Anomalies are deviations from the baseline (i.e., the 1981 – 2010 average).

The bars indicate the precipitation anomaly for each year, and the blue line indicates the five-year running mean.

### 2.2.3 Long-term trends of extreme precipitation events in Japan

This section describes long-term trends in frequencies of extremely wet/dry months and heavy daily precipitation events in Japan based on analysis of precipitation data from 51 observation stations.

#### (1) Extremely wet/dry months<sup>17</sup>

It is virtually certain that the frequency of extremely dry months increased during the period from 1901 to 2019 (statistically significant at a confidence level of 99%) (Figure 2.2-3 left). There has been no discernible trend in the frequency of extremely wet months (Figure 2.2-3 right).

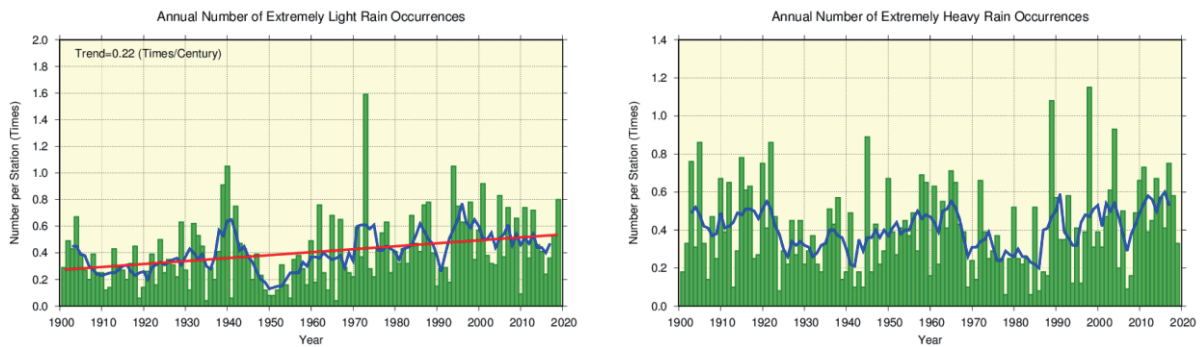


Figure 2.2-3 Annual number of extremely wet/dry months from 1901 to 2019

The graphs show the annual number of occurrences of the first-to-fourth heaviest/lightest precipitation values for each month during the period from 1901 to 2019. The green bars indicate annual occurrences of extremely heavy/light monthly precipitation divided by the total number of monthly observation data sets available for the year (i.e., the average occurrence per station). The blue line indicates the five-year running mean, and the straight red line indicates the long-term linear trend.

<sup>17</sup> Here, judgment of extremely heavy/light precipitation is based on the fourth-highest/lowest monthly values on record over the 119-year period from 1901 to 2019. The frequency of occurrence of the highest/lowest to the fourth-highest/lowest values over this period is once approximately every 30 years, which is close to JMA's definition of extreme climate events as those occurring once every 30 years or longer (See the Glossary for terms relating to Extreme climate event).

(2) Annual number of days with precipitation of  $\geq 100$  mm,  $\geq 200$  mm and  $\geq 1.0$  mm

The annual number of days with precipitation of  $\geq 100$  mm and  $\geq 200$  mm are virtually certain to have increased (both statistically significant at a confidence level of 99%) during the period from 1901 to 2019 (Figure 2.2-4). The annual number of days with precipitation of  $\geq 1.0$  mm (Figure 2.2-5) is virtually certain to have decreased over the same period (statistically significant at a confidence level of 99%). These results suggest decrease in the annual number of wet days including light precipitation and in contrast, an increase in extremely wet days.

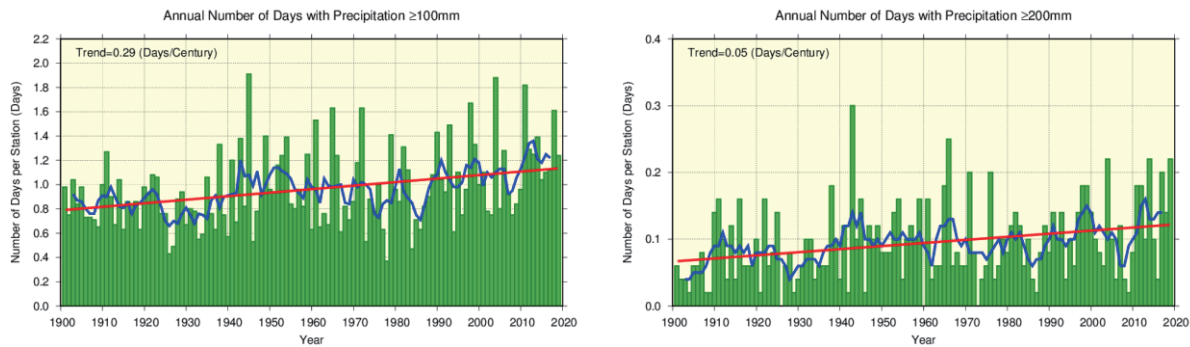


Figure 2.2-4 Annual number of days with precipitation  $\geq 100$  mm and  $\geq 200$  mm from 1901 to 2019

The green bars indicate the annual number of days per station for each year. The blue line indicates the five-year running mean, and the straight red line indicates the long-term linear trend.

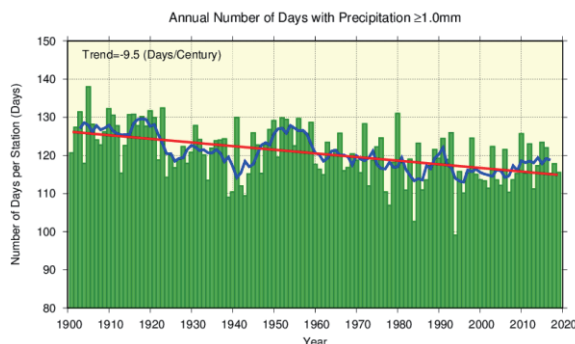


Figure 2.2-5 Annual number of days with precipitation of  $\geq 1.0$  mm from 1901 to 2019

As per figure 2.2-4.

#### 2.2.4 Long-term trends of heavy rainfall analyzed using AMeDAS data

JMA operationally observes precipitation at about 1,300 unmanned regional meteorological observation stations all over Japan (collectively known as the Automated Meteorological Data Acquisition System, or AMeDAS). Observation was started in the latter part of the 1970s at many points, and observation data covering the approximately 40-year period through to 2019 are available<sup>18</sup>. Although the period covered by AMeDAS observation records is shorter than that of Local Meteorological Observatories or Weather Stations (which have observation records for the past 100 years or so), there are around eight times as many AMeDAS stations as Local Meteorological Observatories and Weather Stations combined. Hence, AMeDAS is better equipped to capture heavy precipitation events that take place on a limited spatial scale.

It is virtually certain that the annual numbers of events with precipitation of  $\geq 50$  mm and

<sup>18</sup> The number of AMeDAS station was about 800 in 1976, and had gradually increased to about 1,300 in 2019. To account for these numerical differences, the annual number of precipitation events needs to be converted to a per-1,300-station basis. Data from wireless robot precipitation observation stations previously deployed in mountainous areas are also excluded.

$\geq 80$  mm per hour have increased (both statistically significant at a confidence level of 99%) (Figure 2.2-6). For the annual number of days with precipitation of  $\geq 50$  mm per hour, the number averaged for the last 10 years of the records (2010 – 2019) is about 327 on a per-1,300-station basis, which is about 1.4 times as many as that averaged for the first 10 years (1976 – 1985) of about 226.

The annual number of days with precipitation of  $\geq 200$  mm is very likely to have increased (statistically significant at a confidence level of 90%), and the corresponding figure for days with precipitation of  $\geq 400$  mm is extremely likely to have increased (statistically significant at a confidence level of 95%) (Figure 2.2-7).

As the annual number of extreme precipitation events is subject to large annual variations and the period covered by observation records is still relatively short, the addition of future observations to the data series is expected to increase the reliability of statistical trend detection.

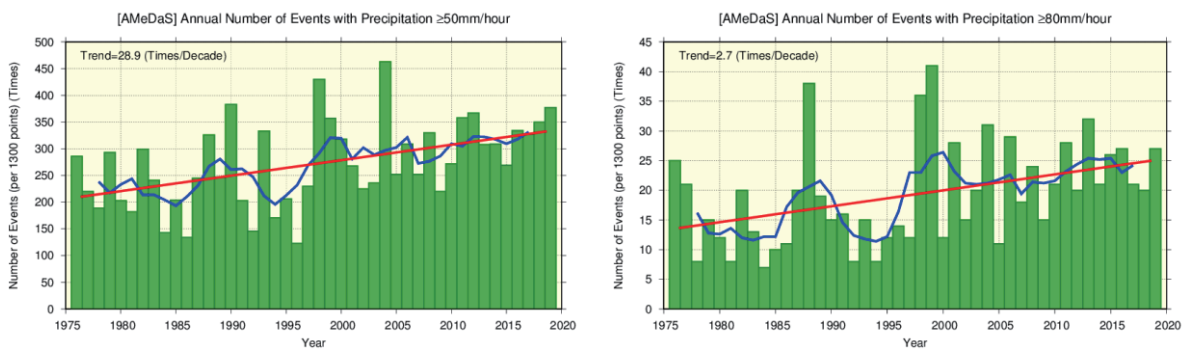


Figure 2.2-6 Annual number of events with precipitation of  $\geq 50$  mm and  $\geq 80$  mm per hour from 1976 to 2019. The green bars indicate the annual number of events per 1,300 AMeDAS stations for each year, and the straight red line indicates the long-term linear trend.

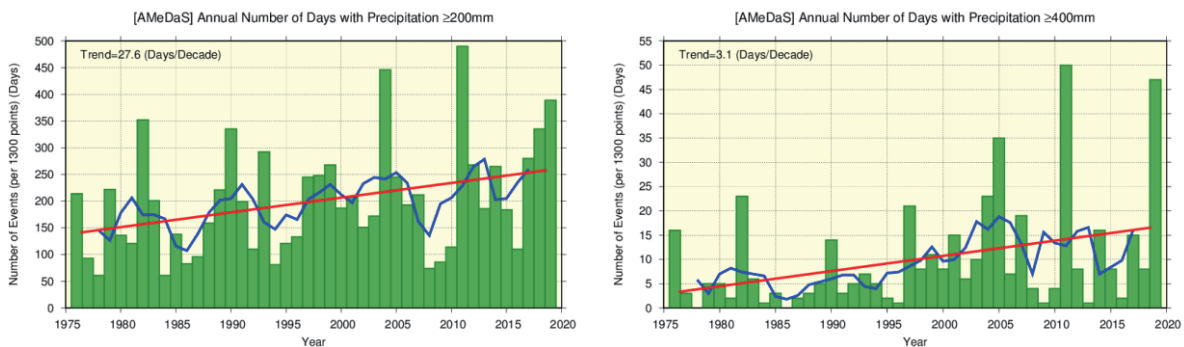


Figure 2.2-7 Annual number of days with precipitation of  $\geq 200$  mm and  $\geq 400$  mm from 1976 to 2019. The green bars indicate the annual number of days per 1,300 AMeDAS stations for each year, and the straight red line indicates the long-term linear trend.

### 2.2.5 Snow depth in Japan

Long-term trends in the annual maximum snow depth (represented in terms of a ratio against the 1981 – 2010 average) in Japan since 1962 are analyzed using observational records from stations located on the Sea of Japan coast (Table 2.2-2).

Table 2.2-2 Observation stations whose data are used to calculate snow depth ratios in Japan

Region	Observation stations
Sea of Japan side of northern Japan	Wakkanai, Rumoi, Asahikawa, Sapporo, Iwamizawa, Suttsu, Esashi, Kutchan, Wakamatsu, Aomori, Akita, Yamagata
Sea of Japan side of eastern Japan	Wajima, Aikawa, Niigata, Toyama, Takada, Fukui, Tsuruga
Sea of Japan side of western Japan	Saigo, Matsue, Yonago, Tottori, Toyooka, Hikone, Shimonoseki, Fukuoka, Oita, Nagasaki, Kumamoto

The annual maximum snow depth ratio in 2019 was 79% relative to the 1981 – 2010 average for the Sea of Japan side of northern Japan, 36% for the same side of eastern Japan, and 13% for the same side of western Japan (Figure 2.2-8). On a longer time scale, the annual maximum snow depth ratio from 1962 onward on the Sea of Japan side of northern Japan is very likely to have decreased at rates of 3.2% per decade (statistically significant at a confidence level of 90%), that on the Sea of Japan side of eastern Japan is extremely likely to have decreased at rates of 11.4% per decade (statistically significant at a confidence level of 95%), and that on the Sea of Japan side of western Japan is extremely likely to have decreased at rates of about 13.5% per decade (statistically significant at a confidence level of 95%). The annual maximum snow depth reached a local peak in the early 1980s followed by a sharp decline until around the early 1990s. The decline was particularly striking on the Sea of Japan side of eastern and western Japan.

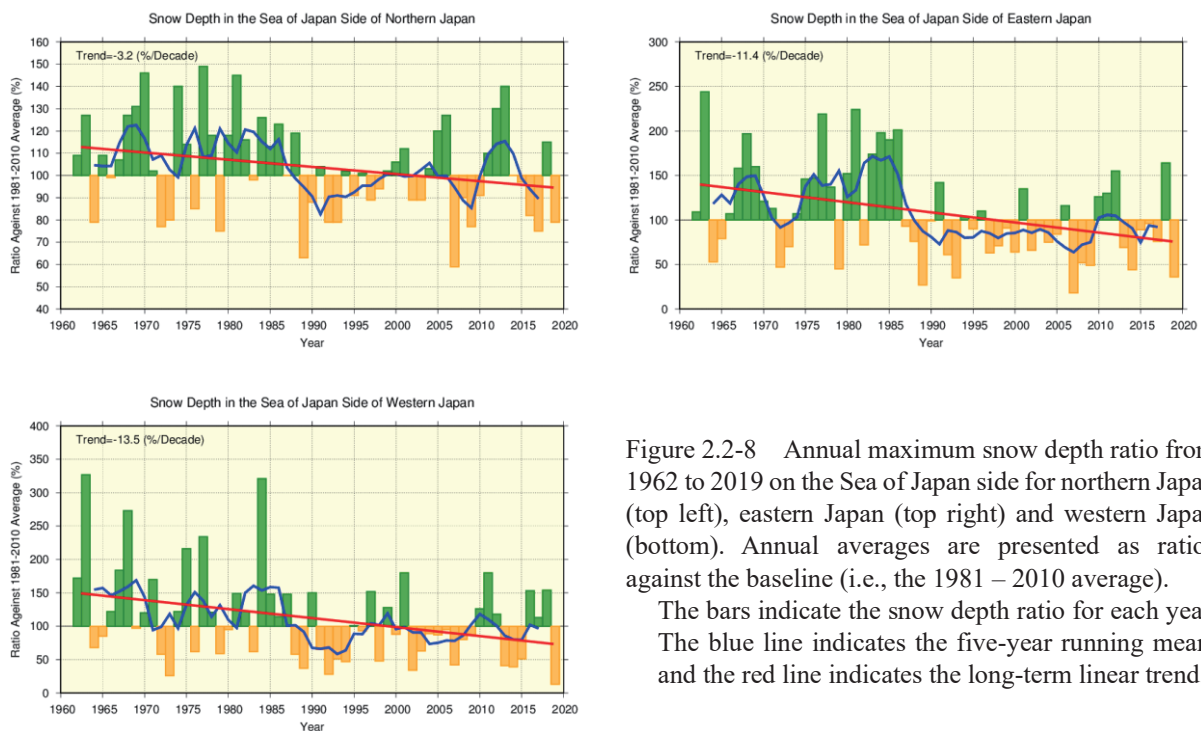


Figure 2.2-8 Annual maximum snow depth ratio from 1962 to 2019 on the Sea of Japan side for northern Japan (top left), eastern Japan (top right) and western Japan (bottom). Annual averages are presented as ratios against the baseline (i.e., the 1981 – 2010 average).

The bars indicate the snow depth ratio for each year. The blue line indicates the five-year running mean, and the red line indicates the long-term linear trend.

## 2.3 Changes in the phenology of cherry blossoms and acer leaves in Japan

- It is virtually certain that cherry blossoms have been flowering earlier.
- It is virtually certain that acer leaves have been changing color later.

JMA implements phenological observation to research the impact of meteorological condition on plants and animals, and eventually to monitor the progress of seasons as well as geographical variations and long-term changes in relation to the climate. Observation covers the first/full flowering and leaf color change of several plants and the first reported appearance/song of insects, birds and animals.

As part of its phenological monitoring, JMA observes cherry blossoms at 58 stations and acer leaves at 51 stations. Figure 2.3-1 shows interannual changes in the first reported dates of cherry blossom flowering and acer leaf color change between 1953 and 2019. The former exhibits a long-term advancing trend at a rate of 1.0 days per decade, while the latter shows a delaying trend at a rate of 2.8 days per decade (99% level of confidence for both cases). Table 2.3-1 compares climatological normals (based on 30-year averages) of the first reported date of cherry blossom flowering between 1961 – 1990 and 1981 – 2010 at stations in major Japanese cities. These phenomena are closely related to the surface mean temperature in the period before the event, and long-term warming is considered to be a major factor behind the trends observed.

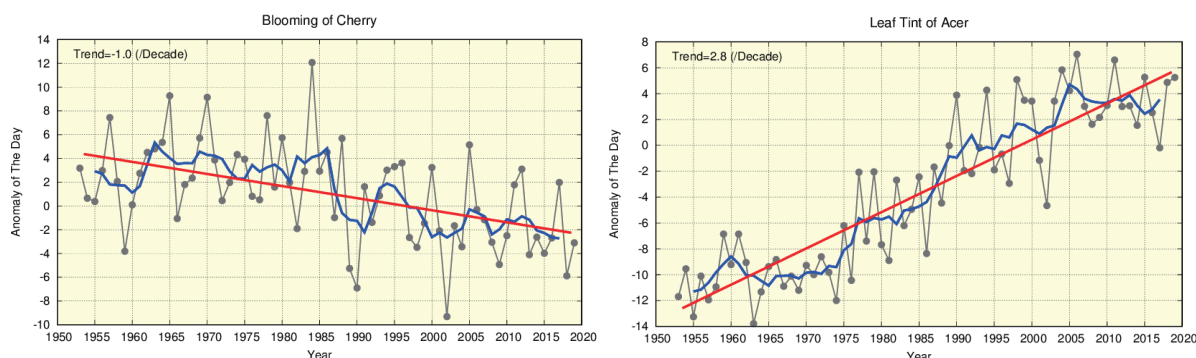


Figure 2.3-1 First reported dates of cherry blossom flowering (left) and acer leaf color change (right)  
 The black lines show annual anomalies of the first reported date averaged over all observation stations nationwide based on the normals for 1981 – 2010, and the blue lines indicate five-year running means. The red lines show the linear trend (cherry blossoms:  $-1.0$  days per decade; acer leaves:  $+2.8$  days per decade).

Table 2.3-1 Comparison of first reported dates of cherry blossom flowering  
 Differences in climatological normals for the first reported date of cherry blossom flowering between 1981 – 2010 and 1961 – 1990 at stations in major Japanese cities

Station	1961-1990 average	1981-2010 average	Difference (days)		1961-1990 average	1981-2010 average	Difference (days)
Kushiro	May 19	May 17	-2	Osaka	Apr 1	Mar 28	-4
Sapporo	May 5	May 3	-2	Hiroshima	Mar 31	Mar 27	-4
Aomori	Apr 27	Apr 24	-3	Takamatsu	Mar 31	Mar 28	-3
Sendai	Apr 14	Apr 11	-3	Fukuoka	Mar 28	Mar 23	-5
Niigata	Apr 13	Apr 9	-4	Kagoshima	Mar 27	Mar 26	-1
Tokyo	Mar 29	Mar 26	-3	Naha	Jan 16	Jan 18	+2
Nagoya	Mar 30	Mar 26	-4	Ishigakijima	Jan 15	Jan 16	+1

## 2.4 Tropical cyclones over the western North Pacific and the South China Sea

- A total of 29 tropical cyclones (TCs) with maximum wind speeds of 34 kt<sup>19</sup> or higher formed over the western North Pacific and the South China Sea in 2019, which was above normal.
- The numbers of formations show no significant long-term trend.

In 2019, 29 tropical cyclones (TCs) with maximum wind speeds of  $\geq 34$  kt formed over the western North Pacific and the South China Sea (Figure 2.4-1), which was above the normal (i.e., the 1981 – 2010 average) of 25.6. The numbers of formations show no discernible long-term trend during the analysis period from 1951 to 2019, while they have often been below the normal from the latter half of the 1990s to the early 2010s. Numbers of TCs with maximum wind speeds of  $\geq 34$  kt approaching and making landfall in Japan were 15 and 5 (Figure 2.4-2), both of which were above the normal of 11.4 and 2.7, respectively. The numbers of TCs approaching Japan also show no discernible long-term trend during the same period from 1951 to 2019.

Figure 2.4-3 shows the numbers and rates of strong TCs with maximum wind speeds of  $\geq 64$  kt to those with maximum wind speeds of  $\geq 34$  kt from 1977 (the year in which the collection of complete data on maximum wind speeds near TC centers began). The numbers of strong TCs show no discernible trend during the period from 1977 to 2019.

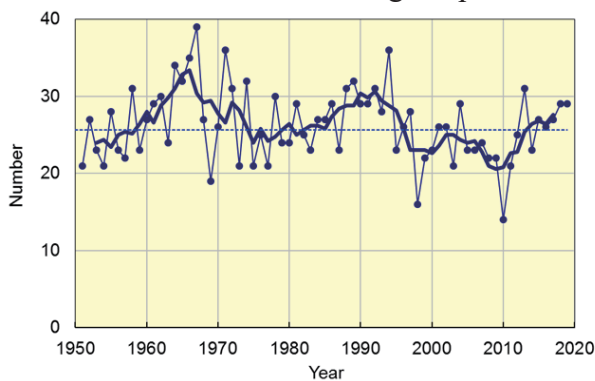


Figure 2.4-1 Time-series of the numbers of TCs with maximum wind speeds of  $\geq 34$  kt forming in the western North Pacific and the South China Sea from 1951 to 2019.

The thin and thick lines represent annual and five-year running means, respectively.

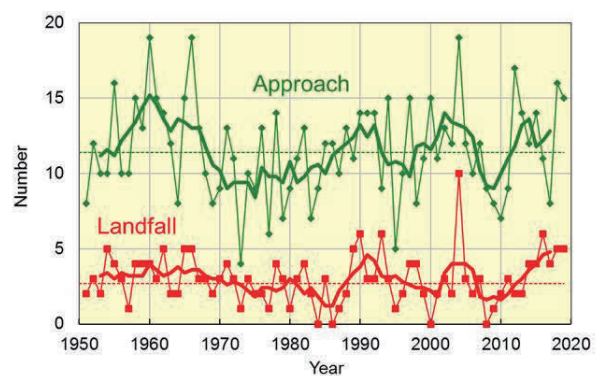


Figure 2.4-2 Time-series of the numbers of TCs with maximum wind speeds of  $\geq 34$  kt approaching (green) and making landfall in Japan (red) from 1951 to 2019.

The thin and thick lines represent annual and five-year running means, respectively.

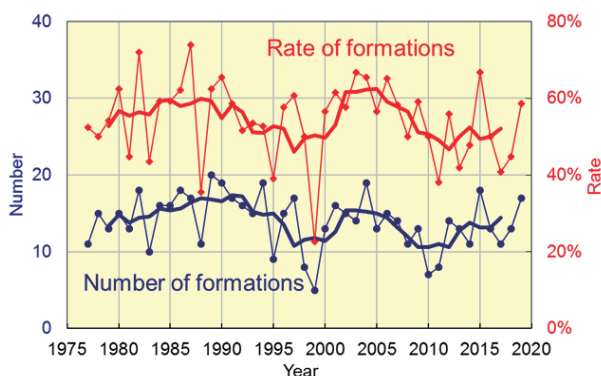


Figure 2.4-3 Time-series of the numbers of strong TCs with maximum wind speeds of  $\geq 64$  kt (blue) and rates of the strong TCs to the total TCs with maximum wind speeds of  $\geq 34$  kt (red) forming in the western North Pacific and the South China Sea from 1977 to 2019.

The thin and thick lines represent annual and five-year running means, respectively.

<sup>19</sup> One knot (kt) is about 0.51 m/s

## 2.5 Sea surface temperature<sup>20</sup>

- The annual mean global average sea surface temperature (SST) in 2018 was 0.22°C above the 1981 – 2010 average, which was the fourth highest since 1891 (highest: 2016; second highest: 2015; third highest: 2017).
- The global average SST has risen at a rate of about +0.54°C per century.
- Annual average SSTs around Japan have risen by +1.14°C per century.

### 2.5.1 Global sea surface temperature

The annual mean global average SST in 2018 was 0.22°C above the 1981 – 2010 average. This was the fourth highest since 1891 (highest: 2016; second highest: 2015; third highest: 2017). The years from 2014 to 2018 represent the top-five five warmest since 1891.

The linear trend from 1891 to 2018 shows an increase of +0.54°C per century (Figure 2.5-1). Although magnitudes of the long-term SST trend vary by area, it is extremely likely that SSTs have increased in many parts of the world's oceans (Figure 2.5-2). Global average SSTs and global average surface temperatures (Section 2.1) are affected by natural climate variability on inter-annual to inter-decadal time scales as well as by global warming.

On a multi-year time scale, global average SSTs showed a rising trend from the middle of the 1970s to around 2000, before remaining largely static until the early 2010s and thereafter re-assuming an upward trend (Figure 2.5-1, blue line). This is partly because rising trends overlap with decadal-to-multi-decadal variations in the climate system. It is important to estimate the contribution of these internally induced natural variations in order to properly understand global warming. In the next section, the Pacific Decadal Oscillation (PDO) is presented as a typical example of decadal variability observed in SSTs.

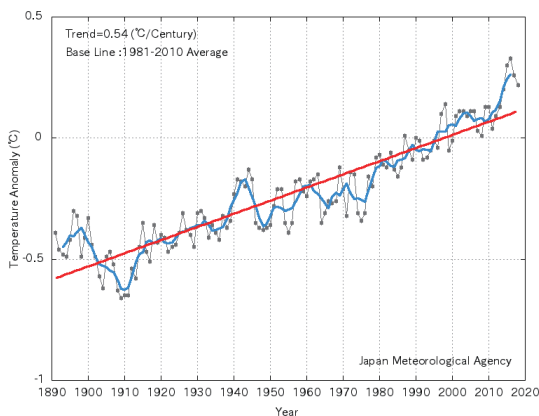


Figure 2.5-1 Time-series representation of global average sea surface temperature anomalies from 1891 to 2018

The black, blue and red lines indicate annual anomalies, the five-year running mean and the long-term linear trend, respectively. Anomalies are deviations from the 1981 – 2010 average.

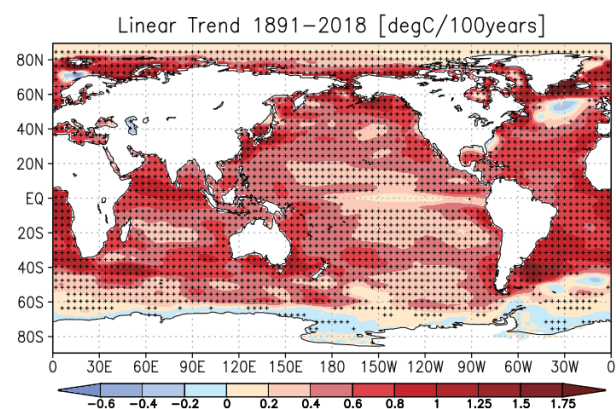


Figure 2.5-2 Linear trend of annual mean sea surface temperature during the period from 1891 to 2018 (°C per century)

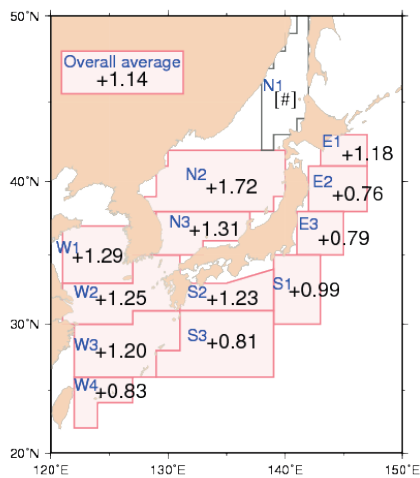
Plus signs indicate statistically significant trends with a confidence level of 95%.

<sup>20</sup> The results of analysis regarding tendencies of SSTs worldwide and around Japan are published on JMA's website. [https://www.data.jma.go.jp/gmd/kaiyou/english/long\\_term\\_sst\\_global/glb\\_warm\\_e.html](https://www.data.jma.go.jp/gmd/kaiyou/english/long_term_sst_global/glb_warm_e.html)  
[https://www.data.jma.go.jp/gmd/kaiyou/english/long\\_term\\_sst\\_japan/sea\\_surface\\_temperature\\_around\\_japan.html](https://www.data.jma.go.jp/gmd/kaiyou/english/long_term_sst_japan/sea_surface_temperature_around_japan.html)

### 2.5.2 Sea surface temperature (around Japan)

Figure 2.5-3 shows increase rates of area-averaged annual mean SSTs for 13 areas around Japan. The average SST of all areas around Japan has risen by  $+1.14^{\circ}\text{C}$  per century, which is higher than the corresponding value for the North Pacific ( $+0.53^{\circ}\text{C}$  per century).

It is virtually certain (statistically significant at a confidence level of 99%) that SSTs have risen by between  $+0.76$  and  $+1.72^{\circ}\text{C}$  per century in the sea off Kushiro, the sea off Sanriku, eastern and southern parts of the sea off Kanto, the sea off Shikoku and Tokai, east of Okinawa, the central and southwestern parts of the Sea of Japan, the Yellow Sea, the East China Sea, and the sea around the Sakishima Islands (areas E1-3, S1-3, N2-3, and W1-4). SSTs in the northeastern part of the Sea of Japan (area N1) exhibit no statistical long-term trend.



Area number	Area name
E1	Sea off Kushiro
E2	Sea off Sanriku
E3	Eastern part of the sea off Kanto
S1	Southern part of the sea off Kanto
S2	Sea off Shikoku and Tokai
S3	East of Okinawa
N1	Northeastern part of the Sea of Japan
N2	Central part of the Sea of Japan
N3	Southwestern part of the Sea of Japan
W1	Yellow Sea
W2	Northern part of the East China Sea
W3	Southern part of the East China Sea
W4	Sea around the Sakishima Islands

Figure 2.5-3 Increase rates of area-averaged annual mean SSTs around Japan from 1900 to 2019 ( $^{\circ}\text{C}$  per century) Areas with no symbol have statistical significant trend at confidence levels of 99%. Areas marked with [#] are those where no discernible trend is seen due to large SST variability factors such as decadal oscillation.

## 2.6 El Niño/La Niña <sup>21</sup> and PDO (Pacific Decadal Oscillation) <sup>22</sup>

- The El Niño event that started in autumn 2018 continued until spring 2019. The ENSO-neutral conditions, in which neither El Niño event nor La Niña event have prevailed, have been observed in the equatorial Pacific since summer 2019.
- Negative PDO index values were generally observed from around 2000 to the early 2010s. Thereafter, the annual mean values have been consecutively positive since 2014.

### 2.6.1 El Niño/La Niña

An El Niño event is a phenomenon in which sea surface temperatures (SSTs) are above normal over the equatorial Pacific from near the date line to the coast of South America for around a year. In contrast, a La Niña event is a phenomenon in which SSTs are below normal over the same area. Both events occur every few years, causing changes in global atmospheric circulations which result in abnormal weather conditions worldwide. In Japan, cooler summers and warmer winters tend to appear during El Niño events, while hotter summers and colder winters tend to appear during La Niña events.

Figure 2.6-1 shows a time-series representation of SST deviations from climatological means based on a sliding 30-year period for the El Niño monitoring region (5°N – 5°S, 150°W – 90°W) and SST deviations from reference values based on linear extrapolation with respect to the latest sliding 30-year period for the tropical western Pacific region (Eq. – 15°N, 130 – 150°E) since 2009. SSTs in the El Niño monitoring region were above the relevant climatological means from January to May 2019 and have remained near these values since June 2019. SSTs in the Western Pacific region were below the related reference values from January to April of 2019, and have been near or below these levels since May 2019. These variations are consistent with the continuation of the El Niño event from autumn 2018 to spring 2019 and the presence of ENSO-neutral conditions since summer 2019.

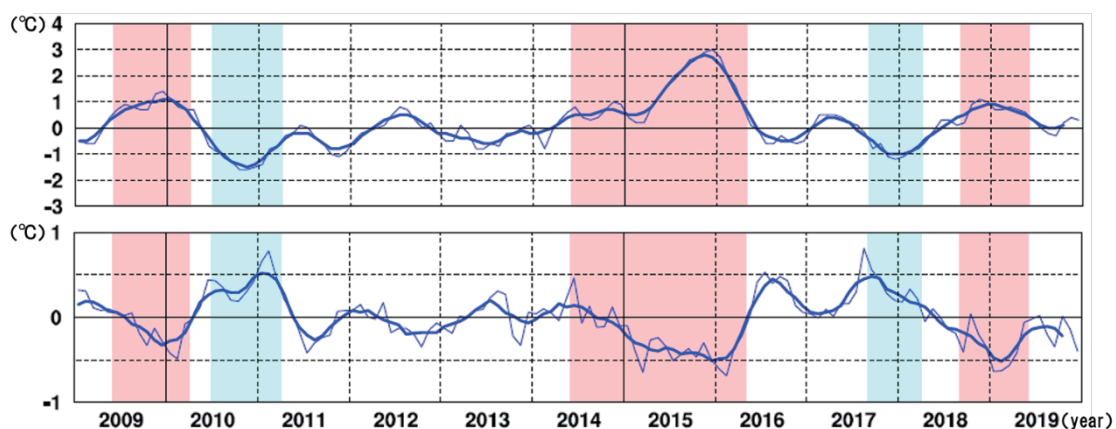


Figure 2.6-1 Time-series representations of SST deviations from the climatological mean based on a sliding 30-year period for the El Niño monitoring region (top) and SST deviations from reference values based on linear extrapolation with respect to the latest sliding 30-year period for the Western Pacific (bottom)

Thin lines indicate monthly means, and smooth thick curves indicate the five-month running mean.

Red shading denotes El Niño periods, and blue shading denotes La Niña periods.

<sup>21</sup> See the Glossary for terms relating to El Niño phenomena. Monthly diagnosis reports, ENSO monitoring products, ENSO indices and El Niño outlooks are published on JMA's website.

<https://ds.data.jma.go.jp/tcc/tcc/products/elnino/index.html>

<sup>22</sup> The PDO index time series is published on JMA's website.

<https://ds.data.jma.go.jp/tcc/tcc/products/elnino/decadal/pdo.html>

### 2.6.2 Pacific Decadal Oscillation

SST variability is also observed on time scales ranging from one to several decades in addition to El Niño/La Niña events, whose time scale is several years, and long-term trends associated with global warming. Among these, the atmosphere and oceans tend to co-vary with a period of more than ten years in the North Pacific in a phenomenon known as the Pacific Decadal Oscillation (PDO). When SSTs are lower (higher) than their normals in the central part of the North Pacific, those in its part along the coast of North America are likely to be higher (lower) than their normals. This seesaw pattern changes slowly, and appears repeatedly with a period of more than ten years. The PDO index, which is defined by the SST anomaly pattern in the North Pacific, is used as a measure of phase and strength of the oscillation. It is noted that both the PDO index and SST anomaly patterns associated with PDO include relatively short-timescale variabilities such as El Niño/La Niña events in addition to decadal to multi-decadal components.

When the PDO index is positive (negative), SSTs in the central part of the North Pacific are likely to be lower (higher) than their normals in addition to those along the coast of North America, and those in the equatorial part from near the date line to the coast of South America are likely to be higher (lower) than normal. This tendency is analogous to the patterns observed in El Niño (La Niña) events (Figure 2.6-2). Additionally, sea level pressures (SLPs) in the high latitudes of the North Pacific are likely to be lower (higher) than their normals in the same time (Figure 2.6-3). This indicates that the Aleutian Low is stronger (weaker) than its normal in winter and spring. These atmospheric variations affect meteorological conditions mainly in North America. When the PDO index is positive, winter temperatures tend to be high in the northwestern part of North America and the northern part of South America, and low in the southeastern part of the USA and in parts of China (Mantua and Hare, 2002).

The PDO index was generally positive from the late 1920s to the early 1940s and from the late 1970s to around 2000, and was generally negative from the late 1940s to the mid-1970s and from around 2000 to the early 2010s. The annual mean PDO index value has remained positive since 2014 (Figure 2.6-4).

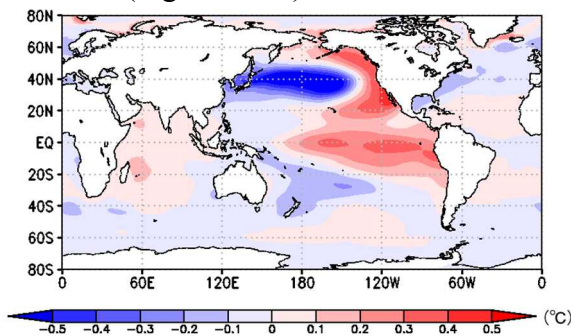


Figure 2.6-2 Typical SST anomaly patterns in the positive phase of the PDO

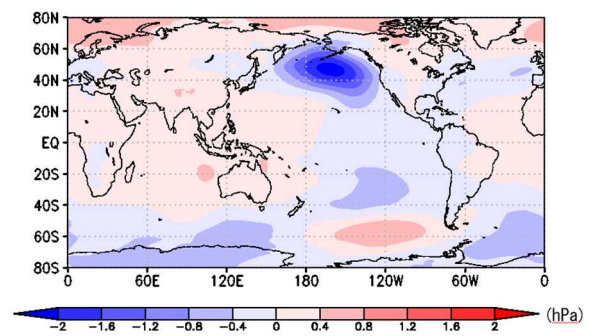


Figure 2.6-3 Typical SLP anomaly patterns in the positive phase of the PDO

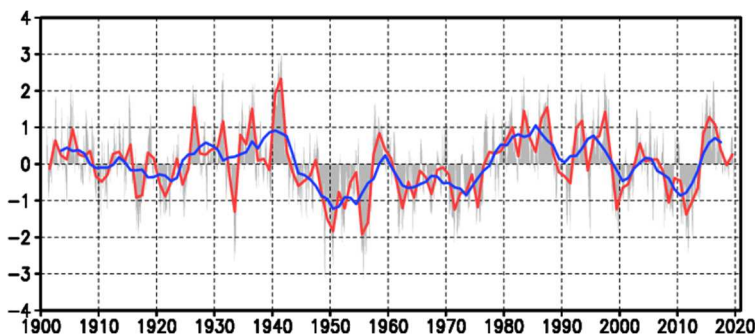


Figure 2.6-4 Time-series of the PDO index

The red line represents annual mean values for the PDO index, the blue line represents five-year running mean values, and the gray bars represent monthly values.

## 2.7 Global ocean heat content<sup>23</sup>

- Globally integrated ocean heat content (OHC) exhibits a long-term increase.
- OHC has exhibited a higher rate of increase since the mid-1990s.

Oceans have a significant impact on the global climate because they cover about 70% of the earth's surface and have high heat capacity. The Intergovernmental Panel on Climate Change Special Report on the Ocean and Cryosphere in a Changing Climate (IPCC, 2019) said that approximately 90% of heat energy in the earth's system was present in oceans, and that approximately 90% of this ocean heat was in the top 2,000 m (Johnson et al., 2019).

It is virtually certain that globally integrated ocean heat content (OHC) from 0 to 2,000 m exhibits a long-term increase (statistically significant at a confidence level of 99%) (Figure 2.7-1). OHC had risen by approximately  $43 \times 10^{22}$  J in 2019 relative to 1955. Since the mid-1990s, the rate of increase ( $9.7 \times 10^{22}$  J per decade for 1993 – 2019) has risen ( $3.9 \times 10^{22}$  J per decade for 1955 – 1993). IPCC (2019) also reported an accelerated increase of ocean heat uptake.

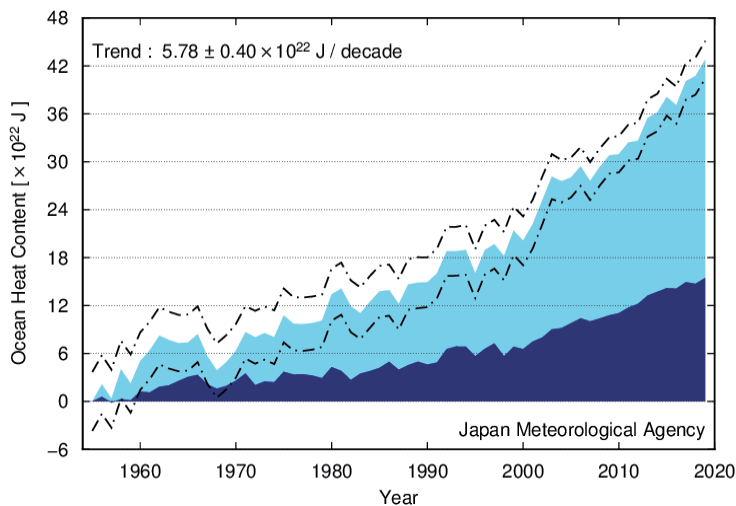


Figure 2.7-1 Time-series representation of globally integrated ocean heat content relative to 1955

The light- and dark-blue areas show annual means for global integrals of 0 to 700 m and 700 to 2,000 m, respectively, for ocean heat content relative to 1955. The dot-dash lines indicate a 95% confidence level for ocean heat content above 2,000 m.

<sup>23</sup> The results of ocean heat content analysis are published on JMA's website. [https://www.data.jma.go.jp/gmd/kaiyou/english/ohc/ohc\\_global\\_en.html](https://www.data.jma.go.jp/gmd/kaiyou/english/ohc/ohc_global_en.html)

## 2.8 Sea levels around Japan <sup>24</sup>

- A trend of sea level rise has been seen in Japanese coastal areas since the 1980s.
- No long-term trend of sea level rise is seen in Japanese coastal areas for the period from 1906 to 2019.

The IPCC Special Report on the Ocean and Cryosphere in a Changing Climate 2019 (SROCC) concluded that the global mean sea level (GMSL) is rising, with acceleration in recent decades due to increasing rates of ice loss from the Greenland and Antarctic ice sheets (very high confidence), as well as continued glacier mass loss and ocean thermal expansion. The report also identified a total GMSL rise for the period from 1902 to 2010 of 0.16 [0.12 to 0.21] m and a GMSL rate for 2006 to 2015 of 3.6 [3.1 to 4.1] mm/year, representing unprecedented levels for the last century (high confidence), and approximately 2.5 times the rate for 1901 to 1990 of 1.4 [0.8 to 2.0] mm/year (values in square brackets show the 95% uncertainty range).

Sea levels in Japanese coastal areas exhibit no significant rise from 1906 to 2019 (Figure 2.8-1), but have shown a rising trend since the 1980s. Recent rates of rise around the country have been 4.1 [0.1 to 8.2] mm/year from 2006 to 2015. These figures are comparable to those observed for the global average in recent years.

In Japanese coastal areas, variations with 10- to 20-year periods are seen between 1906 and 2019. The major factor behind sea level variations with 10- to 20-year periods is the variability of atmospheric circulation over the North Pacific. Westerlies in the mid-latitudes of the Northern Hemisphere are strengthened in boreal winter, and the consequent decadal variations in turn cause sea level variations in the central North Pacific. These propagate westward due to the earth's rotation, causing sea level rise around Japan.

The extent to which global warming has contributed to sea level change around Japan remains unclear due to the involvement of various other factors such as variations with 10- to 20-year periods as mentioned above. Continuous monitoring is needed to clarify the long-term trend of sea level rise caused by global warming.

---

<sup>24</sup> Sea levels around Japan are published on the JMA's website.  
[https://www.data.jma.go.jp/gmd/kaiyou/english/sl\\_trend/sea\\_level\\_around\\_japan.html](https://www.data.jma.go.jp/gmd/kaiyou/english/sl_trend/sea_level_around_japan.html)

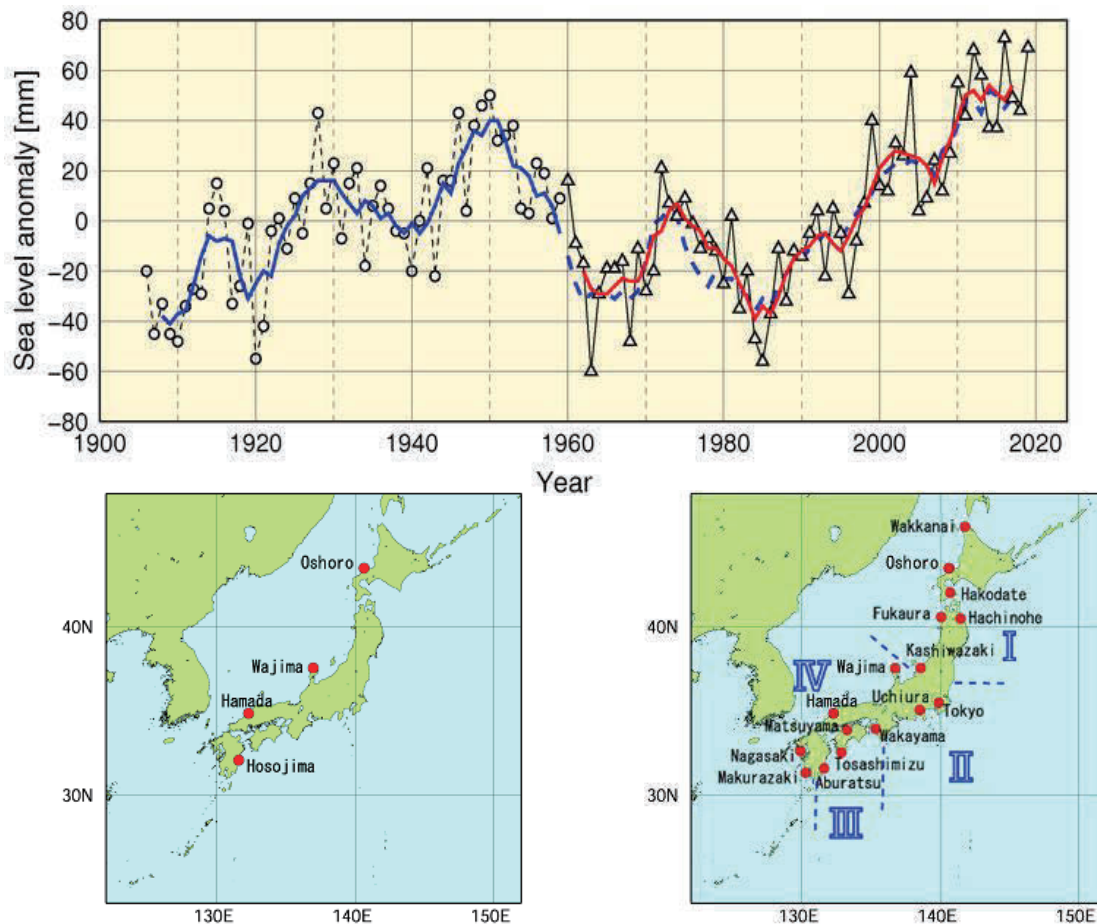


Figure 2.8-1 Time-series representation of annual mean sea levels (1906 – 2019) and locations of tide gauge stations

Tide gauge stations assessed as being affected to a lesser extent by crustal movement are selected. The four stations shown on the map on the left are used for the period from 1906 to 1959, and the sixteen shown on the right are used for the period since 1960. From 1906 to 1959, a time-series representation of mean annual mean sea level anomalies for the selected stations is shown. For the period since 1960, the nation's islands were then divided into four regions based on sea level variation characteristics, annual mean sea level anomalies were averaged for each of the regions, and the variations were plotted in the figure. The four regions are I: from Hokkaido to Tohoku district; II: from Kanto to Tokai district; III: from the Pacific coast of Kinki to that of Kyushu district; and IV: from Hokuriku to East China Sea coast of Kyushu district. Sea level variations are plotted on the chart as a time-series representation of annual mean sea level anomalies for each year, obtained using the 1981 to 2010 average as the normal. The solid blue line represents the five-year running mean of annual sea level anomalies averaged among the four stations shown in the lower left map, while the solid red line represents that averaged among the four divided regions in the lower right map. The dashed blue line represents the value averaged among the four stations shown in the lower left map for the same period shown by the solid red line (after 1960) for reference. The coefficient of correlation between the solid red line and the dashed blue line from 1962 to 2017 is as high as 0.98. Accordingly, the extent to which changing the tide gauge stations used in the monitoring affects the analysis of variance of sea level anomalies can be regarded as small. Among the tide gauge stations, those at Oshoro, Kashiwazaki, Wajima and Hosojima belong to the Geospatial Information Authority of Japan. Sea level data for the Tokyo station are available from 1968 onward. Sea level data for the period from 2011 to 2019 from Hakodate, Fukaura, Kashiwazaki, Tokyo and Hachinohe were not used due to possible influences from the 2011 off the Pacific coast of Tohoku Earthquake.

## 2.9 Sea ice<sup>25</sup>

- The sea ice extent in the Arctic Ocean is decreasing. In 2019, the annual minimum sea ice extent in the Arctic Ocean was  $4.18 \times 10^6 \text{ km}^2$ , which was the third-lowest value since 1979.
- The annual maximum sea ice extent in the Antarctic Ocean is extremely likely to increase. Since 2016, however, the sea ice extent has been lower than the normal.
- The maximum sea ice extent in the Sea of Okhotsk shows a decreasing trend of  $0.062 \times 10^6 \text{ km}^2$  per decade.

### 2.9.1 Sea ice in Arctic and Antarctic areas (Figures 2.9-1, 2.9-2, 2.9-3)

Sea ice is formed when sea water in the Arctic and Antarctic freezes. As the albedo (reflection coefficient) of sea ice is greater than that of the ocean surface, sea ice extent reductions caused by global warming result in more solar energy absorption at the surface, which in turn accelerates global warming. Sea ice also affects deep-ocean circulation because the expelled salt as it forms increases the salinity (and therefore the density) of the water below it causing the water to sink.

It is virtually certain that there has been a long-term trend of decrease in sea ice extent in the Arctic Ocean since 1979 when continuous monitoring of sea ice using satellite sensors with similar properties started (statistically significant at a confidence level of 99%). In particular, the reduction in the annual minimum extent is notable. The rate of decrease in the annual minimum up to 2019 was  $0.089 \times 10^6 \text{ km}^2$  per year. Meanwhile, it is extremely likely that there has been a long-term trend of increase in sea ice extent at a rate of  $0.016 \times 10^6 \text{ km}^2$  per year in the annual maximum sea ice extent in the Antarctic Ocean (statistically significant at the confidence level of 95%). However, the values since 2016 have been lower than the normal (Figure 2.9-1).

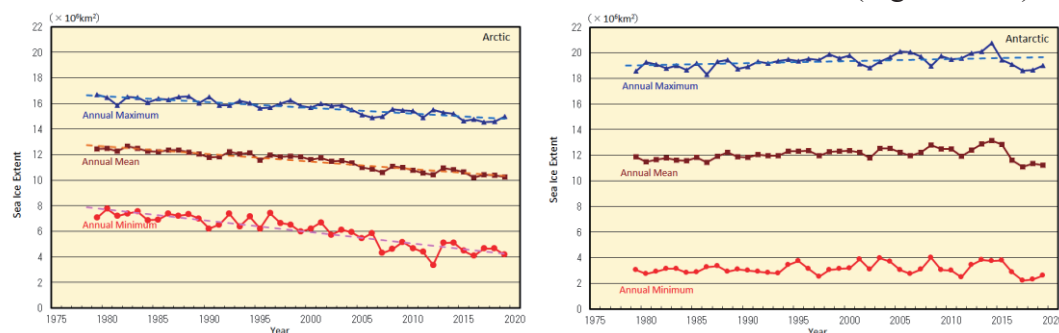


Figure 2.9-1 Time-series representations of annual maximum, annual mean and annual minimum sea ice extent in the Arctic Ocean (including the Sea of Okhotsk and the Bering Sea) (left) and in the Antarctic Ocean (right) from 1979 to 2019

The solid blue, brown and red lines indicate the annual maximum, the annual mean and the annual minimum sea ice extent, respectively. The dashed lines indicate the linear trends. Sea ice extents are calculated from brightness temperature data provided by NASA (the National Aeronautics and Space Administration) and NSIDC (the National Snow and Ice Data Center).

In 2019, the annual maximum Arctic sea ice extent was  $14.96 \times 10^6 \text{ km}^2$  on March 11, marking the seventh-lowest value since 1979. The extent subsequently decreased during spring and summer in the Northern Hemisphere and reached its annual minimum of  $4.18 \times 10^6 \text{ km}^2$  on September 13, marking the third-lowest value since 1979. Meanwhile, the Antarctic sea ice extent

<sup>25</sup> Information on sea ice in the Arctic/Antarctic, and in the Sea of Okhotsk are published on JMA's website.  
[https://www.data.jma.go.jp/gmd/kaiyou/english/seaice\\_global/series\\_global\\_e.html](https://www.data.jma.go.jp/gmd/kaiyou/english/seaice_global/series_global_e.html) (Arctic/Antarctic)  
[https://www.data.jma.go.jp/gmd/kaiyou/english/seaice\\_okhotsk/series\\_okhotsk\\_e.html](https://www.data.jma.go.jp/gmd/kaiyou/english/seaice_okhotsk/series_okhotsk_e.html) (Sea of Okhotsk)

was at its annual minimum of  $2.60 \times 10^6 \text{ km}^2$  on February 24, also marking the fifth-lowest value since 1979. The extent subsequently increased during the autumn and winter months of the Southern Hemisphere and reached its annual maximum of  $19.00 \times 10^6 \text{ km}^2$  on September 30, marking the eleventh-lowest value since 1979 (Figures 2.9-1, 2.9-2, 2.9-3).

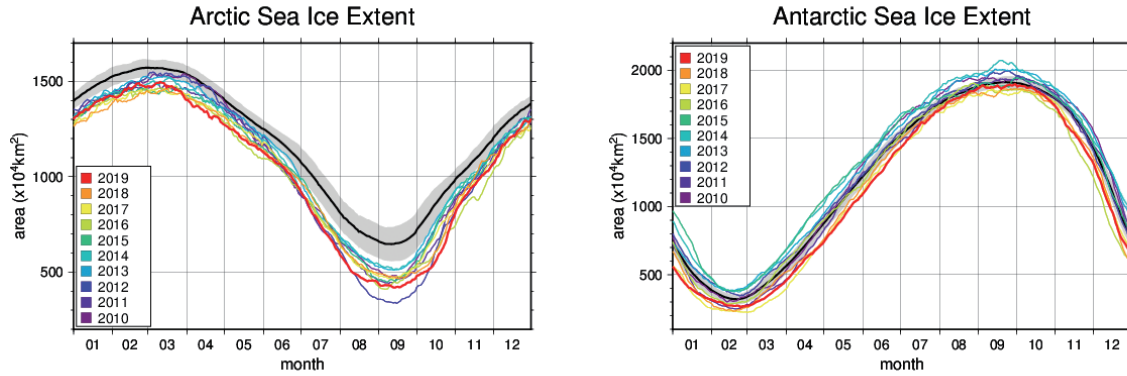


Figure 2.9-2 Annual variations of sea ice extent in the Arctic (left) and Antarctic (right) areas in 2019 (red line) Black lines represent the normal, and shading represents the range of the normal.

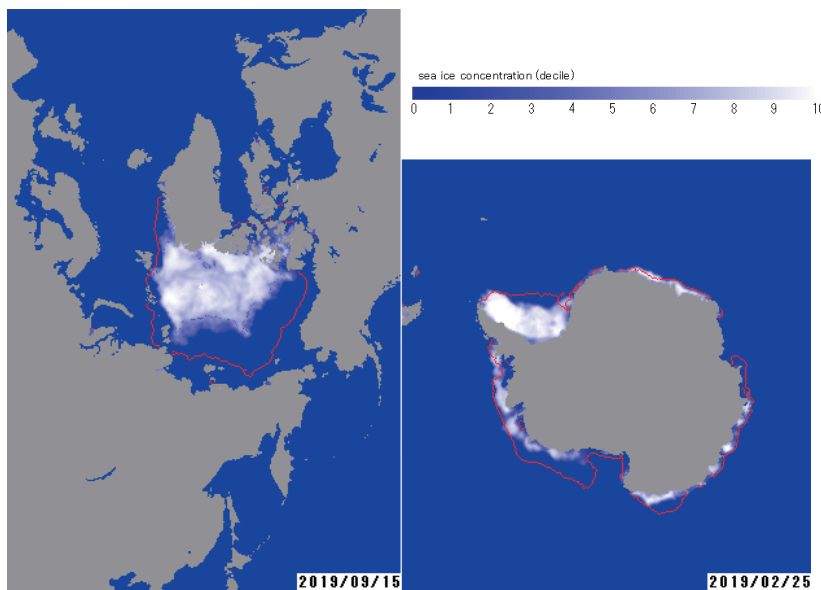


Figure 2.9-3 Annual minimum sea ice distribution for the Arctic and Antarctic

The figure on the left shows Arctic sea ice concentration on September 15 2019, and on the right is Antarctic sea ice concentration on February 25 2019. The red lines represent the normal sea ice edge for the relevant days.

### 2.9.2 Sea ice in the Sea of Okhotsk (Figure 2.9-4)

The Sea of Okhotsk is the southernmost sea in the Northern Hemisphere where sea ice is observed across a wide area. The variation of the sea ice in the Sea of Okhotsk has effect on climate in coastal area facing the Sea of Okhotsk in Hokkaido and water quality of Oyashio.

The maximum<sup>26</sup> sea ice extent in the Sea of Okhotsk shows large interannual variations. However, it is virtually certain that it exhibited a long-term trend of decrease for the period from 1971 to 2019 (statistically significant at the confidence level of 99%). The maximum extent has decreased by  $0.062 \times 10^6 \text{ km}^2$  per decade (corresponding to 3.9% of the Sea of Okhotsk's total area).

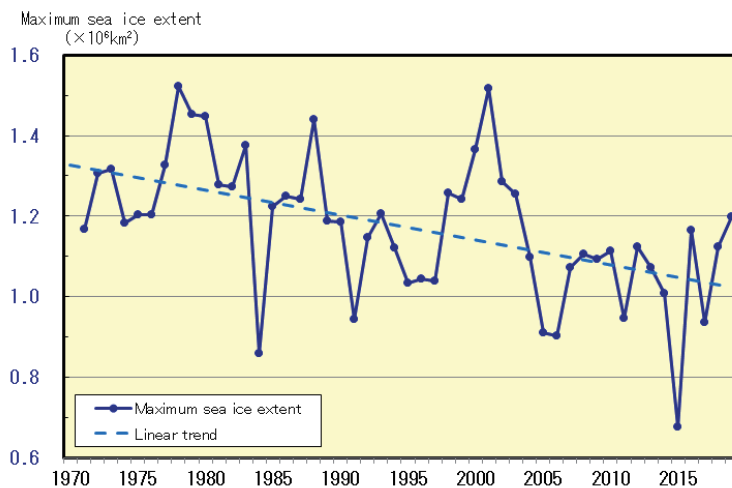


Figure 2.9-4 Time-series representations of maximum sea ice extent for the Sea of Okhotsk from 1971 to 2019

Straight line indicates the linear trend.

<sup>26</sup> The maximum sea ice extent: It shows sea ice extent that sea ice was the most expanding of every five days in the winter.

## 2.10 Snow cover in the Northern Hemisphere

- It is extremely likely that a decreasing trend is observed in the interannual variability of the total snow cover extent in the Northern Hemisphere for January, June and the period from September to December and in Eurasia for June and the period from September to December.
- In winter 2018/2019, there were more days of snow cover than normal over the western and central part of North America, and fewer over the northeastern part of East Asia.

JMA monitors snow-cover variations in the Northern Hemisphere using analysis data from satellite observations<sup>27</sup> based on its own algorithm. The average seasonal migration of snow cover in the Northern Hemisphere normally peaks around January - February and decreases in spring.

In the Northern Hemisphere (north of 30°N), it is extremely likely (statistically significant at a confidence level of 95%) that a decreasing trend is observed in the interannual variability of the total snow cover extent over the 32-year period from 1988 to 2019 for January, June and the period from September to December, while no discernible trend is seen for the period from February to May (Figure 2.10-1 (a) and (c)). In Eurasia (north of 30°N from 0° to 180°E), it is extremely likely (statistically significant at a confidence level of 95%) that a decreasing trend is observed in the interannual variability of the total snow cover for June and the period from September to December, while no discernible trend is seen for the period from January to May (Figure 2.10-1 (b) and (d)). In winter (December to February) 2018/2019, there were more days of snow cover than normal over the western and central part of North America, and fewer over the northeastern part of East Asia (Figure 2.10-1 (e)). In November 2019, there were more days of snow cover than normal over the central part of North America, and fewer from eastern Europe to western Russia and over the northeastern part of East Asia (Figure 2.10-1 (f)).

The albedo of snow-covered ground (i.e., the ratio of solar radiation reflected by the surface) is higher than that of snow-free ground. The variability of snow cover has an impact on the earth's surface energy budget and radiation balance, and therefore on the climate. In addition, snow absorbs heat from its surroundings and melts, thereby providing soil moisture and related effects on the climate system. The variability of atmospheric circulation and oceanographic conditions affects the amount of snow cover, which exhibits a close and mutual association with climatic conditions. Snow-cover variations in Eurasia and other parts of the Northern Hemisphere may affect climate conditions in Japan, but the mechanisms behind such a potential influence remain unclear. The accumulation of future observation data in addition to the current body of information and the implementation of related research are expected to increase the reliability of statistical work to identify trends of snow cover extent and help to elucidate how snow-cover variations affect climate conditions.

---

<sup>27</sup> The Defense Meteorological Satellite Program (DMSP) polar-orbiting satellites of the USA, equipped with the Special Sensor Microwave/Imager (SSM/I) and the Special Sensor Microwave Imager Sounder (SSMIS)

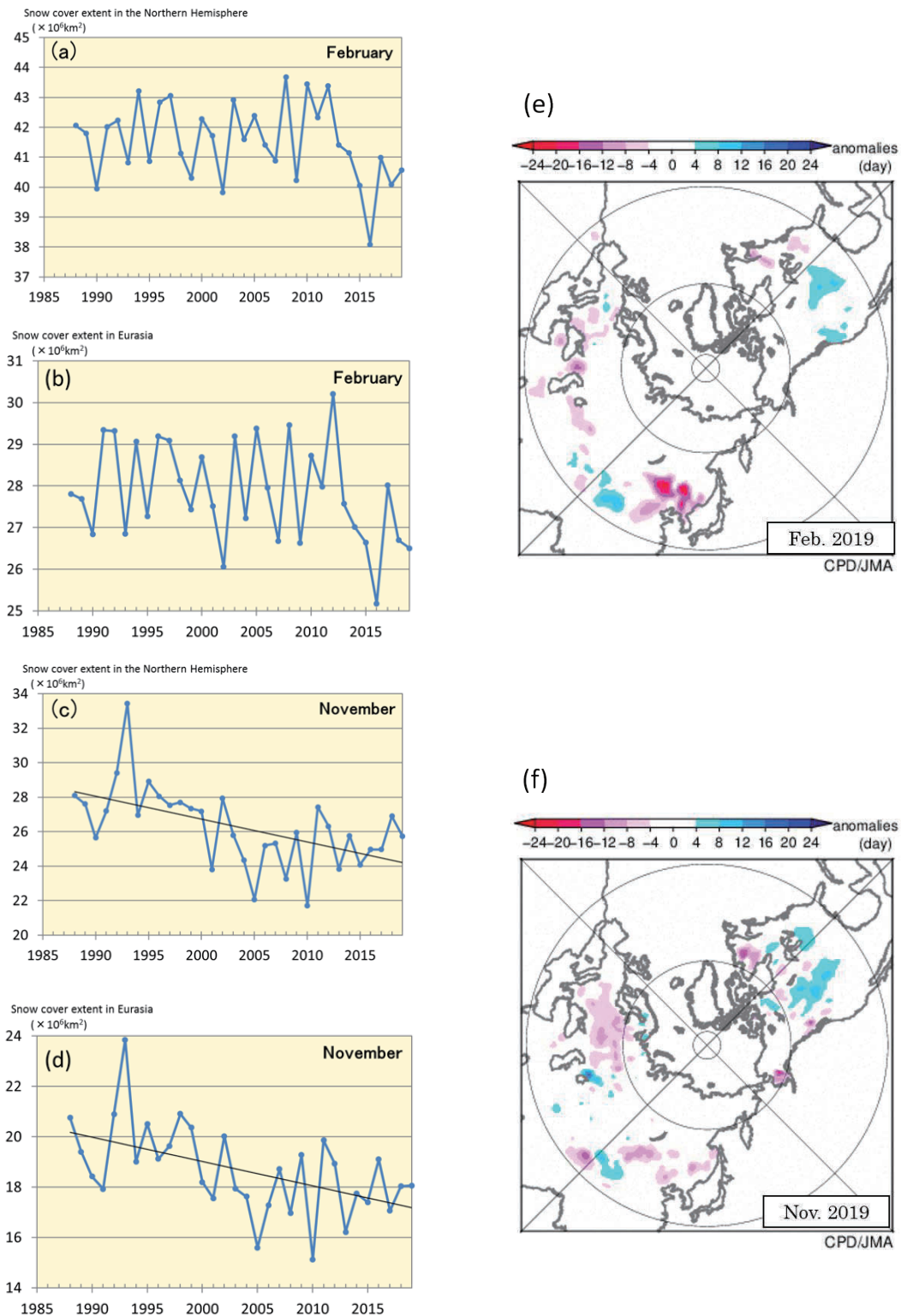


Figure 2.10-1 Interannual variations in the total area of monthly snow cover ( $\text{km}^2$ ) in the Northern Hemisphere (north of  $30^\circ\text{N}$ ) for (a) February and (c) November and in Eurasia (north of  $30^\circ\text{N}$ , from  $0^\circ$  to  $180^\circ\text{E}$ ) for (b) February and (d) November from 1988 to 2019, and anomalies in the number of days with snow cover for (e) February and (f) November in 2019

(a) - (d): The blue lines indicate the total snow cover area for each year, and the black lines show linear trends (statistically significant at a confidence level of 95%).

(e) - (f): Blue (red) shading indicates more (fewer) days of snow cover.

The base period for the normal is 1989 – 2010.

## Chapter 3 Atmospheric and Marine Environment Monitoring<sup>28</sup>

### 3.1 Monitoring of greenhouse gases<sup>29</sup>

- Concentrations of carbon dioxide both in the air and in oceans are increasing.
- Concentrations of atmospheric methane have shown an ongoing increase (with the exception of a stationary phase from 1999 to 2006).
- Concentrations of atmospheric nitrous oxide are increasing.

JMA operates the World Data Centre for Greenhouse Gases (WDCGG)<sup>30</sup> to collect, maintain and provide data on greenhouse gases for related monitoring on a global scale under the Global Atmosphere Watch (GAW) Programme of the World Meteorological Organization (WMO). Analysis of data reported to WDCGG shows that the global mean concentration of greenhouse gases with strong impacts on global warming (in particular, carbon dioxide (CO<sub>2</sub>), methane (CH<sub>4</sub>) and nitrous oxide (N<sub>2</sub>O)) continues to increase (Table 3.1-1).

In Japan, JMA monitors surface-air concentrations of greenhouse gases via three observation stations at Ryori in Ofunato, Minamitorishima in the Ogasawara Islands and Yonagunijima in the Nansei Islands. JMA research vessels are used to observe oceanic and atmospheric CO<sub>2</sub> in sea areas near Japan and in the western North Pacific. In addition, sampling of greenhouse gases in upper-air areas using cargo aircraft was commenced in 2011 (Figure 3.1-1).

Table 3.1-1 Atmospheric concentrations of major greenhouse gases (2018)<sup>31</sup>

	Atmospheric mole fraction			Absolute increase from 2017	Relative increase from 2017	Lifetime
	Pre-industrial level around 1750	Global mean in 2018	Relative increase from Pre-industrial level			
Carbon dioxide	About 278 ppm	407.8 ppm	+ 47 %	+2.3 ppm	+0.57 %	-
Methane	About 722 ppb	1,869 ppb	+159 %	+10 ppb	+0.54 %	12.4 years
Nitrous oxide	About 270 ppb	331.1 ppb	+ 23 %	+1.2 ppb	+0.36 %	121 years

28 In this chapter, data from the period until 2018 are used for certain results where time is needed for collection and analysis of observation data regarding greenhouse gases around the world.

29 Information on greenhouse gas monitoring is published on JMA's website.

[https://www.data.jma.go.jp/ghg/info\\_ghg\\_e.html](https://www.data.jma.go.jp/ghg/info_ghg_e.html) (Atmospheric greenhouse gases)

[https://www.data.jma.go.jp/gmd/kaiyou/english/oceanic\\_carbon\\_cycle\\_index.html](https://www.data.jma.go.jp/gmd/kaiyou/english/oceanic_carbon_cycle_index.html) (oceanic greenhouse gases and ocean acidification)

30 See the WDCGG website for more information.

<https://gaw.kishou.go.jp/>

31 Data on the annual mean mole fraction in 2018 and its absolute and relative differences from the previous year are from WMO (2019), while data on pre-industrial levels and lifetime are from IPCC (2013). The lifetime of gas as referred to here describes the time scale over which a local instantaneous increment of gas decays. The increase from pre-industrial levels is calculated from mole fractions for the pre-industrial era and 2018.

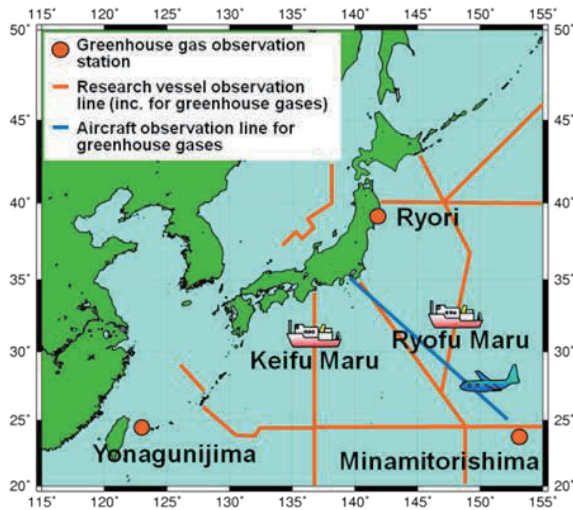


Figure 3.1-1 JMA's greenhouse gas observation network

Observation stations at Ryori, Minamitorishima and Yonagunijima and regular monitoring routes of research vessel and cargo aircraft

### 3.1.1 Concentration of carbon dioxide

#### (1) Concentration of global atmospheric carbon dioxide

The global mean concentration of atmospheric CO<sub>2</sub> shows a trend of increase with ongoing seasonal variations (Figure 3.1-2), primarily due to influences associated with human activity such as fossil fuel combustion and deforestation. Some anthropogenic CO<sub>2</sub> is absorbed by the terrestrial biosphere and the oceans, while the rest remains in the atmosphere. As most major sources of CO<sub>2</sub> are located in the Northern Hemisphere, concentrations tend to be higher in the mid- and high latitudes there and lower in the Southern Hemisphere (Figure 3.1-3).

The seasonal variability of CO<sub>2</sub> concentration is generally attributable to terrestrial biosphere activity. In summer, active plant photosynthesis consumes masses of CO<sub>2</sub>, while emissions from plant respiration and organic-matter decomposition become dominant in winter. As a result, the annual maximum concentration is observed from March to April in the Northern Hemisphere and from September to October in the Southern Hemisphere. Seasonal variations exhibit larger amplitudes in the mid- and high latitudes of the Northern Hemisphere than in the ocean-rich Southern Hemisphere (Figure 3.1-3). Accordingly, the global mean CO<sub>2</sub> concentration usually peaks around April, reflecting the seasonal variations of the Northern Hemisphere.

WDCGG analysis shows that global mean surface CO<sub>2</sub> concentration increased by 2.3 ppm from 2017 to 2018, reaching as much as 407.8 ppm (Table 3.1-1). The most recent 10-year average annual growth rate is 2.3 ppm/year, as opposed to the corresponding value of 1.5 ppm/year for the 1990s.

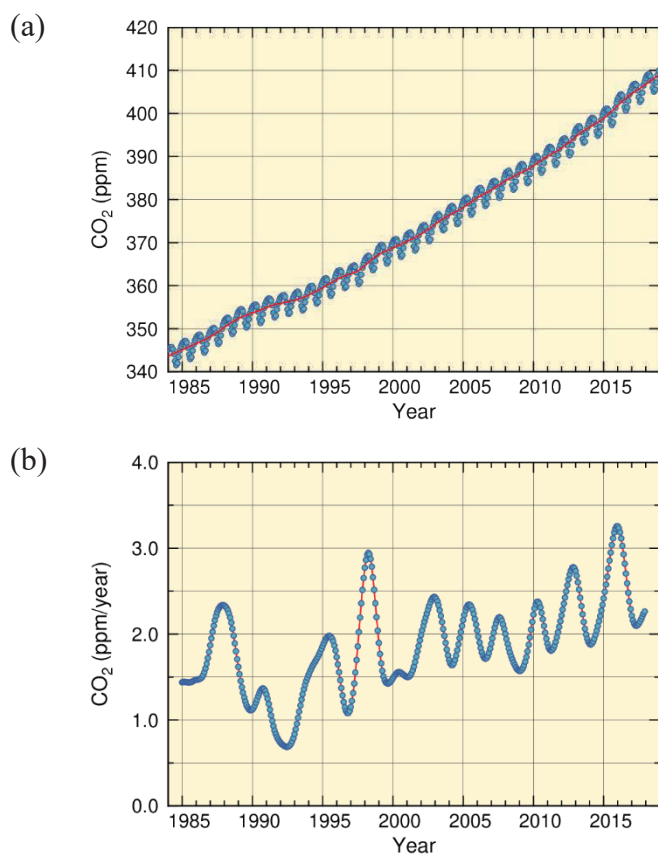


Figure 3.1-2 Global mean concentration of atmospheric CO<sub>2</sub> (a) and annual growth rate (b)

In the upper panel the blue dots are monthly values, and the red line represents the corresponding sequence after removal of seasonal variations. From the latter, the growth rate is derived and shown in the lower panel. Graph content is based on analysis of observation data reported to WDCGG using the method of WMO (2009). Data contributors are listed in WMO (2020).

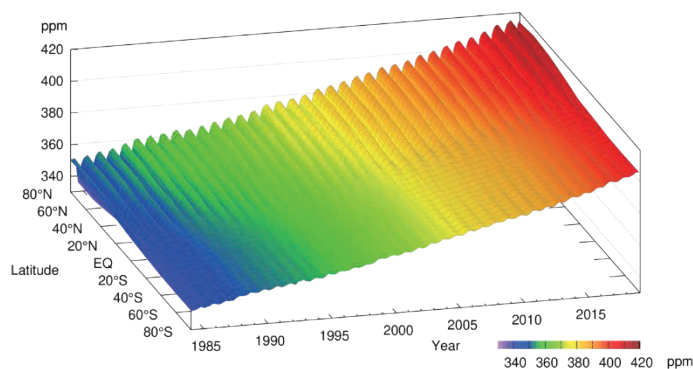


Figure 3.1-3 Latitudinal distribution of atmospheric CO<sub>2</sub> concentrations

The data set and analysis method are as per Figure 3.1-2.

The growth rate of CO<sub>2</sub> concentration exhibits significant interannual variations (Figure 3.1-2 (b)). Major increases in concentration often coincide with El Niño events, largely because the terrestrial biosphere emits more CO<sub>2</sub> than usual under such conditions. In particular, El Niño events bring about high temperatures and droughts in tropical areas and elsewhere, thereby promoting plant respiration and organic-matter decomposition in soil and hindering plant photosynthesis (Keeling *et al.*, 1995; Dettinger and Ghil, 1998).

Figure 3.1-4 illustrates net CO<sub>2</sub> uptake by the terrestrial biosphere as estimated using the method of Le Quéré *et al.* (2016). Here, CO<sub>2</sub> uptake is defined as the amount of anthropogenic emissions minus the increment of atmospheric concentration and the amount of uptake by oceans. The low uptake by the terrestrial biosphere in 2015 and 2016 is generally attributed to the 2014 – 2016 El Niño event (WMO, 2018b). The annual net CO<sub>2</sub> uptake in 2015 and 2016 was  $2.1 \pm 1.1$  GtC/year and  $1.8 \pm 1.1$  GtC/year, respectively, both of which were lower than the 10-year average of  $3.2 \pm 1.0$  GtC/year for the period 2008 – 2017. Similar suppression of net CO<sub>2</sub> uptake was observed in association with the El Niño events of 1997/1998 and 2002/2003. In 1998 in

particular, the lowest net uptake since 1990 was recorded. An exception was observed from 1991 to 1992, when net CO<sub>2</sub> uptake by the terrestrial biosphere was large despite the presence of an El Niño event. This is attributable to the eruption of Mt. Pinatubo in June 1991, which triggered worldwide low temperatures and inhibited CO<sub>2</sub> emissions from organic-matter decomposition in soil (Keeling *et al.*, 1996; Rayner *et al.*, 1999).

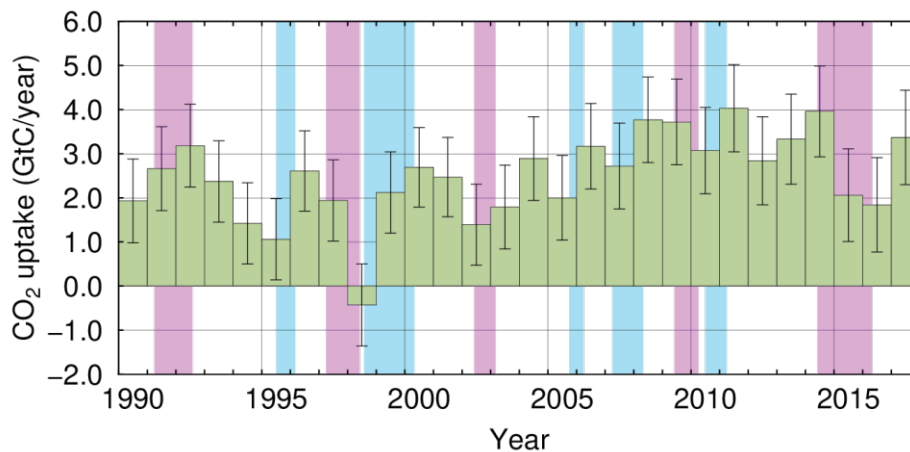


Figure 3.1-4 Annual net CO<sub>2</sub> uptake by the terrestrial biosphere

In this analysis, the net CO<sub>2</sub> uptake is estimated by subtracting the annual increment of atmospheric CO<sub>2</sub> and the amount of uptake by oceans from the amount of anthropogenic emissions. The amount of anthropogenic emissions, stemming from fossil fuel combustion and land-use changes, is based on Friedlingstein *et al.* (2019). The annual increment of atmospheric CO<sub>2</sub> is the annual mean of the monthly means shown in Figure 3.1-2 (b). Oceanic uptake is based on Iida *et al.* (2015; see also Section 3.1.1 (3)), and incorporates emissions associated with the natural carbon cycle, corresponding to 0.7 GtC/year (IPCC 2013). Error bars indicate 68% confidence levels. El Niño and La Niña periods are shaded in red and blue, respectively. A negative CO<sub>2</sub> uptake equates to an emission.

## (2) Concentration of atmospheric carbon dioxide in Japan

Concentrations of atmospheric CO<sub>2</sub> at all three of Japan's observation stations have shown a continuous increase along with seasonal variations (Figure 3.1-5 (a)). The amplitude of these variations is greater at Ryori than at the other stations because it tends to be larger in higher latitudes of the Northern Hemisphere in association with significant seasonal variations in terrestrial biosphere activity in the mid- and high latitudes (see Figure 3.1-1). Although Yonagunijima and Minamitorishima have similar latitudes, the former tends to observe higher concentrations and seasonal variations with larger amplitudes because of its greater proximity to the Asian continent, which is characterized by major anthropogenic emissions and an extensive biosphere. The annual mean CO<sub>2</sub> concentration in 2019 was 414.0 ppm at Ryori, 412.2 ppm at Minamitorishima and 414.8 ppm at Yonagunijima. All these figures are the highest on record (based on preliminary estimations).

Figure 3.1-5 (b) shows growth rates of CO<sub>2</sub> concentrations observed at the three observation stations. High rates have been observed in most cases during the periods of El Niño events. As a recent example, a sharp increase in CO<sub>2</sub> concentration was observed in association with the event that ran from summer 2014 to spring 2016.

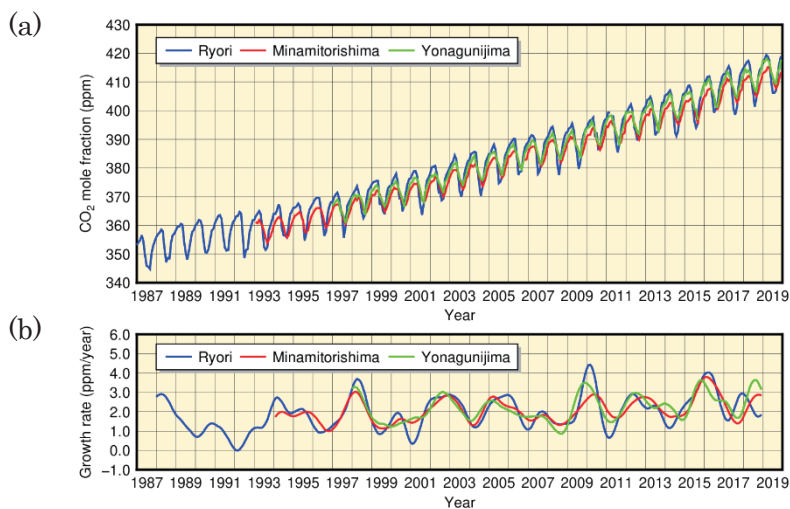


Figure 3.1-5 Monthly mean concentrations (a) and corresponding growth rates (b) of atmospheric CO<sub>2</sub> observed at Ryori (blue), Minamitorishima (red) and Yonagunijima (green)

The method used to calculate the growth rate is described in WMO (2009).

### (3) Oceanic carbon dioxide

Based on data collected by JMA research vessels along the 137°E (3 – 34°N) and 165°E (5°S – 35°N) lines, oceanic and atmospheric *p*CO<sub>2</sub> are increasing in the western North Pacific area (Figures 3.1-6, 3.1-7). The growth rates for oceanic and atmospheric *p*CO<sub>2</sub> along the 137°E line from 1985 to 2019 were 1.5 – 2.0 and 1.7 – 1.9 μatm/year, respectively, while those along the 165°E line from 1996 to 2019 were 1.5 – 3.1 and 1.7 – 2.1 μatm/year, respectively. Oceanic *p*CO<sub>2</sub> exhibits seasonal variations, being higher in summer with higher SSTs and lower in winter with lower SSTs, and the range of variation is more volatile at higher latitudes along both lines. Meanwhile, atmospheric *p*CO<sub>2</sub> is constant and higher than those of oceanic *p*CO<sub>2</sub> except in summer. Consequently, the ocean absorbs atmospheric CO<sub>2</sub> emissions overall, other than in equatorial areas, resulting in a release of CO<sub>2</sub> into the atmosphere over the year because oceanic *p*CO<sub>2</sub> values are higher than those of atmospheric *p*CO<sub>2</sub>.

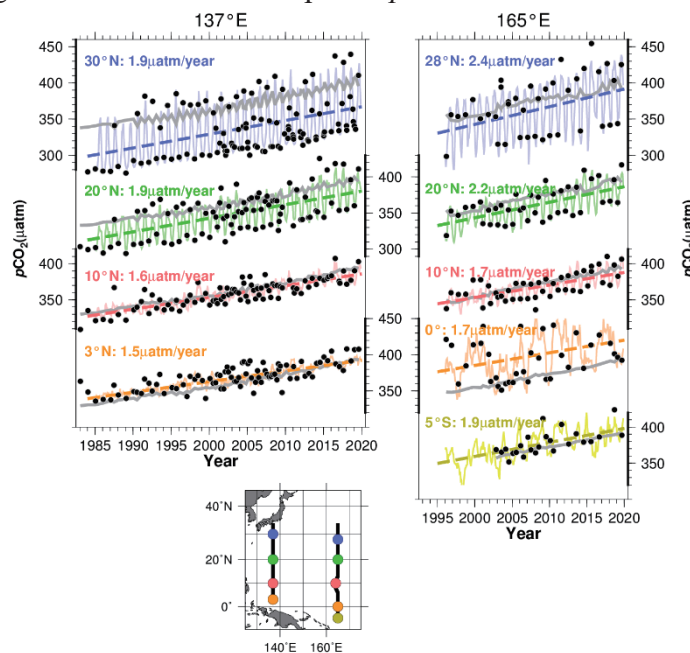


Figure 3.1-6 Annual changes in oceanic and atmospheric *p*CO<sub>2</sub> along the 137°E (left) and the 165°E (right) lines.

Black plots show oceanic *p*CO<sub>2</sub> observation values. Solid lines represent monthly oceanic *p*CO<sub>2</sub> values reconstructed using the method of Ishii et al. (2011), dashed lines show the long-term trend of oceanic *p*CO<sub>2</sub>, and gray lines indicate the observed values of atmospheric *p*CO<sub>2</sub>.

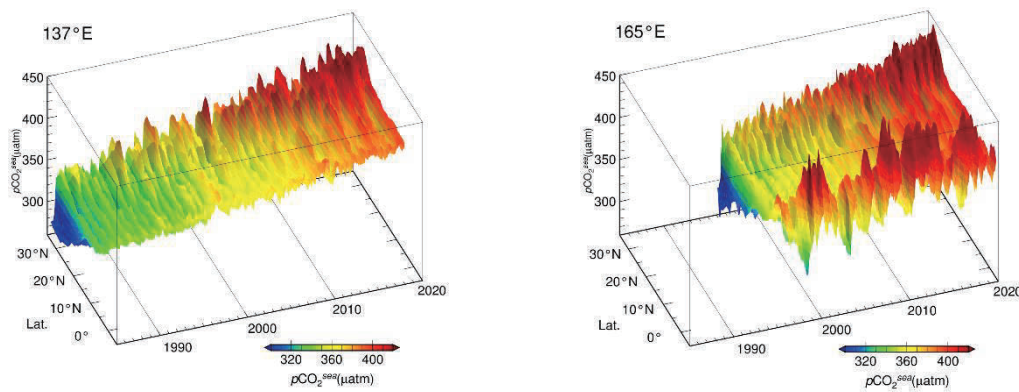


Figure 3.1-7 Time-latitude distribution of oceanic  $p\text{CO}_2$  along the 137°E (left) and the 165°E (right) lines. Colors indicate reconstructed monthly oceanic  $p\text{CO}_2$  value. The part on the left shows oceanic  $p\text{CO}_2$  along the 137°E (3-34°N) since 1985 and the part on the right shows oceanic  $p\text{CO}_2$  along the 165°E (5°S-35°N) since 1996.

Analysis of observation data reveals relationships between surface seawater  $\text{CO}_2$  concentrations and other oceanographic parameters such as sea surface temperature (SST), salinity and chlorophyll-a concentration, which differ by region. Global oceanic  $\text{CO}_2$  concentrations were estimated using datasets of such parameters based on these relationships, and  $\text{CO}_2$  exchanges between the atmosphere and the ocean were calculated (Iida *et al.*, 2015). It was found that the ocean releases  $\text{CO}_2$  into the atmosphere in equatorial regions and the northern Indian Ocean, where seawater with a high  $\text{CO}_2$  concentration upwells and absorbs  $\text{CO}_2$  in other regions (Figure 3.1-8 (a)). Lower SSTs in winter and biological  $\text{CO}_2$  consumption in spring/autumn result in lower surface ocean  $\text{CO}_2$  concentrations and therefore higher  $\text{CO}_2$  uptake, especially in the mid-to-high latitudes. Figure 3.1-8 (b) and (c) show monthly and annual variations in global ocean  $\text{CO}_2$  uptake, respectively. The estimated mean annual global ocean  $\text{CO}_2$  uptake during 1990 to 2018 was 2.0 GtC per year. Considering natural  $\text{CO}_2$  efflux of 0.7 GtC per year (IPCC, 2013), which results from riverine input to the oceans, the amount of oceanic  $\text{CO}_2$  uptake corresponds to 30 % of all anthropogenic  $\text{CO}_2$  emission, which IPCC (2013) estimates to be 9 GtC per year. Global ocean  $\text{CO}_2$  uptake is affected by the variability of global SST distribution and biological activity, and decreases/increases in boreal summer/winter (Figure 3.1-8 (b)). The estimated annual global ocean  $\text{CO}_2$  uptake has increased since 2000.

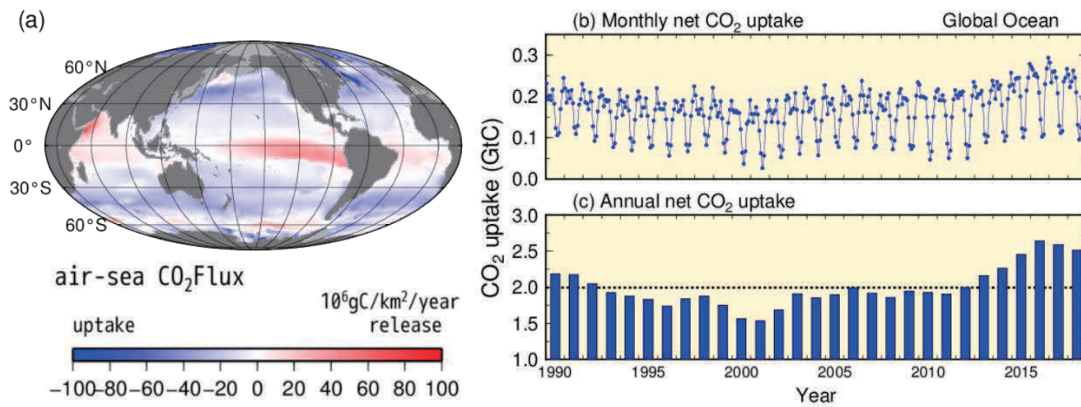


Figure 3.1-8 Distribution of global ocean CO<sub>2</sub> uptake/release for 2018 (a) and time-series representations of monthly (b) and annual (c) CO<sub>2</sub> uptake from 1990 to 2018

The blue/red area in the map on the left (a) indicates ocean uptake/release of CO<sub>2</sub> from/into the atmosphere. The grey area shows the border of the region analyzed. The dotted line in graph (c) shows the 2.0 GtC average for the period from 1990 to 2018.

The column inventory of oceanic CO<sub>2</sub> was estimated using long-term time-series data on dissolved inorganic carbon from 1990s (Figure. 3.1-9). The column inventory rates of oceanic CO<sub>2</sub> between the sea surface and 27.5  $\sigma_\theta$  (1,200 to 1,400 m in depth) along 137°E and 165°E are approximately 5 – 12 and 3 – 12 tC·km<sup>-2</sup>·year<sup>-1</sup>, respectively. The column inventory rates of oceanic CO<sub>2</sub> around 20 – 30°N are higher than those at 10°N and 35°N. This is caused by the transport of CO<sub>2</sub> from the surface to the ocean interior by water masses known as North Pacific subtropical mode water and North Pacific intermediate water.

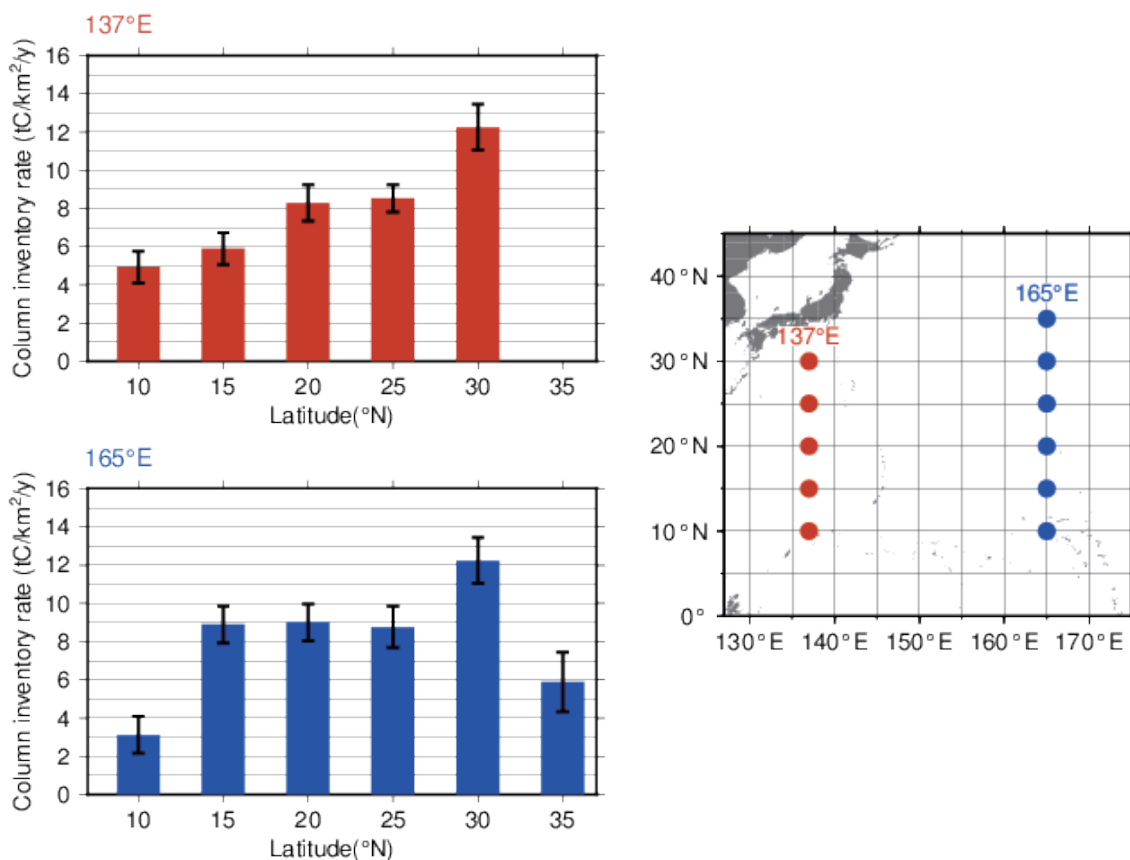


Figure 3.1-9 Changes in oceanic CO<sub>2</sub> between the sea surface and 27.5  $\sigma_\theta$  (approx. 1,200 – 1,400 m in depth) along 137 and 165°E for the periods 1994 – 2019 and 1992 – 2019.

Error bars denote a 95% confidence level

#### (4) Ocean acidification

The ocean acts as a large sink for CO<sub>2</sub> emitted as a result of human activity, and the chemical properties of seawater have changed due to the uptake and reserve of anthropogenic CO<sub>2</sub>. Ocean acidification, known as the decrease in seawater pH (hydrogen ion exponents), is a particular issue of concern because it accelerates global warming by limiting the ocean's capacity of CO<sub>2</sub> uptake from the atmosphere and affects marine ecosystems by disturbing plankton growth. The IPCC AR5 (2013) included an estimate that the average global surface seawater pH has decreased by 0.1 due to ocean uptake of atmospheric CO<sub>2</sub> emitted as a result of human activity since the beginning of the industrial era (1750). According to numerical model experiments based on future CO<sub>2</sub> emission estimates, surface seawater pH will further decrease by 0.065 – 0.31 by the end of 21st century. The CO<sub>2</sub> absorbed by the ocean is considered to have been transported into the ocean interior through ocean circulation and biological processes, and to be causing ocean acidification in the interior as well as in the surface layer (Doney et al., 2009).

JMA has long conducted oceanographic observations in the western North Pacific to monitor long-term variability relating to the ocean, such as global warming and ocean acidification. The Agency monitor long-term trends in surface and interior seawater pH along repeat hydrographic lines at 137°E and 165°E, and performs analysis to determine the average decrease in surface seawater pH throughout the Pacific using data on oceanic CO<sub>2</sub> concentration and related factors. The results clearly show a decreasing trend in surface seawater pH for the whole Pacific, and 0.014 to 0.021 and 0.014 to 0.030 per decade at individual stations on the 137°E and 165°E lines, respectively (Figures 3.1-10 and 3.1-11). Ocean interior pH along these lines also shows decreasing trends of 0.010 to 0.034 per decade (Figure 3.1-12) with higher rates in the northern than the southern subtropics due to greater accumulation of anthropogenic CO<sub>2</sub> in the former.

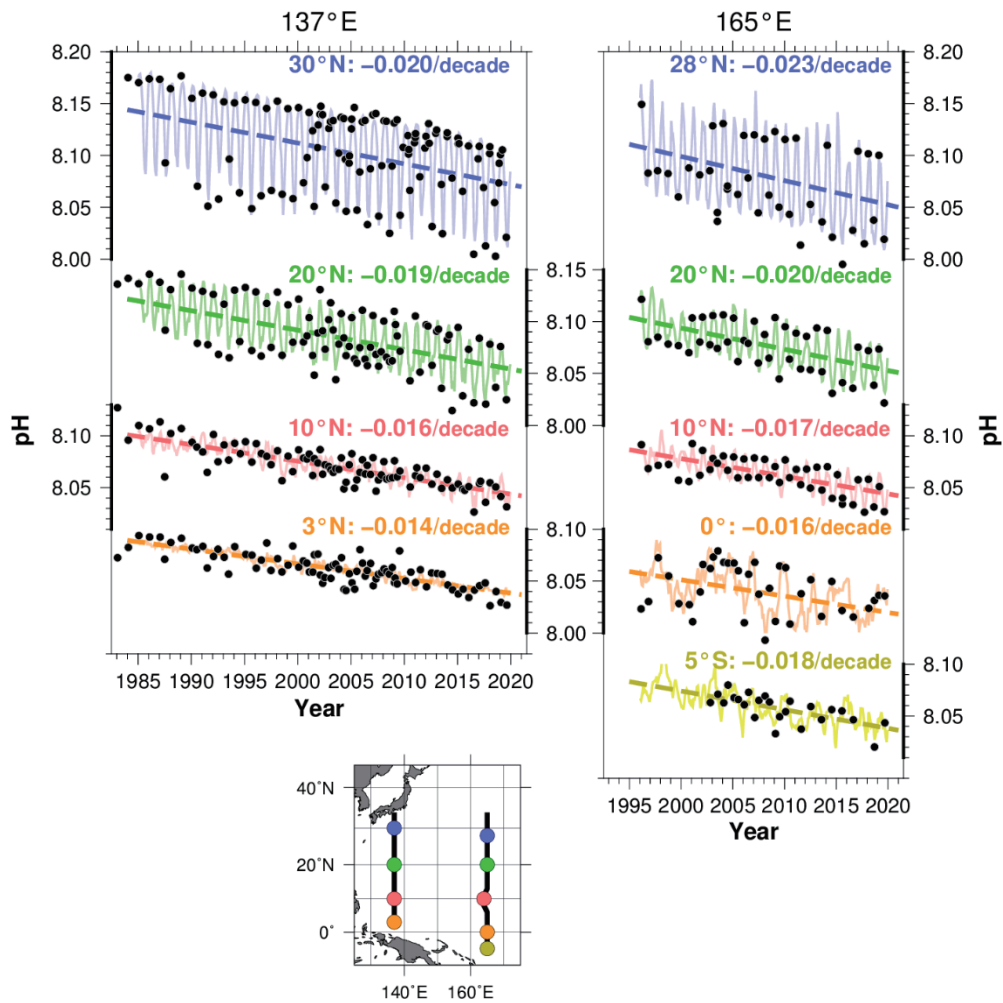


Figure 3.1-10 Long-term trends of pH at each latitude in JMA's repeat hydrographic lines at 137°E (left) and 165°E (right).

Black plots show pH observation values based on  $p\text{CO}_2$  observation data. Solid lines represent monthly pH values reconstructed using the method of Ishii et al. (2011), dashed lines show the long-term trend of pH, and numbers indicate rates of change at each latitude.

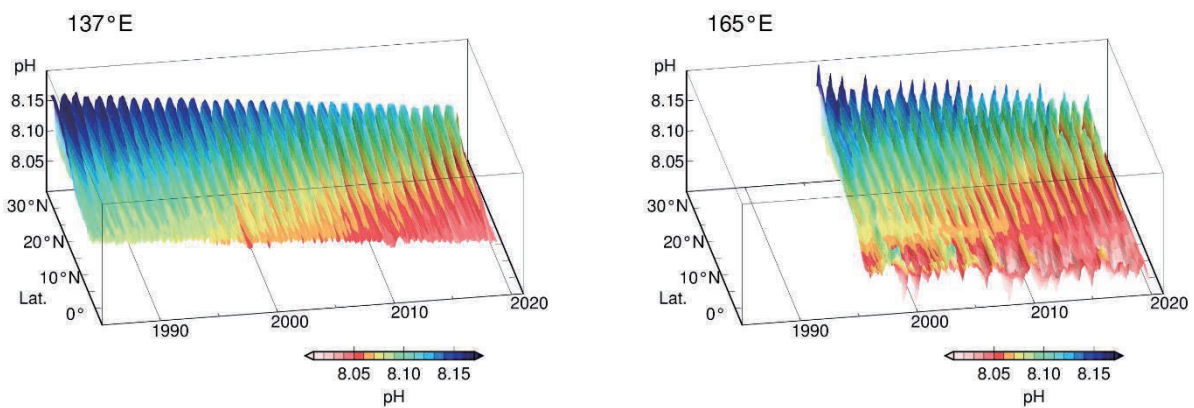


Figure 3.1-11 Time-latitude distribution of pH along the 137°E (left) and the 165°E (right) lines.

Colors indicate reconstructed monthly pH values. The part on the left shows pH along 137°E (3-34°N) since 1985, and the part on the right shows pH along 165°E (5°S-35°N) since 1996.

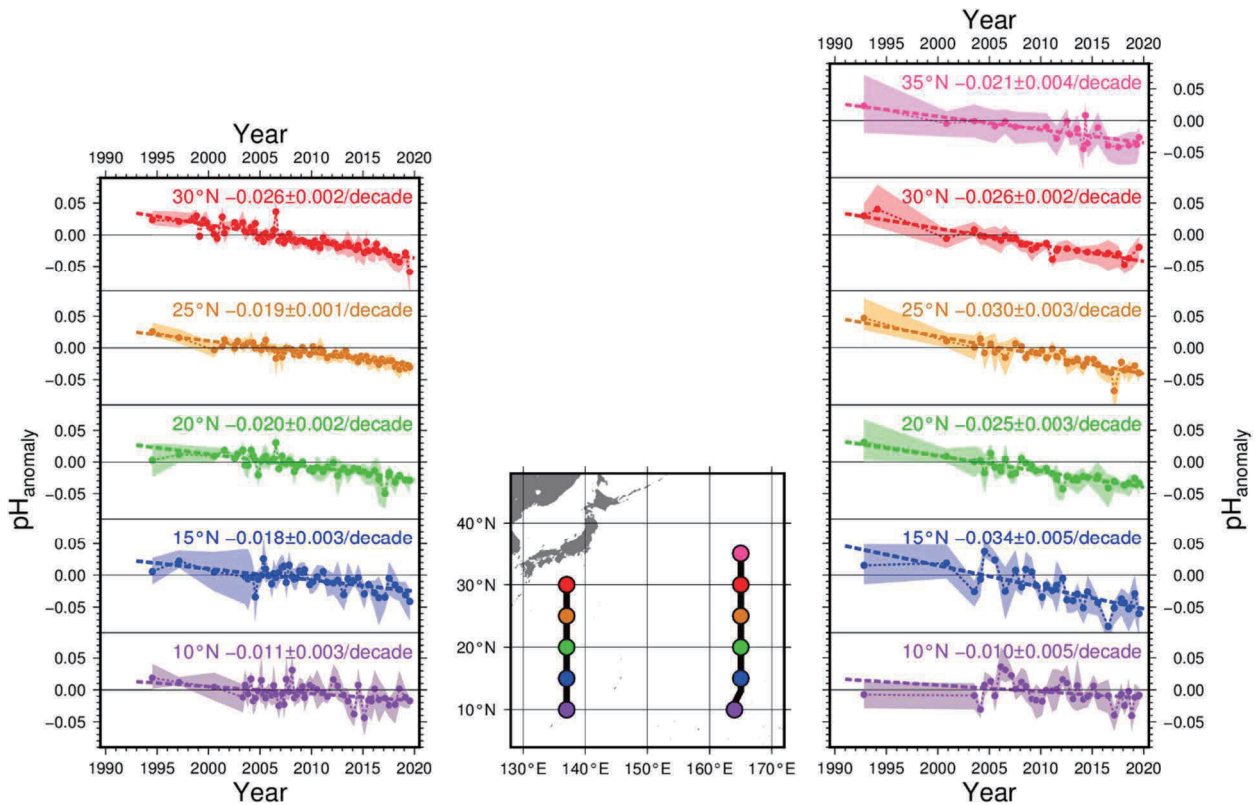


Figure 3.1-12 Long-term trends of pH between  $25.0 \sigma_{\theta}$  and  $26.9 \sigma_{\theta}$  (a depth range of about 150–800 m) along  $137^{\circ}\text{E}$  (left) and  $165^{\circ}\text{E}$  (right).

Plots show pH anomalies from the normal (i.e., the average for the period from 1991 to 2010) at each latitude. The shaded areas and bold dotted lines represent the standard deviation range ( $\pm 1 \sigma$ ) and the long-term trend, respectively. The numbers indicate rates of change at each latitude.

##### (5) Concentration of carbon dioxide in the upper air

Since 2011, JMA has monitored upper-air  $\text{CO}_2$  concentrations using cargo aircraft with support from Japan Ministry of Defense, with air samples taken along the route from Atsugi Air Base ( $35.45^{\circ}\text{N}$ ,  $139.45^{\circ}\text{E}$ ) to Minamitorishima Island ( $24.29^{\circ}\text{N}$ ,  $153.98^{\circ}\text{E}$ ) during level flight at an altitude of approximately 6 km and during descent<sup>32</sup> to the island once a month (Tsuboi *et al.*, 2013; Niwa *et al.*, 2014).

Figure 3-1.13 shows measured and averaged concentrations for samples collected during level flight in black and blue dots, respectively. Monthly mean concentrations at the ground-based station on the island are also shown in red. The dashed curves in blue and red represent components after removal of seasonal cycles for aircraft and Minamitorishima, respectively. Concentrations exhibit a gradual increase over time in the upper air as well as on the surface, although values tend to be lower in the former.

Figure 3-1.14 shows the vertical dependence of average seasonal cycles based on air samples collected during descent in addition to level-flight data and ground-based data. To allow direct comparison, these monthly values are calculated by averaging concentrations after removal of long-term trends in surface observation data. At each level, the information shows similar seasonal variations with higher values from winter to spring and lower values from summer to

<sup>32</sup> Although some air samples are taken during ascent flights from Minamitorishima Island, all vertical samplings are referred to here as descent samplings.

fall, while significant vertical dependence with lower values toward higher altitudes is observed from winter to spring. Consequently, the amplitude of seasonal cycles is smaller in the upper air.

Figure 3-1.15 shows concentrations for samples taken during descent minus the daily mean value recorded at the ground-based station on the flight date for February (left) and August (right). While concentrations are lower toward higher altitudes in February, there is no clear vertical dependence in August.

The above results suggest that parts of surface air affected by the terrestrial biosphere in continental regions are transported to the ground and upper levels of the island, and that air transport behavior varies with seasons and altitudes. The characteristic of strong vertical dependence from winter to spring and weak dependence from summer to fall is also identified in data from other aircraft observations around North America and Asia (Sweeney *et al.*, 2015; Umezawa *et al.*, 2018).

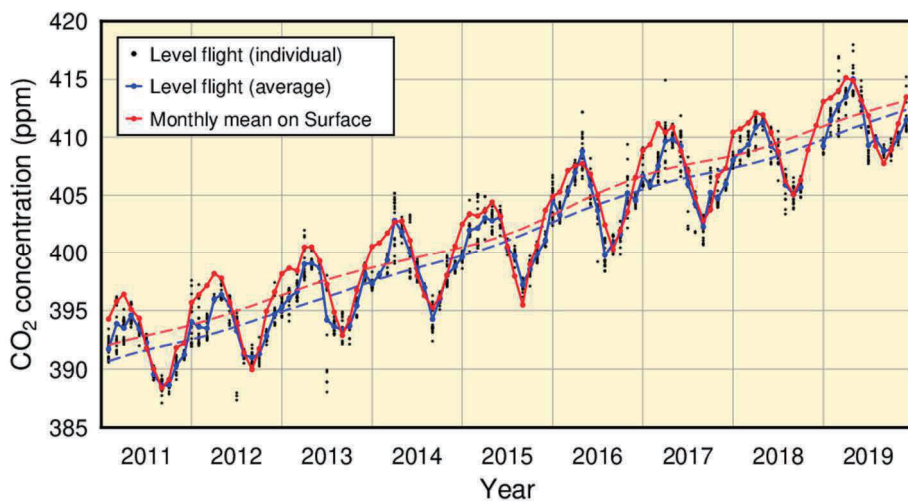


Figure 3.1-13 Measured and averaged CO<sub>2</sub> concentrations for air samples collected during level flight (at a height of approx. 6 km) of cargo aircraft along the route from Atsugi Air Base to Minamitorishima (black and blue dots, respectively) and monthly mean concentrations at the Minamitorishima ground-based station (red dots).

Blue and red dashed lines represent components after the removal of seasonal cycles from the series of blue and red dots, respectively. The analysis is based on WMO (2009).

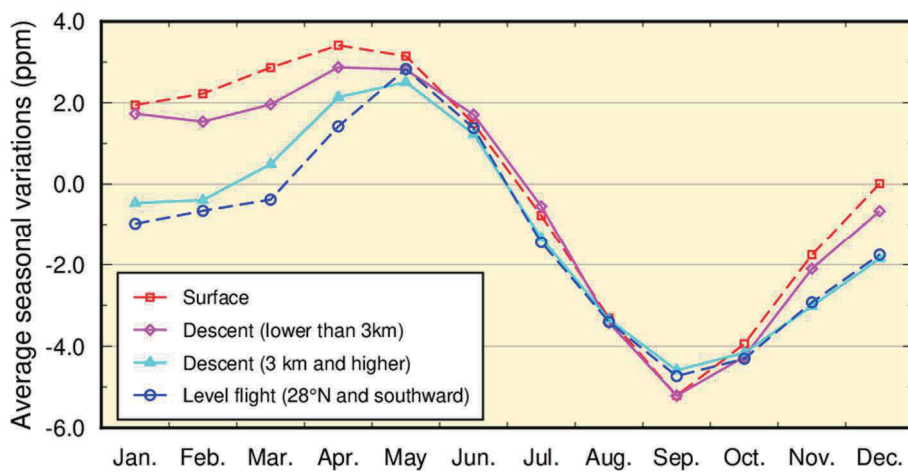


Figure 3.1-14 Vertical dependence of average seasonal cycles around Minamitorishima for monthly mean concentrations on the surface (red), concentrations for air samples taken during

(Chapter 3 Atmospheric and Marine Environment Monitoring)

level flight at latitudes 28°N and southward (blue), and those taken during descent with altitudes less than 3 km (magenta) and otherwise (cyan).

Monthly values are calculated by averaging concentrations after removal of long-term trends (components without seasonal cycles) for surface observation data (the red dashed line in Figure 3.1-13).

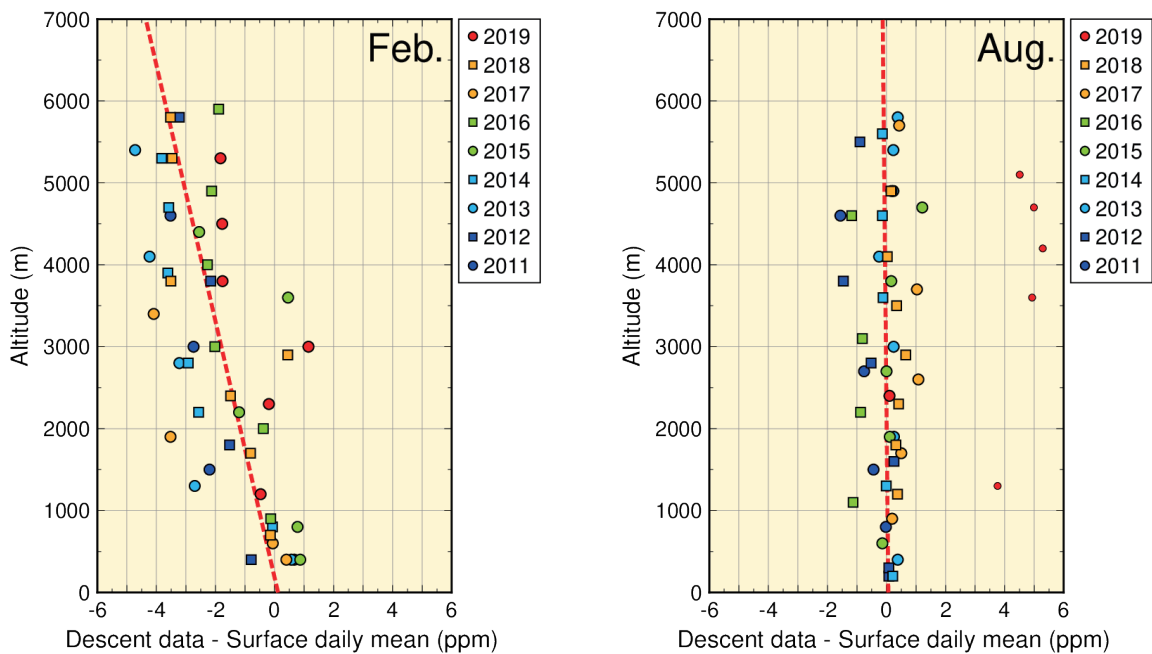


Figure 3.1-15 Vertical variations of CO<sub>2</sub> concentrations over Minamitorishima

Circles and squares show concentrations of air samples taken during descent to the island minus the daily mean value recorded at the ground-based station on the flight date. Symbol colors and shapes represent observation years. Dashed red lines show the vertical gradient of the symbols as determined using the least squares method. To determine representative characteristics for the observation area, outlier data (small symbols) beyond the 3 sigma of the residual standard deviation from the fitted line are excluded from calculation for the vertical gradient. On the flight date in August 2019, daily mean concentration on the surface was 4 – 5 ppm lower than that during descent because continental air masses with low CO<sub>2</sub> concentrations were transported to areas near the ground around Minamitorishima.

### 3.1.2 Concentration of methane

#### (1) Concentration of global atmospheric methane

The global mean concentration of atmospheric CH<sub>4</sub> has been increasing since at least the mid-1980s when worldwide monitoring began, except for a stationary phase from 1999 to 2006 (Figure 3.1-16). The mechanism behind the stationary phase remains unclear, but several scenarios have been proposed (IPCC, 2013). The greater concentrations observed since 2007 indicate an increase in CH<sub>4</sub> emissions from tropical wetlands and human activity in the mid-latitudes of the Northern Hemisphere (WMO, 2019).

WDCGG analysis shows that the global mean concentration of CH<sub>4</sub> in 2018 was 1,869 ppb, which is the highest since records began (Table 3.1-1).

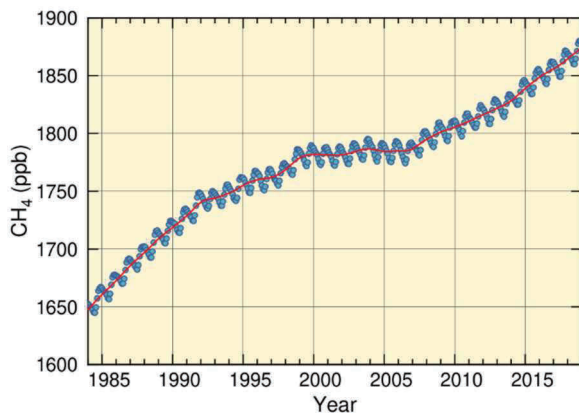


Figure 3.1-16 Global mean concentration of atmospheric CH<sub>4</sub>

The blue dots are monthly values, and the red line represents the corresponding sequence after the removal of seasonal variations. Graph content is based on analysis of observation data reported to WDCGG based on the method of WMO (2009). Data contributors are listed in WMO (2020).

Figure 3.1-17 shows the latitudinal dependence of CH<sub>4</sub> concentrations. Values are lower in the tropics than in the high and mid-latitudes of the Northern Hemisphere because CH<sub>4</sub> is mostly emitted from land areas in the Northern Hemisphere, and disappears due to reaction with hydroxyl radicals<sup>33</sup> over tropical oceans during transportation to the Southern Hemisphere. In summer, more CH<sub>4</sub> is destroyed because more hydroxyl radicals are produced as a result of enhanced ultraviolet radiation and water vapor. This reaction contributes to seasonal variations of CH<sub>4</sub> concentrations in both hemispheres, with lower values in summer and higher values in winter (Figures 3.1-16 and 3.1-17).

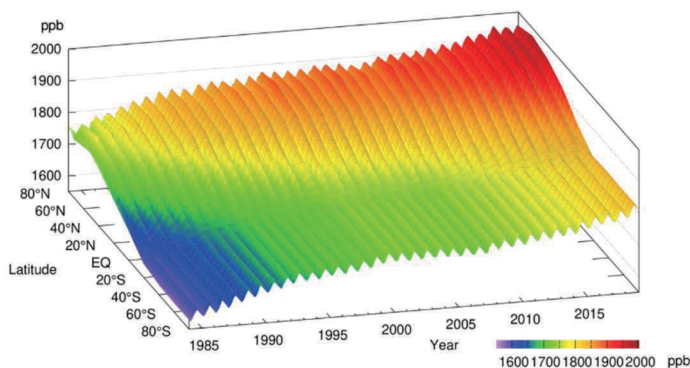


Figure 3.1-17

Latitudinal distribution of atmospheric CH<sub>4</sub> concentrations  
The data set and analysis method are as per Figure 3.1-16.

<sup>33</sup> Hydroxyl radicals are highly reactive chemicals generated by the reaction of atomic oxygen, which is derived from UV photolysis of ozone, with airborne water vapor. It is particularly abundant at low latitudes, where UV radiation is strong and water vapor is plentiful.

The remarkable increase observed in global mean atmospheric concentrations of CH<sub>4</sub> since the industrial era (+159%) has been much more rapid than that of CO<sub>2</sub> (+47%) (Table 3.1-1). This is partly because the amount of anthropogenic emissions of CH<sub>4</sub> relative to natural emissions exceeds that of CO<sub>2</sub>. The long-term trend of CH<sub>4</sub> concentration depends on various factors of uncertainty, including anthropogenic/natural emissions and chemical reactions. Accordingly, further development of the global CH<sub>4</sub> observation network is required.

(2) Concentration of atmospheric methane in Japan

Atmospheric CH<sub>4</sub> concentrations at all of Japan’s three observation stations exhibit a trend of increase with seasonal variations in the same way as the global mean concentration (Figure 3.1-18 (a)). Ryori usually observes the highest concentration among the three stations because it is located in the northern part of Japan, where CH<sub>4</sub> sources in the Asian continent are more influential and reaction with hydroxyl radicals is less marked. Although Yonagunijima and Minamitorishima are located at similar latitudes, the former tends to record higher concentrations in winter because CH<sub>4</sub> sources on the Asian continent have a stronger impact there in winter as a result of continental air mass expansion. In summer, meanwhile, a hydroxyl radical-rich maritime air mass covers both stations, and similarly low concentrations are observed. Since 2010, Yonagunijima has occasionally observed concentrations as high as those of Ryori in winter. The annual mean CH<sub>4</sub> concentration in 2019 was 1,954 ppb at Ryori, 1,902 ppb at Minamitorishima and 1,928 ppb at Yonagunijima, all of which are the highest on record (based on preliminary estimations).

The growth rate of atmospheric CH<sub>4</sub> concentration exhibits interannual variations that differ significantly from station to station (Figure 3.1-18 (b)).

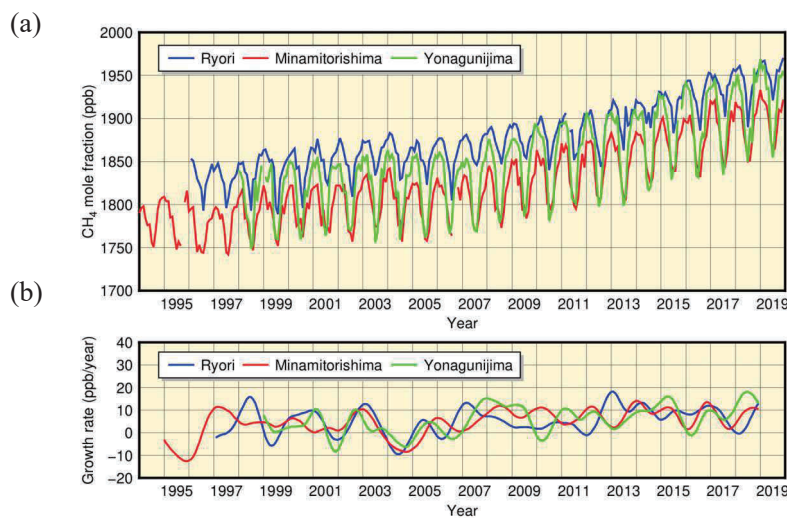


Figure 3.1-18

Monthly mean concentrations (a) and corresponding growth rates (b) of atmospheric CH<sub>4</sub> observed at Ryori (blue), Minamitorishima (red) and Yonagunijima (green)

The method for calculating the growth rate is described in WMO (2009).

### 3.1.3 Concentration of nitrous oxide

Figure 3.1-19 shows that the global mean concentration of atmospheric N<sub>2</sub>O has been continuously increasing. The annual mean concentration in 2018 was 331.1 ppb, which was 23% above the pre-industrial level of 270 ppb (Table 3.1-1). Seasonal variations of N<sub>2</sub>O concentrations are lower than those of CO<sub>2</sub> and CH<sub>4</sub> because N<sub>2</sub>O has a longer lifetime (121 years). The hemispheric mean concentration is approximately 1 ppb higher in the Northern Hemisphere than in the Southern Hemisphere (Figure 3.1-20) because there are more sources of anthropogenic emissions in the former. This interhemispheric difference is, however, much smaller than those observed with CO<sub>2</sub> and CH<sub>4</sub>.

The atmospheric N<sub>2</sub>O concentration at Ryori exhibits characteristics similar to those of the global mean (Figure 3.1-21). The annual mean concentration in 2019 at Ryori was 333.8 ppb (based on preliminary estimations).

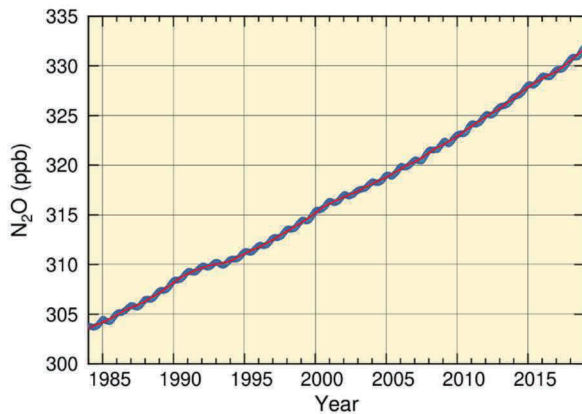


Figure 3.1-19 Global mean concentration of atmospheric N<sub>2</sub>O

The blue dots are monthly values, and the red line represents the corresponding sequence after the removal of seasonal variations. Graph content is based on analysis of observation data reported to WDCGG based on the method of WMO (2009). Data contributors are listed in WMO (2020).

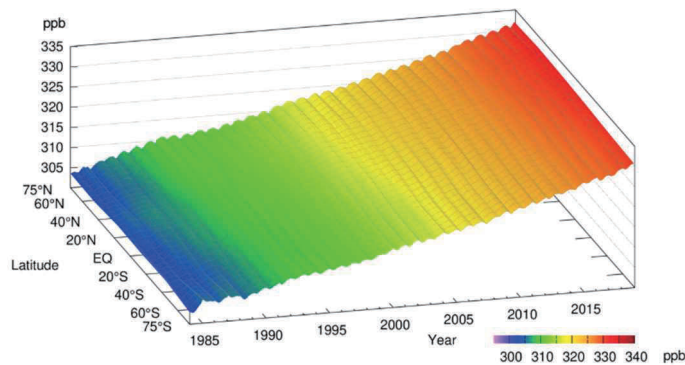


Figure 3.1-20 Latitudinal distribution of atmospheric N<sub>2</sub>O concentrations

The data set and analysis method are as per Figure 3.1-19.

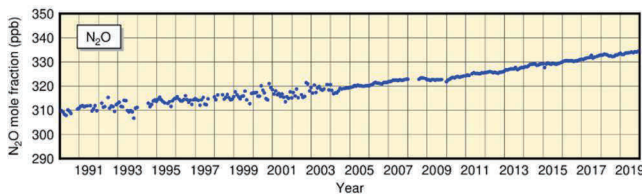


Figure 3.1-21

Monthly mean concentrations of atmospheric N<sub>2</sub>O at Ryori

Improvement of observation equipment in 2004 resulted in improved stability of measurements.

## 3.2 Monitoring of the ozone layer and ultraviolet radiation<sup>34</sup>

- Global-averaged total ozone amount decreased significantly in the 1980s and the early 1990s, and remains low today with a slightly increasing trend.
- The annual maximum size of the Antarctic ozone hole increased substantially in the 1980s and 1990s, but a statistically significant decreasing trend since 2000 has been identified.
- UV radiation levels at three domestic sites have increased since the early 1990s. Annual cumulative daily erythemal UV radiation at Tsukuba is virtually certain to have increased for the whole of the observational period at a rate of 4.3% per decade.
- Global atmospheric concentrations of chlorofluorocarbons (CFCs) have gradually decreased in recent years.

JMA monitors total ozone and/or vertical profiles of ozone at three domestic sites and one Antarctic site (Sapporo, Tsukuba, Naha and Syowa Station) under the Act on the Protection of the Ozone Layer through the Control of Specified Substances and Other Measures<sup>35</sup>. It also monitors UV radiation at Tsukuba and Syowa Station. JMA also monitors the surface concentration of CFCs at Ryori (Figure 3.2-1).

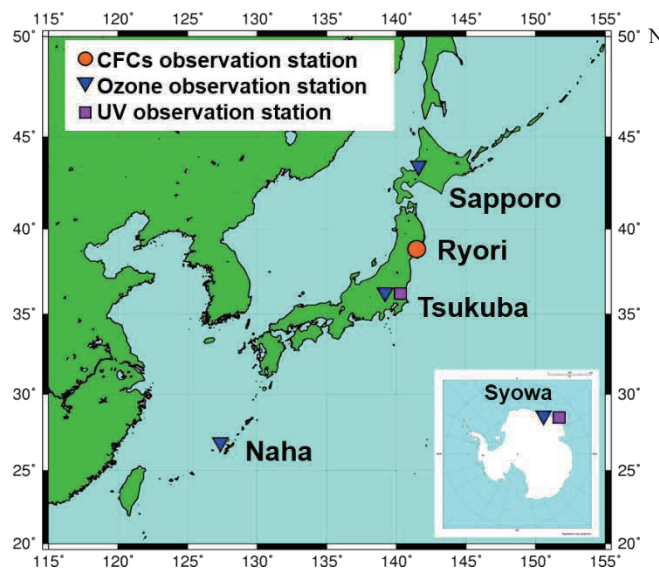


Figure 3.2-1 JMA's ozone layer and UV radiation observation network

### 3.2.1 Ozone layer

#### (1) Global ozone layer

Globally averaged total ozone amount decreased considerably in the 1980s and the early 1990s (Figure 3.2-2). Although uniformity or a slightly increasing trend has been observed since the mid-1990s, total ozone levels have remained lower than those seen before the 1980s. Global mean total ozone with enough data points for statistical analysis for the period 2014 – 2018 was slightly higher than the 1994 – 2008 mean and 3% lower than the 1970 – 1980 mean, which is a representative value for the period prior to the onset of ozone depletion. The total concentration

<sup>34</sup> Information on the ozone layer and ultraviolet radiation is published on JMA's website.

[https://www.data.jma.go.jp/gmd/env/ozonehp/en/diag\\_o3uv\\_e.html](https://www.data.jma.go.jp/gmd/env/ozonehp/en/diag_o3uv_e.html)

<sup>35</sup> Law No. 53 of May 20, 1988, Article 22: Observation and monitoring

1. The Director-General of the Meteorological Agency shall observe the state of the ozone layer and the atmospheric concentrations of specified substances and publish the results obtained.

of tropospheric chlorine, which causes ozone depletion, increased rapidly until the 1980s before the onset of a decreasing trend in the 1990s (Section 3.2.3). *Scientific Assessment of Ozone Depletion: 2018* (WMO, 2018a) reported that action taken under the Montreal Protocol has led to a reduction in the tropospheric and stratospheric abundance of controlled ozone-depleting substances (ODSs), and that upper-stratospheric ozone concentrations have increased since 2000.

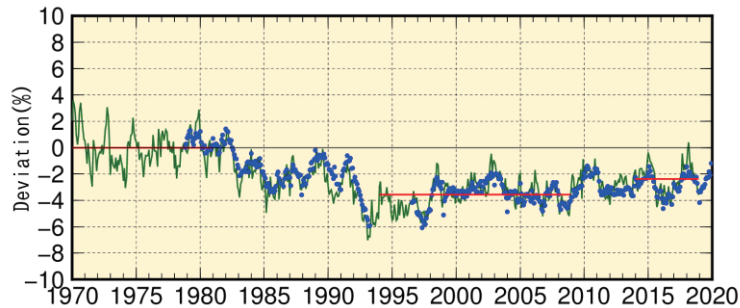


Figure 3.2-2 Time-series representation of global-averaged total ozone deviations shown as percentages  
 The green line represents deviations of monthly mean global-area-weighted total ozone from the 1970 – 1980 mean, the three red lines represent the 1970 – 1980 mean, the 1994 – 2008 mean and the mean over the last five years when there were enough data points for a statistical analysis (2014 – 2018), and the blue dots show NASA TOMS/OMI satellite data averaged at latitudes of 70°S – 70°N. Each data set is deseasonalized with respect to the whole observation period. A total of 114 ground-based stations were used for this calculation (91 in the Northern Hemisphere and 23 in the Southern Hemisphere).

## (2) Antarctic ozone hole<sup>36</sup>

The annual maximum size of the ozone hole in 2019 was the smallest since 1990, when large-scale ozone hole continuously began to be observed. The main factors behind this were meteorological conditions such as high stratospheric temperatures over the Antarctic (see Topics III). The annual maximum size of the ozone hole increased substantially in the 1980s and 1990s, but a statistically significant decreasing trend since 2000 has been identified.

The annual ozone hole size depends on regional inter-annual climate variations, but also shows decadal variations in line with total amounts of ODSs in the stratosphere. A report titled *Scientific Assessment of Ozone Depletion: 2018* (WMO, 2018a) stated that the Antarctic ozone hole is expected to gradually close, with springtime total column ozone in the 2060s returning to 1980 values.

<sup>36</sup> See the Glossary for terms relating to ozone hole.

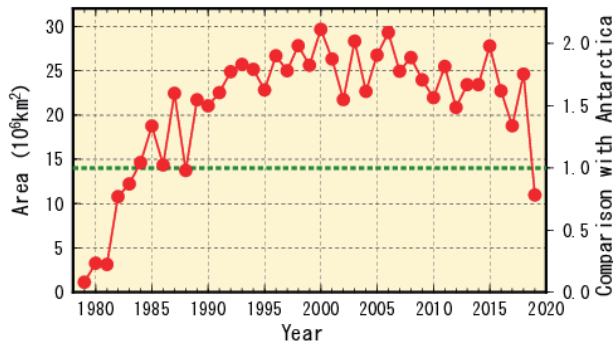


Figure 3.2-3 Time-series representation of the annual maximum size of the Antarctic ozone hole

The ozone hole area is defined as the region over which total ozone south of 45°S is equal to or less than 220 m atm-cm. NASA TOMS/OMI and NOAA-TOVS satellite data are used in calculation of the area for 1979 – 2019. The green line indicates the overall area of the Antarctic (13.9 million square kilometers). The left axis shows the ozone hole’s maximum area in units of million square kilometers, and the right axis shows its ratio to the area of Antarctica itself.

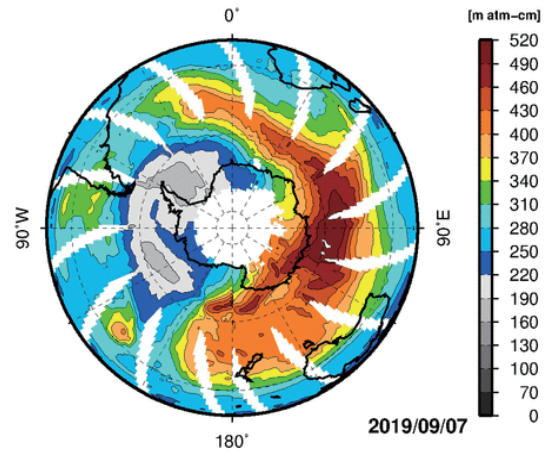


Figure 3.2-4 Southern Hemisphere distribution of total ozone on 7 September 2019, when the area of the ozone hole reached its maximum for the year

The unit is m atm-cm, and the map is produced using NASA OMI satellite data. The grey shading in the center shows the ozone hole area where the total ozone column value is 220 m atm-cm or less. White regions are domains where no satellite data were available.

### (3) Ozone layer over Japan

Figure 3.2-5 shows time-series representations of annual-mean total ozone observed at Sapporo, Tsukuba and Naha. A decrease is seen in the 1980s and the early 1990s at Sapporo and Tsukuba. After 2000, slightly increasing trends are observed at all three sites, but an ongoing trend of relatively low values has been seen in recent years at Naha.

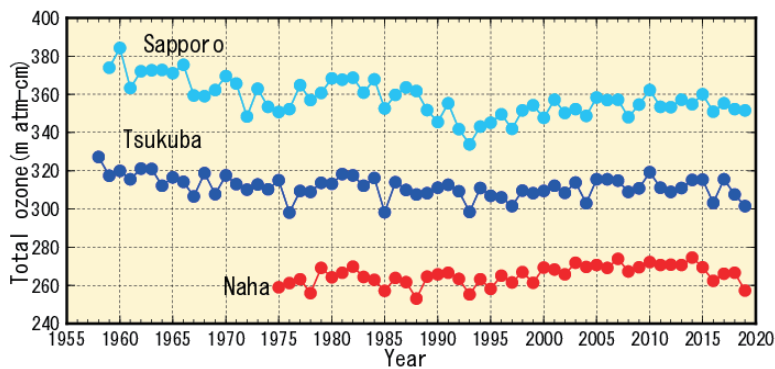


Figure 3.2-5 Time-series representations of annual-mean total ozone at stations in Japan

The stations here are at Sapporo, Tsukuba and Naha. JMA began observing total ozone at Tsukuba in 1957 and currently monitors total ozone and/or vertical profiles of ozone at three domestic sites (Sapporo, Tsukuba, Naha) and one Antarctic site (Syowa Station).

### 3.2.2 Solar UV radiation in Japan

UV radiation levels at three domestic sites have been increased from early-1990s. Annual cumulative daily erythemal UV radiation<sup>37</sup> at Tsukuba is virtually certain to have increased for the whole of the observational period by ratios of 4.3% per decade (Figure 3.2-6). At Sapporo, UV radiation levels increased from the mid-1990s to the 2000s. At Tsukuba, UV radiation levels increased in 1990s. At Naha, data show no marked changes since the increase observed in the 1990s. This phenomenon may be attributable to a decreasing tendency of mainly aerosols (UNEP, 2018).

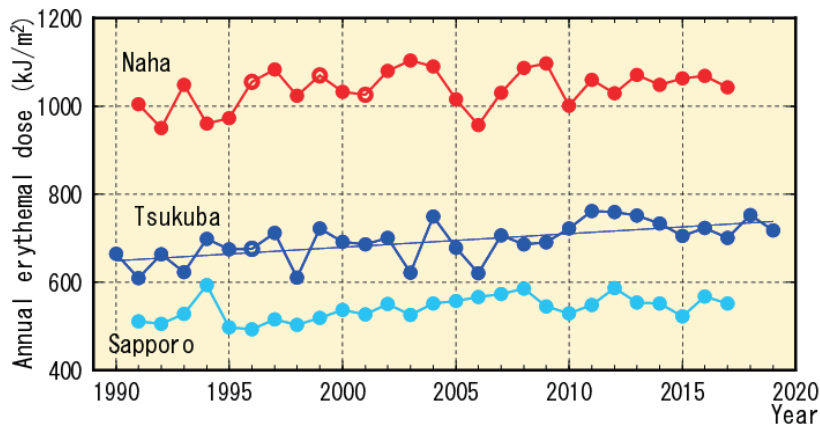


Figure 3.2-6 Time-series representations of annual cumulative daily erythemal UV radiation at stations in Japan. Observation of erythemal UV at Sapporo, Tsukuba and Naha in Japan started in the early 1990s. Each annual cumulative total is calculated from monthly-mean equivalent values multiplied by the number of days in each month. The monthly-mean equivalent value is based on calculation using daily values from which missing data are excluded. Open circles represent cases of at least a month in which there are fewer than 20 days of monitoring data. Regression lines cover the whole observation period (statistically significant at a confidence level of 99% for Tsukuba). UV radiation observations at Sapporo and Naha were terminated in January 2018.

### 3.2.3 Concentration of ozone-depleting substances

Chlorofluorocarbons (CFCs: CFC-11, CFC-12 and CFC-113), which are compounds of carbon, fluorine and chlorine, and other halogenated gases are ozone-depleting substances (ODSs). They are regulated under the 1987 Montreal Protocol on Substances that Deplete the Ozone Layer and its Amendments and Adjustments. Although ODSs have atmospheric concentrations equivalent to about a millionth of CO<sub>2</sub> levels at most, they contribute considerably to global warming because of their significant radiative effects per unit mass, some of which are several thousand times greater than that of CO<sub>2</sub>.

#### (1) Global concentration of ozone-depleting substances

Global concentrations of atmospheric CFCs increased rapidly until the 1980s before entering a decreasing trend in the 1990s (Figure 3.2-7). The concentration of CFC-11 peaked in 1992 – 1994, and has since shown a decreasing tendency. The concentration of CFC-12 increased until around 2003, and has also since shown a decreasing tendency. The concentration of CFC-113 reached its maximum in around 1993 in the Northern Hemisphere and around 1996 in the Southern Hemisphere. Differences in the concentrations of these gases between the Northern Hemisphere, where most emissions sources are located, and the Southern Hemisphere, which has significantly fewer sources, have decreased since the 1990s in contrast to the situation of the 1980s. These observations indicate that the CFC emission controls under the Montreal Protocol have been effective.

<sup>37</sup> See the Glossary for terms relating to erythemal UV radiation.

However, a slowdown in the decline of CFC-11 concentrations has been observed since 2012 (WMO, 2018a; WMO, 2018b; Montzka *et al.*, 2018; Rigby *et al.*, 2019), with decreasing rate approximately two thirds of those seen in the preceding decade. Numerical model calculation reporting by Montzka *et al.* (2018) attributed this to increased global CFC-11 emissions with main sources probably located in eastern Asia.

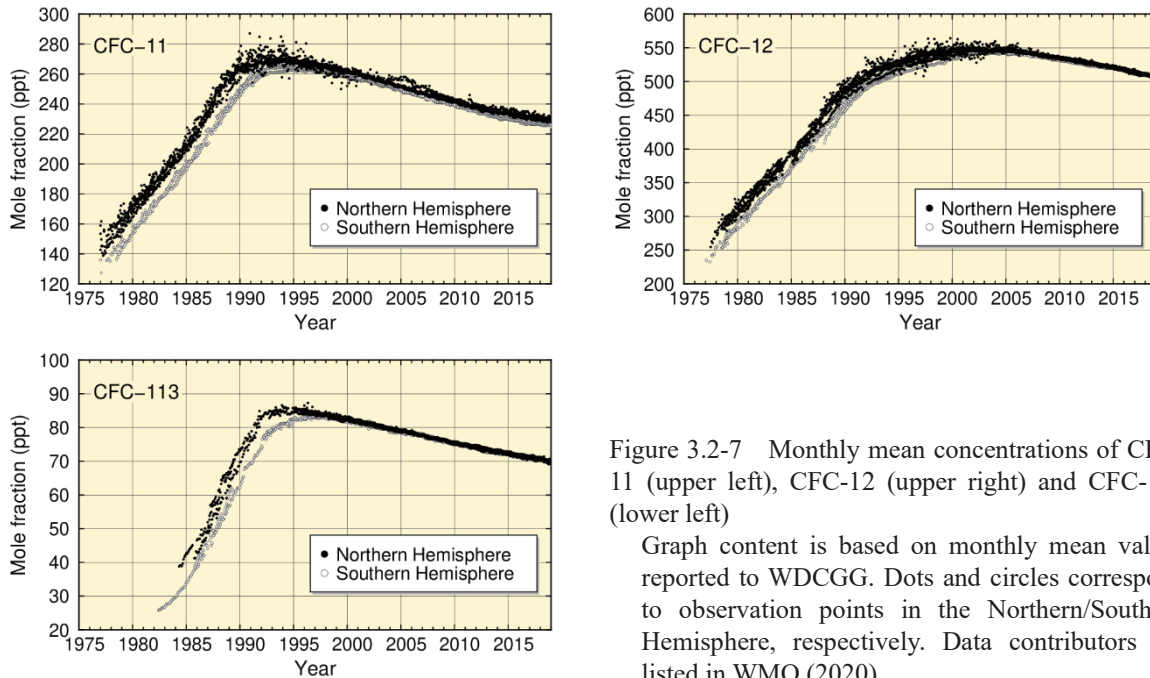


Figure 3.2-7 Monthly mean concentrations of CFC-11 (upper left), CFC-12 (upper right) and CFC-113 (lower left)

Graph content is based on monthly mean values reported to WDCGG. Dots and circles correspond to observation points in the Northern/Southern Hemisphere, respectively. Data contributors are listed in WMO (2020).

(2) Concentration of ozone-depleting substances in Japan

Concentrations of CFC-11, CFC-12 and CFC-113 at Ryori have shown decreasing tendencies since reaching maxima in various years (Figure 3.2-8). The concentration of CFC-11 peaked at about 270 ppt in 1993 – 1994, and has since decreased. The distinct peak of concentration observed in 2011 is considered attributable to emissions from polyurethane foam insulation materials released by the Great East Japan Earthquake and the subsequent hugely destructive tsunami of 11 March 2011 (Saito *et al.*, 2015). The rate of increase in CFC-12 concentration slowed around 1995, and a gradual decrease has been seen since 2005. There was no clear tendency of increase or decrease in the concentration of CFC-113 until 2001, but a decreasing tendency has been seen since then.

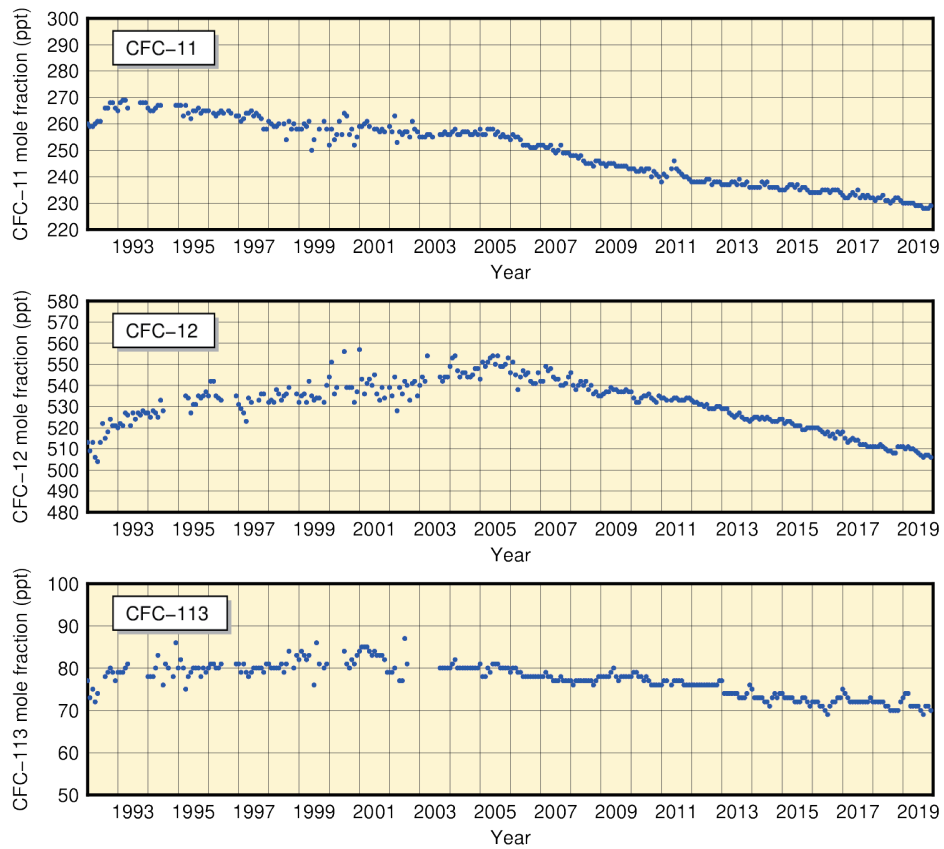


Figure 3.2-8 Monthly mean atmospheric concentrations of CFC-11 (top), CFC-12 (middle) and CFC-113 (bottom) at Ryori

Improvement of observation equipment in 2003 resulted in improved stability of measurements.

### 3.3 Monitoring of aerosols and surface radiation<sup>38</sup>

- In Japan, background atmospheric turbidity coefficient values (which depend on concentrations of aerosols, water vapor and other constituents in the air) have returned to approximate levels seen before the eruption of Mt. Agung in 1963. This is mainly because of no large-scale eruptions impacting the global climate since that of Mt. Pinatubo in 1991.
- The number of days when any meteorological station in Japan observed Kosa was 8 in 2019, and the total number of stations reporting its occurrence during the year was 16.

#### 3.3.1 Aerosols

Interannual variations in the atmospheric turbidity coefficient<sup>39</sup>, which is calculated from direct solar radiation<sup>40</sup> measurements taken at five stations in Japan excluding the fluctuation component of the troposphere, shows a clear impacts of stratospheric aerosols resulting from volcanic eruptions (Figure 3.3-1). The increased turbidity coefficients observed for several years after 1963 and during the periods of 1982 – 1983 and 1991 – 1993 were caused by the eruptions of Mt. Agung (Indonesia) in 1963, Mt. El Chichón (Mexico) in 1982 and Mt. Pinatubo (Philippines) in 1991, respectively. The increased turbidity stems from the persistent presence of sulfate aerosol in the stratosphere resulting from huge amounts of SO<sub>2</sub> released by the volcanic eruptions. The turbidity coefficient has now returned to approximately the same level as that observed before the eruption of Mt. Agung because no large-scale eruptions have occurred since that of Mt. Pinatubo.

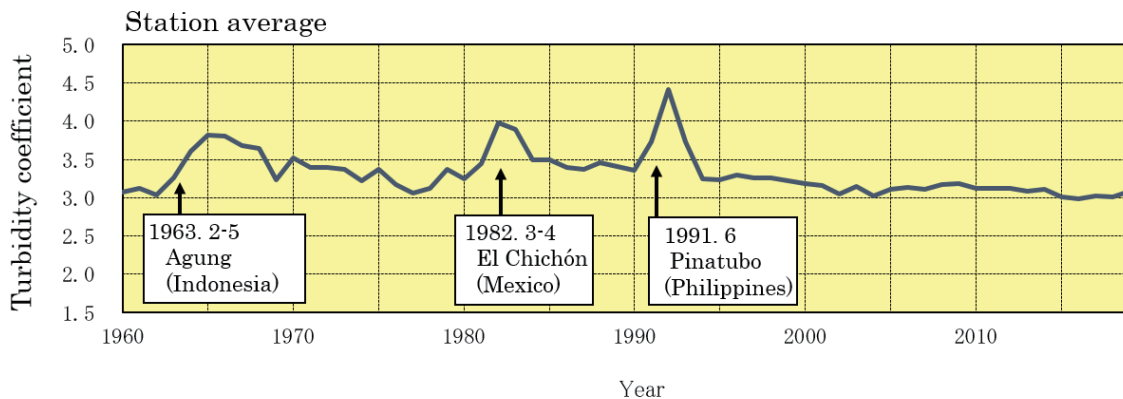


Figure 3.3-1 Time-series representation of annual mean atmospheric turbidity coefficients (1960 – 2018)

To eliminate the influence of variations in tropospheric aerosols such as water vapor, dust and air pollutants, the annual mean atmospheric turbidity coefficient is calculated using the minimum turbidity coefficient for each month.

<sup>38</sup> See the Glossary for terms relating to aerosols.

Information on surface radiation and Kosa is published on JMA's website.

<https://www.data.jma.go.jp/gmd/env/kosahp/en/kosa.html> (Aeolian Dust (Kosa))

[https://www.data.jma.go.jp/gmd/env/radiation/en/info\\_rad\\_e.html](https://www.data.jma.go.jp/gmd/env/radiation/en/info_rad_e.html) (Solar and Infrared Radiation)

<sup>39</sup> The atmospheric turbidity coefficient indicates the ratio of the atmospheric optical depth affected by aerosols, water vapor and gases in the atmosphere to that uninfluenced by constituents other than air molecules such as oxygen and nitrogen in the atmosphere. Larger values indicate greater amounts of turbid matter in the air.

<sup>40</sup> Direct solar radiation is the incident solar energy acting on the earth's surface from the sun. The atmospheric turbidity coefficient (also known as the Feussner-Dubois turbidity coefficient) can be calculated from direct solar radiation amounts.

### 3.3.2 Kosa (Aeolian dust)

Kosa (Aeolian dust) is a kind of aerosol blown up from semi-arid areas of the Asian continent and transported by westerly winds to Japan. A total of 11 JMA meteorological stations (as of 1 July 2020) perform Kosa monitoring. The phenomenon is recorded when visually observed by station staff. The number of days when any meteorological station in Japan observed Kosa was 8 in 2019 (Figure 3.3-2), and the total number of stations reporting its occurrence during the year was 16 (Figure 3.3-3).

The number of days on which Kosa is observed shows no discernible trend, but the annual total number of stations reporting observation is extremely likely to have increased (statistically significant at a confidence level of 95%.) As the phenomenon shows significant interannual variability, ongoing data collection is necessary to clarify related trends.

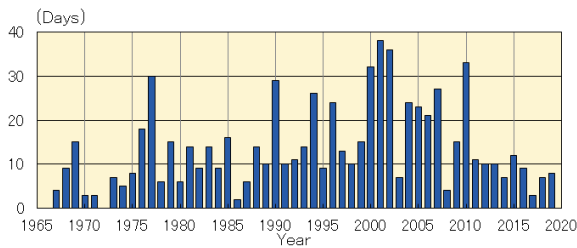


Figure 3.3-2 Number of days when any station in Japan observed Kosa (1967 – 2019) based on the 11 stations that were active for the whole period

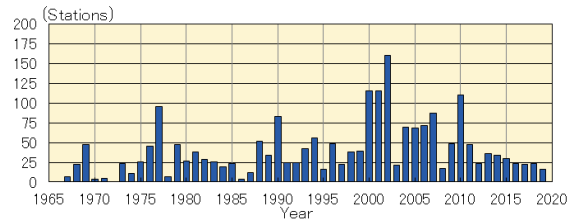


Figure 3.3-3 Annual total number of stations observing Kosa in Japan (1967 – 2019) based on the 11 stations that were active for the whole period

### 3.3.3 Solar radiation and downward infrared radiation

The earth's radiation budget is a source of energy for climate change, and monitoring of its variations is important. To this end, JMA conducts measurements of direct solar radiation, diffuse solar radiation and downward infrared radiation<sup>41</sup> at five stations in Japan (Sapporo, Tsukuba, Fukuoka, Ishigakijima and Minamitorishima) (Figure 3.3-4).

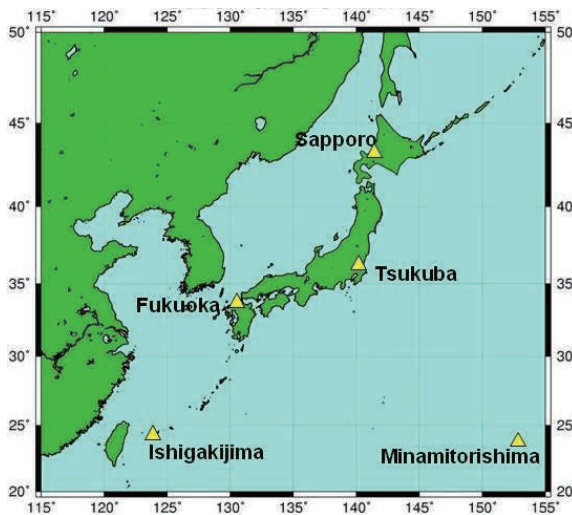


Figure 3.3-4 JMA's solar radiation and infrared radiation observation network

JMA conducts observation of direct solar, diffuse solar and downward infrared radiation at five stations (Sapporo, Tsukuba, Fukuoka, Ishigakijima and Minamitorishima).

41 Downward infrared radiation is the incident infrared radiation acting on the earth's surface from all directions in the sky. It is emitted from clouds and atmospheric constituents such as water vapor and carbon dioxide in proportion to the fourth power of their temperature, and can be used as an index of global warming.

### (1) Global solar radiation

Reports indicate that global solar radiation decreased from around 1960 to the late 1980s before increasing rapidly from the late 1980s to around 2000, and no obvious changes have been observed in most regions of the world (Ohmura, 2009).

In Japan, global solar radiation declined rapidly from the late 1970s to around 1990 before increasing rapidly from around 1990 to the early 2000s. Since then, data from measurements at the five observation stations show no obvious changes. These long-term variations are consistent with those reported globally (Figure 3.3-5). Variations are considered to stem mainly from changes in anthropogenic aerosols in the atmosphere, and to be partly attributed to changes in cloud cover and cloud characteristics (Wild, 2009). Norris and Wild (2009) quantitatively estimated the cause of the rapid increase in global solar radiation observed in Japan from around 1990 to the beginning of the 2000s. According to their estimates, two thirds of the increase was due to reduced anthropogenic aerosols in the atmosphere and the other third was due to reduced cloud cover. These results imply that the presence of anthropogenic aerosols has a profound effect on solar radiation variations. Results produced by Kudo et al. (2012) indicated that the solar radiation increase was mainly caused by changes in the optical characteristics of aerosols due to changes in the aerosol composition of the atmosphere.

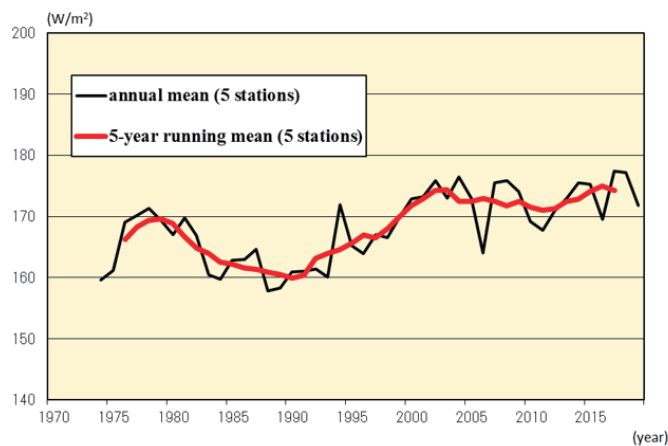


Figure 3.3-5 Time-series representations of annual and five-year-running means of global solar radiation at five stations in Japan (Sapporo, Tsukuba, Fukuoka, Ishigakijima and Minamitorishima)

### (2) Downward infrared radiation

Atmospheric concentrations of carbon dioxide and other greenhouse gases, which cause global warming, show increasing yearly trends. Observation of downward infrared radiation is effective for the evaluation of global warming because signals of global warming due to increased greenhouse gases are seen more clearly from increased downward infrared radiation than from increased surface temperatures. While general circulation model experiments suggest that two decades of downward infrared radiation monitoring are necessary to detect statistically significant increases with a confidence level of 95%, analysis of in situ observation data covering about a decade has shown an overall increase (Wild and Ohmura, 2004).

In Japan, downward infrared radiation has been monitored since the early 1990s at Tsukuba. Analysis of the data obtained shows an increasing trend at a rate of about 0.3 W/m<sup>2</sup> per year during the period from 1993 to 2019 (Figure 3.3-6). This is consistent with the trend seen in the

results of analysis using data from 20 BSRN<sup>42</sup> stations worldwide (+0.3 W/m<sup>2</sup> per year during the period from 1992 to 2009) (WCRP, 2010).

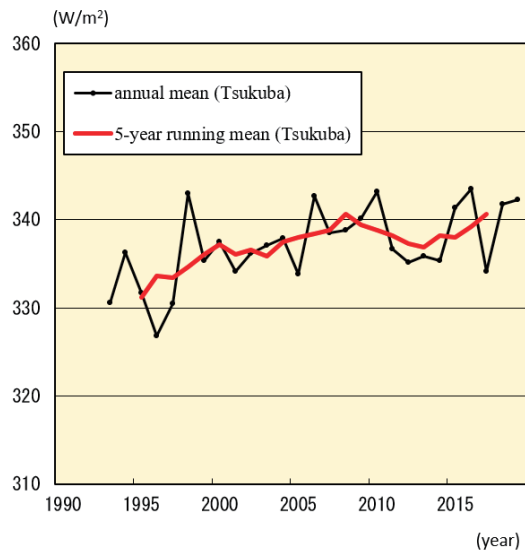


Figure 3.3-6 Time-series representations of annual and five-year-running means of downward infrared radiation at Tsukuba

---

42 The BSRN (Baseline Surface Radiation Network) is a global observation network for measuring high-precision surface radiation balance on an ongoing basis. JMA operates five BSRN stations in Japan (Sapporo, Tsukuba, Fukuoka, Ishigakijima and Minamitorishima) and one in Antarctica (Syowa Station).

## Explanatory note on detection of statistical significance in long-term trends

Meteorological observation data, including those relating to temperature and precipitation, are subject to large amplitude fluctuations due to the influence of atmospheric and oceanic dynamics on a broad spectrum of spatial and temporal scales. To examine the possible presence of long-term climate system trends associated with global warming in consideration of natural variability, raw climate data need to be converted into suitable statistical time-series representations and subjected to statistical testing in order to highlight the likelihood of systematic temporal trends that cannot be explained by random variability alone. When the results of such testing allow reasonable conclusion that random variability is unlikely to be the sole factor at work, a change is described as statistically significant.

In this report, the likelihood of a systematic long-term change existing in a time-series representation is based on the results of statistical significance testing performed at confidence levels of 99, 95 and 90%. The following terminology summary describes each level:

Level of confidence	Term
$\geq 99\%$	<b>Virtually certain</b> to have increased/decreased (statistically significant at a confidence level of 99%)
$\geq 95\%$	<b>Extremely likely</b> to have increased/decreased (statistically significant at a confidence level of 95%)
$\geq 90\%$	<b>Very likely</b> to have increased/decreased (statistically significant at a confidence level of 90%)
$< 90\%$	No discernible trend

The following statistical methods are applied for the data used in this report:

i) For statistical variables whose annual fluctuation component can be assumed to follow normal distribution

For temperature anomalies, trend-removed annual variability data are expected to approximately follow normal distribution. T-testing is performed for statistical variables assumed to be normally distributed using a coefficient of correlation between years and values.

ii) For statistical variables whose annual fluctuation component cannot be assumed to follow normal distribution

The assumption of normality may not be applicable to frequency statistics regarding weather conditions, including those for extremely warm days, tropical nights and hourly precipitation amounts exceeding 50 mm. Accordingly, non-parametric testing, which does not depend on underlying assumptions about distribution, is applied to such variables.

It should be noted that statistical tests are in theory inevitably susceptible to the establishment of false conclusions even if the results indicate a statistically significant trend. Even outcomes indicating statistical significance at confidence levels of 90, 95 or 99% imply that there are small inherent probabilities of up to 10, 5 and 1%, respectively, of the significance being erroneously detected when in fact the observed long-term change occurred by mere random chance. Conversely, when a systematic long-term change actually exists, statistical testing may fail to detect the significance correctly. In general, test results are not considered highly stable if they are based on observation records that are temporally limited, influenced by large annual fluctuations/rare events or subject to change when new observations are added to a data sequence. Readers are encouraged to interpret the analytical results presented in the report appropriately with due note of these considerations.

## Glossary

### **Aerosols**

Aerosols are airborne solids or liquids in fine particle form. Their many types include particles of natural origin blown up from land/sea surfaces, anthropogenic particles and secondary aerosols formed from anthropogenic and biogenic precursors. In addition to absorbing and scattering sunlight, they also provide condensation nuclei for clouds. Particulate matter 2.5 (PM<sub>2.5</sub>) is the name given to aerosol particles measuring 2.5 micrometers or less in diameter (about 30 times thinner than a human hair), and is considered to have possible adverse effects on human health when inhaled.

### **Anthropogenic**

Resulting from or produced by human activity.

### **Arctic Oscillation**

The Arctic Oscillation (AO) is a major atmospheric circulation variation exhibiting an annular pattern of sea-level pressure anomalies in a seesaw fashion with one sign over the Arctic region and the opposite sign over the mid-latitudes. Its negative phase, which is characterized by positive and negative sea-level pressure anomalies over the Arctic region and the mid-latitudes, respectively, helps cold Arctic air move into the mid-latitudes. The positive phase, whose sea-level pressure anomaly pattern is reversed, keeps Arctic air over the Arctic region.

### **Erythemal UV radiation**

Erythema is sunburn – a reddening of the skin resulting from continuous exposure to ultraviolet (UV) rays present in solar radiation. It is known that excessive erythema and long-term exposure to the sun can cause human health problems such as a high incidence of skin cancer and cataracts. Erythemal UV radiation is widely used as a scale of UV radiation for evaluation of its effects on the human body, and is calculated in consideration of various influences depending on wavelength.

### **Extreme climate event**

In general, an extreme climate event is recognized as an unusually severe or rare climate event creating disaster conditions or exerting significant socio-economic influence. The definition includes severe weather conditions covering periods ranging from only a few hours (such as heavy rain or strong wind) to several months (such as drought or cold summer conditions). JMA defines extreme climate events as those occurring once every 30 years or longer.

### **IPCC (Intergovernmental Panel on Climate Change)**

The Intergovernmental Panel on Climate Change (IPCC) is an international organization established by the United Nations Environment Programme (UNEP) and the World Meteorological Organization (WMO) in 1988. It reviews and assesses scientific, technical and socio-economic information on climate change, the potential impacts of such change and related

vulnerability, and options for adaptation and mitigation, in collaboration with scientists and experts on an international basis. The Panel's reports highlight common understanding of such information to support political matters such as treaty negotiations on global warming.

### **Kosa (Aeolian dust)**

Kosa (Aeolian dust) is a meteorological phenomenon in which fine dust is blown up to an altitude of several thousand meters by cyclonic or other wind systems from deserts or cropland in semi-arid areas of the Asian continent, and is transported over long distances by westerly winds, resulting in haze or dustfall in downstream areas. It is often observed between March and June in Japan and makes the sky yellow and hazy. Heavy Kosa can affect transportation by obstructing visibility.

### **Monsoon**

The term *monsoon* primarily refers to seasonally reversing winds, and by extension includes related seasonal rainfall change with wet and dry phases. Monsoon climate regions where seasonal winds prevail are found in numerous places around the world, with a major one located over a broad area from the Asian continent to northern Australia.

### **Normals**

Normals represent climatic conditions at meteorological stations, and are used as a base to evaluate meteorological variables (e.g., temperature, precipitation and sunshine duration) and produce generalizations (e.g., cool summer, warm winter and dry/wet months) for particular periods. JMA uses averages for the most recent three decades (currently 1981 – 2010) as normals, which are updated every decade in line with WMO Technical Regulations.

### **Terms relating to surface temperature variations**

**El Niño/La Niña events:** In an El Niño event, sea surface temperatures (SSTs) are higher than normal across a wide region from near the date line to the area off the coast of South America in the equatorial Pacific for about a year. In a La Niña event, SSTs are lower than normal in the same area. Both occur every few years, and are associated with frequent extreme climate conditions worldwide.

JMA recognizes the occurrence of an El Niño event when the five-month running mean of SST deviations from the climatological means (based on a sliding 30-year period averaged over the NINO.3 El Niño Monitoring Region (5°N – 5°S, 150°W – 90°W; Figure A)) remains +0.5°C or above for a period of six months or more. Similarly, a La Niña event is recognized when the corresponding figure is –0.5°C or below for the same area/period.

Figure B shows typical SST deviations from the normal during El Niño and La Niña events. The dark red and blue shading seen from the date line to the coast of South America indicates large deviations.

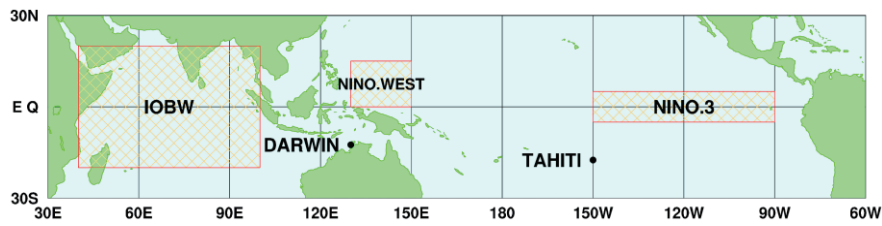
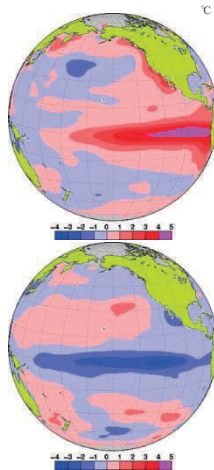


Figure A El Niño monitoring regions

Figure B Left: monthly mean SST anomalies for El Niño (November 1997); right: for La Niña (December 1998)

Red and blue shading represents positive and negative SST deviations, respectively. Darker shading indicates larger deviations. The unit of temperature is degrees Celsius.



**Southern Oscillation:** El Niño and La Niña events are closely related to trade winds (easterlies blowing around the tropical Pacific), which tend to be weak during the former and strong during the latter. The strength of such winds is closely related to the sea level pressure difference between eastern and western parts of the Pacific. This pressure difference varies in a phenomenon known as the Southern Oscillation. El Niño/La Niña events and the Southern Oscillation are not independent of each other; they are different manifestations of the same phenomenon involving atmospheric and oceanic interaction, and are referred to as ENSO (El Niño – Southern Oscillation) for short.

**Pacific Decadal Oscillation (PDO):** A phenomenon in which variables in the atmosphere and oceans tend to co-vary with a period of more than ten years in the North Pacific. When sea surface temperatures are lower (higher) than their normals in the central part of the North Pacific, those in its part along the coast of North America are likely to be higher (lower) than their normals, and sea level pressures in the high latitudes of the North Pacific are likely to be lower (higher) than their normals. These atmospheric variations affect meteorological conditions in North America and elsewhere.

**Indian Ocean Dipole mode (IOD) event:** A phenomenon in which sea surface temperatures (SSTs) are below normal in the south eastern part of tropical Indian Ocean (off the Sumatra Island) and above normal in the western part during the northern hemisphere summer and autumn (June - November). This east-west contrast of SST anomaly pattern is called dipole mode. On the other hand, a phenomenon in which SSTs are above normal off the Sumatra Island and below normal in the western part is called negative IOD event. These phenomena affect the climate near Japan and Australia through the changes of atmospheric circulation caused by atmospheric active (inactive) convections over above (below) normal SST area.

### **Terms relating to the greenhouse effect**

**Greenhouse effect:** The earth's atmosphere contains small amounts of greenhouse gases, which absorb a large part of the infrared radiation emitted from the earth's surface and re-emit it back, thereby warming the surface. This process is known as the greenhouse effect. Without it, the earth's average surface temperature of around 14°C would be approximately -19°C. Increased concentrations of greenhouse gases enhance the greenhouse effect, thereby producing higher surface temperatures. Major greenhouse gases include carbon dioxide, methane and nitrous oxide. Although water vapor has the strongest greenhouse effect, it is not usually regarded as a greenhouse gas in the context of global warming because the amount of water vapor on a global scale is not directly affected by human activity.

**Carbon dioxide:** Of all greenhouse gases, carbon dioxide (CO<sub>2</sub>) is the most significant contributor to global warming. Since the start of the industrial era in the mid-18th century, its atmospheric concentration has increased as a result of emissions associated with human activity, such as fossil fuel combustion, cement production and deforestation. Around half of all cumulative anthropogenic CO<sub>2</sub> emissions have remained in the atmosphere. The rest was removed from the atmosphere and stored in natural terrestrial ecosystems and oceans (IPCC, 2013).

**Methane:** Methane (CH<sub>4</sub>) is the second most significant greenhouse gas after CO<sub>2</sub>, and is emitted into the atmosphere from various sources including wetlands, rice paddy fields, ruminant animals, natural gas production and biomass combustion (WMO, 2019). It is primarily removed from the atmosphere via photochemical reaction with reactive and unstable hydroxyl (OH) radicals.

**Nitrous oxide:** Nitrous oxide (N<sub>2</sub>O) is a significant greenhouse gas because of its large radiative effect per unit mass (about 300 times greater than that of CO<sub>2</sub>) and its long lifetime (about 121 years) in the atmosphere. It is emitted into the atmosphere by elements of nature such as soil and the ocean, and as a result of human activity such as the use of nitrate fertilizers and various industrial processes. It is photo-dissociated in the stratosphere by ultraviolet radiation.

**ppm, ppb, ppt:** In this report, greenhouse gas concentrations are described in terms of mole fractions in units of ppm/ppb/ppt, representing the numbers of molecules of the gas per million/billion/trillion molecules of dry air, respectively.

### **Terms relating to the ozone layer**

**Total ozone:** Total ozone at any location on the globe is defined as the sum of all ozone in the atmosphere directly above that location, and is often reported in m atm-cm or Dobson units. The unit of m atm-cm (read as "milli-atmosphere centimeters") indicates the columnar density of a trace gas (ozone) in the earth's atmosphere. A value of 1 m atm-cm represents a layer of gas that would be 10 μm thick under standard temperature and pressure conditions. For example, 300 m atm-cm of ozone brought down to the earth's surface at 0°C would occupy a layer 3 mm thick. Typical values of total ozone vary between 200 and 500 m atm-cm over the globe, and the global mean is about 300 m atm-cm.

**Ozone-depleting substances:** Ozone-depleting substances (ODSs) are those that deplete the ozone layer as listed in the Montreal Protocol, which bans their production. Major ODS species include chlorofluorocarbons (CFC-11, CFC-12 and CFC-113 among others), carbon tetrachloride,

hydrochlorofluorocarbons (HCFCs), 1,1,1-trichloroethane, chloromethane, halons and bromomethane. These are also powerful greenhouse gases that trap heat in the atmosphere and contribute to global warming.

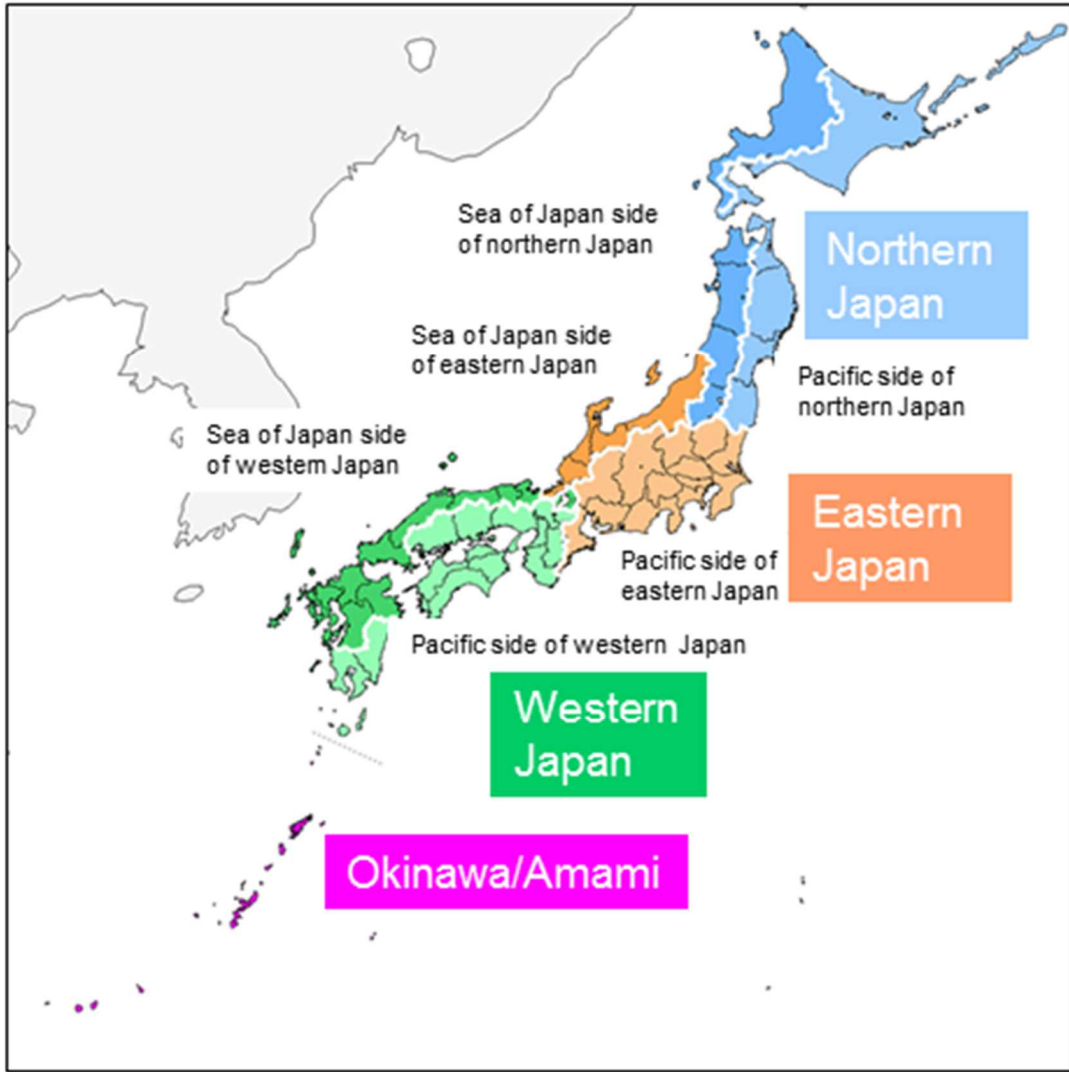
**Ozone hole:** The phenomenon referred to as the ozone hole is a reduction in the concentration of ozone high above the earth in the stratosphere over the Antarctica. For simplicity, it is often regarded as the area in which the total ozone amount is equal to or less than 220 m atm-cm to the south of the southern latitude of 45 degrees. The hole has steadily grown in size and annual length of presence (from August to December) over the last two decades of the last century.

**Montreal Protocol:** The Montreal Protocol on Substances that Deplete the Ozone Layer (a protocol to the Vienna Convention for the Protection of the Ozone Layer) is an international treaty designed to protect the ozone layer by phasing out the production of numerous substances believed to be responsible for ozone depletion. The treaty was opened for signatures in 1987 and came into force in 1989. Since then, it has undergone several revisions. Japan ratified the protocol in 1988.

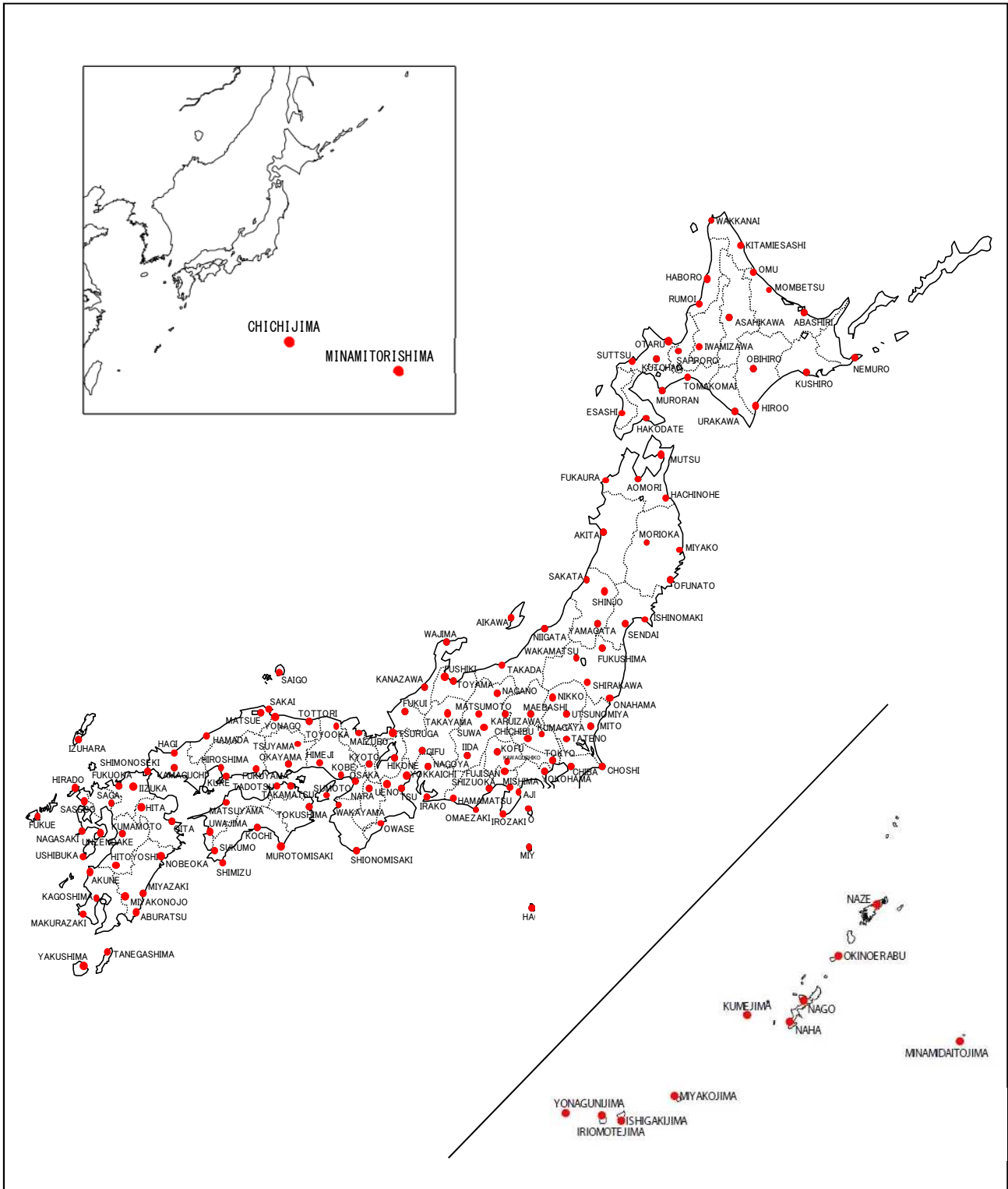
#### **Terms relating to water masses**

**North Pacific Subtropical Mode Water (NPSTMW) area:** A thermocline between the seasonal and main thermoclines. The NPSTMW area is considered to form in the surface mixed layer just south of the Kuroshio Extension as a result of huge heat loss in winter. It is defined as an area of 16 – 18-degree water at depths of 100 to 400 m at around 20 to 30°N along the 137°E line.

**North Pacific Intermediate Water (NPIW) area:** The NPIW area forms in the mixed region between the Kuroshio Extension and the Oyashio front. It is defined as water with a salinity level of 34.0 or less at a depth of around 800 m at around 20 to 30°N along the 137°E line.



Names of Japanese regions used in this report



Distribution of surface meteorological observation stations in Japan

# References

## Topics

- Kosaka, Y., and H. Nakamura, 2010: Mechanisms of meridional teleconnection observed between a summer monsoon system and a subtropical anticyclone. Part I: The Pacific-Japan pattern. *J. Climate*, 23, 5085 – 5108.
- Nitta, T., 1987: Convective activities in the tropical western Pacific and their impact on the Northern Hemisphere summer circulation. *J. Meteor. Soc. Japan*, 65, 373 – 390.

## Chapter 1

- EM-DAT: The OFDA/CRED International Disaster, Database – [www.emdat.be](http://www.emdat.be) – Université Catholique de Louvain – Brussels – Belgium
- IPCC, 2013: *Climate Change 2013: The Physical Science Basis. Contribution of Working Group I to the Fifth Assessment Report of the Intergovernmental Panel on Climate Change* [Stocker, T.F., D. Qin, G.-K. Plattner, M. Tignor, S.K. Allen, J. Boschung, A. Nauels, Y. Xia, V. Bex and P.M. Midgley (eds.)]. Cambridge University Press, Cambridge, United Kingdom and New York, NY, USA, 1535 pp.
- JMA, 1997: *Monthly Report on Climate System*, June 1997.

## Chapter 2

- IPCC, 2013: *Climate Change 2013: The Physical Science Basis. Contribution of Working Group I to the Fifth Assessment Report of the Intergovernmental Panel on Climate Change* [Stocker, T.F., D. Qin, G.-K. Plattner, M. Tignor, S.K. Allen, J. Boschung, A. Nauels, Y. Xia, V. Bex and P.M. Midgley (eds.)]. Cambridge University Press, Cambridge, United Kingdom and New York, NY, USA, 1535 pp.
- Mantua, N. J. and S. R. Hare, 2002: The Pacific decadal oscillation. *J. Oceanogr.*, 58, 35–44.
- Trenberth, K. E., J. M. Caron, D. P. Stepaniak and S. Worley, 2002: The evolution of El Niño–Southern Oscillation and global atmospheric surface temperatures, *J. Geophys. Res.*, 107, D8, doi: 10.1029/2000JD000298.

## Chapter 3

- Dettinger, M. D. and M. Ghil, 1998: Seasonal and interannual variations of atmospheric CO<sub>2</sub> and climate. *Tellus*, 50B, 1–24.
- Doney, S. C., V. J. Fabry, R. A. Feely and J. A. Kleypas, 2009: Ocean acidification: The other CO<sub>2</sub> problem, *Annu. Rev. Mar. Sci.*, 1, 169–192, doi:10.1146/annurev.marine.010908.163834.
- Friedlingstein, P., et al., 2019: Global Carbon Budget 2019, *Earth Syst. Sci. Data*, 11, 1783–1838, doi:10.5194/essd-11-1783-2019.
- Iida, Y., et al., 2015: Trends in *p*CO<sub>2</sub> and sea-air CO<sub>2</sub> flux over the global open oceans for the last two decades. *J. Oceanogr.* doi:10.1007/s10872-015-0306-4.
- IPCC, 2013: *Climate Change 2013: The Physical Science Basis. Contribution of Working Group I to the Fifth Assessment Report of the Intergovernmental Panel on Climate Change* [Stocker, T.F., D. Qin, G.-K. Plattner, M. Tignor, S.K. Allen, J. Boschung, A. Nauels, Y. Xia, V. Bex and

- P.M. Midgley (eds.]. Cambridge University Press, Cambridge, United Kingdom and New York, NY, USA, 1535 pp.
- Ishii, M., et al, 2011: Ocean acidification off the south coast of Japan: A result from time series observations of CO<sub>2</sub> parameters from 1994 to 2008, *J. Geophys. Res.*, 116, C06022, doi:10.1029/2010JC006831.
- Keeling, C. D., T. P. Whorf, M. Wahlen and J. van der Plicht, 1995: Interannual extremes in the rate of rise of atmospheric carbon dioxide since 1980. *Nature*, 375, 666–670.
- Keeling, R. F., S. C. Piper, and M. Heinmann, 1996: Global and hemispheric CO<sub>2</sub> sinks deduced from changes in atmospheric O<sub>2</sub> concentration. *Nature*, 381: 218-221.
- Kudo, R., et al, 2012: Aerosol impact on the brightening in Japan. *J. Geophys. Res.*, 117(D07208), doi:10.1029/2011JD017158.
- Le Quéré, C., et al., 2016: Global Carbon Budget 2016, *Earth Syst. Sci. Data*, 8, 605-649, doi:10.5194/essd-8-605-2016.
- Montzka, S. A. et al., 2018: An unexpected and persistent increase in global emissions of ozone-depleting CFC-11, *Nature*, 557, 413-417, doi:10.1038/s41586-018-0106-2.
- Niwa, Y., et al, 2014: Seasonal Variations of CO<sub>2</sub>, CH<sub>4</sub>, N<sub>2</sub>O and CO in the Mid-Troposphere over the Western North Pacific Observed Using a C-130H Cargo Aircraft. *J. Meteorol. Soc. Japan*, 92(1), 50-70, doi:10.2151/jmsj.2014-104.
- Norris, J. R. and M. Wild, 2009: Trends in aerosol radiative effects over China and Japan inferred from observed cloud cover, solar “dimming,” and solar “brightening,”. *J. Geophys. Res.*, 114(D00D15), doi:10.1029/2008JD011378.
- Ohmura, A., 2009: Observed decadal variations in surface solar radiation and their causes. *J. Geophys. Res.*, 114(D00D05), doi: 10.1029/2008JD011290.
- Rayner, P. J., I. G. Enting, R. J. Francey, and R. Langenfelds, 1999: Reconstructing the recent carbon cycle from atmospheric CO<sub>2</sub>, δ<sup>13</sup>C and O<sub>2</sub>/N<sub>2</sub> observations. *Tellus*, 51B, 213-232.
- Saito, T., et al, 2015: Extraordinary halocarbon emissions initiated by the 2011 Tohoku earthquake. *Geophys. Res. Lett.*, 42, doi:10.1002/2014GL062814.
- Sweeney, C., et al., 2015: Seasonal climatology of CO<sub>2</sub> across North America from aircraft measurements in the NOAA/ESRL Global Greenhouse Gas Reference Network, *J. Geophys. Res. Atmos.*, 120, 5155-5190, doi:10.1002/2014JD022591.
- Tsuboi, K., et al, 2013: Evaluation of a new JMA aircraft flask sampling system and laboratory trace gas analysis system. *Atmos. Meas. Tech.*, 6, 1257–1270, doi:10.5194/amt-6-1257-2013.
- Umezawa, T., et al, 2018: Seasonal evaluation of tropospheric CO<sub>2</sub> over the Asia-Pacific region observed by the CONTRAIL commercial airliner measurements, *Atmos. Chem. Phys.*, 18, 14851-14866, doi:10.5194/acp-18-14851-2018.
- UNEP, 2018: Environmental effects and interactions of stratospheric ozone depletion, UV radiation, and climate change: 2018assessmentreport.
- WCRP, 2010: Summary Report from the Eleventh Baseline Surface Radiation Network (BSRN) Scientific Review and Workshop. WCRP Informal Report No. 08/2010, 21 pp.
- Wild, M., 2009: Global dimming and brightening: A review. *J. Geophys. Res.*, 114(D00D16), doi:10.1029/2008JD011470.
- Wild M. and A. Ohmura, 2004: BSRN longwave downward radiation measurements combined with GCMs show promise for greenhouse detection studies, *GEWEX news*, 14(4), 20pp.

WMO, 2009: Technical Report of Global Analysis Method for Major Greenhouse Gases by the World Data Center for Greenhouse Gases. GAW Report, 184, WMO/TD No.1473.

WMO, 2018a: Scientific Assessment of Ozone Depletion: 2018. Global Ozone Research and Monitoring Project-Report, 58.

WMO, 2018b: WMO Greenhouse Gas Bulletin No.14.

WMO, 2019: WMO Greenhouse Gas Bulletin No.15.  
<http://www.wmo.int/pages/prog/arep/gaw/ghg/GHGbulletin.html>

WMO, 2020: WMO WDCGG DATA SUMMARY, WDCGG No.44, GAW Data Volume IV- Greenhouse Gases and Other Atmospheric Gases, published by the Japan Meteorological Agency in co-operation with World Meteorological Organization. Available at <https://gaw.kishou.go.jp/publications/summary>.

